Fast Design and Optimisation of One-Dimensional Microstrip Patch Antenna Arrays

by

Brandt Klopper

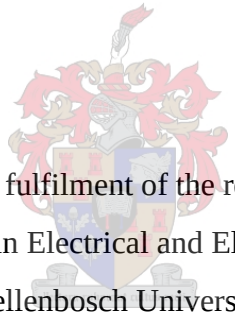

Thesis presented in partial fulfilment of the requirements for the degree Master of Engineering in Electrical and Electronic Engineering at Stellenbosch University

Supervisor: Dr. D.I.L. de Villiers

Faculty of Electrical and Electronic Engineering

March 2016

DECLARATION

By submitting this thesis electronically, I declare that the entirety of the work contained therein is my own, original work, that I am the sole author thereof (save to the extent explicitly otherwise stated), that reproduction and publication thereof by Stellenbosch University will not infringe any third party rights and that I have not previously in its entirety or in part submitted it for obtaining any qualification.

Date: .March 2016

Acknowledgements

Upon completion of this work, I would like to express my heartfelt thankfulness and appreciation for the support and assistance from my family, friends and teachers. In particular, I give my thanks to:

- My supervisor, Prof. Dirk de Villiers, whose guidance, support and expertise throughout the course of this project has been invaluable in my academic and professional development.
- Reutech Radar Systems, who made this project possible through their financial support.
- My fiancé, Jen, who has given me more friendship, love, patience and stability than I could ever have asked for. Words cannot express my gratitude.
- My mother and father, whose encouragement and interest in my work has been endless, and whose support is unfailing. Thank you for believing in me even when I did not, and for being my first and most prominent academic role models.
- My brother, Rijn, who implicitly taught me the value of substantiating claims with facts at a young age, and who also is an all-round great brother.
- My fellow students in Room E205, who gave me advice, assistance and comradeship through everything.
- My second family at *TomboKai Bujutsu*, who taught me resilience and patience in the long path towards self-improvement.
- My friends, who I have the privilege of being friends with, and who have remained my friends throughout the years.

Abstract

This thesis proposes a method for the design of one-dimensional, uniformly spaced, nonuniform amplitude microstrip patch antenna arrays using computationally inexpensive transmission-line models and space mapping surrogate-based optimisation. The method provides consistent and effective results for both impedance specifications and radiation specifications, and is significantly faster than conventional full-wave optimisation procedures.

The method is developed for microstrip-fed, probe-fed and aperture-fed rectangular microstrip antennas. Transmission-line models of each geometry are developed and run through a set of validation experiments to test their effectiveness over a range of substrate choices. The models are shown to perform with reasonable accuracy for a practical set of substrates, to the point where they are useful coarse models in space mapping optimisation procedures.

An optimisation framework is set out to apply the space mapping paradigm to the design of the three aforementioned patch element geometries, as well as the design of a one-dimensional array. Several types of space mapping techniques are tested on each design problem, and the most efficient is selected to incorporate into the main design method of the thesis.

The method incorporates the design of the individual patch antenna elements, the array layout and the finite antenna/feed substrate dimensions. The method is developed to accommodate microstrip feeds, probe feeds and aperture-coupled feeds to the patch antenna elements.

A design procedure is developed to design a one-dimensional patch antenna array to a desired impedance and radiation specification. The procedure is tested with 2 experimental S-band designs; a narrowband probe-fed 1x8 patch array and a wideband aperture-fed 1x8 patch array. The aperture-coupled patch array achieves 10% fractional bandwidth over a -10 dB $|S_{11}|$ passband, and exhibits 13.9° 3dB-beamwidth and -20.6 dB sidelobe-level in its gain pattern, across its passband. The total solver runtime of the entire aperture-coupled patch antenna array optimisation process amounts to 1708.14s (28.47 minutes).

The design method is modular, efficient and integrated with a general space mapping optimisation software framework. It is highly expandable and is one of few, if any works to apply a transmission-line model to the space mapping optimisation of an aperture-coupled patch antenna.

Opsomming

Hierdie tesis stel ’n metode voor vir die ontwerp van eendimensionele, uniforme gespasieerde, nie-uniform amplitude, mikrostrook plak antenna skikking met die gebruik van lae-intensiewe numeriese transmissielyn modelle en spasie-karterings surrogaat-gebaseerde optimisasies. Die metode lewer konsekwente en effektiewe resultate vir beide impedansie- en stralingspesifikasies. Die metode is beduidend vinniger as konvensionele vol-golf optimisasie prosedures.

Die metode is ontwikkel vir koplanêr-gevoed, probe-gevoed en gleuf-gevoerde reghoekige mikrostrook antennas. Transmissielyn modelle is ontwerp vir elke antenna geometrie en dié ontwerpe se effektiwiteit word getoets deur behulp van ’n stel validasie eksperimente oor verskeie substraat keuses. Daar word getoon in hierdie tesis dat hierdie modelle presteer met redelike akkuraatheid oor ’n reeks prakties-realiseerbare substrate. Sodoende kan hierdie modelle gebruik word vir rowwe modelle in Spasie-karterings optimisasie prosedures.

’n Optimasie raamwerk word opgestel om die spasie-karterings paradigma toe te pas op die ontwerp van die drie bogenoemde geometrie ontwerpe, asook op ’n eendimensionele skikking van antennas. Verskeie tipes Spasie-karterings tegnieke word getoets op elke ontwerpsprobleem, en die mees effektiefste tegniek word dan geïnkorporeer in die hoof ontwerp metode van die tesis.

Hierdie metode inkorporeer die ontwerp van die individuele plak antenna elemente, die skikking uitleg en die eindige antenna/voer substraat dimensies. Die metode is ontwikkel om mikrostrook, koplanêr voere, probe-voere en gleuf-gekoppelde voere te akkommodeer na die plak antenna elemente.

’n Ontwerp prosedure is ontwikkel om ’n eendimensionele plak antenna skikking te ontwerp by ’n gewenste impedansie en stralingsspesifikasie. Die prosedure is getoets met twee eksperimentele S-band ontwerpe, ’n nouband probe-gevoed 1x8 plak skikking en ’n wyeband gleuf 1x8 plak skikking. Die gleuf plak skikking behaal 10% fraksionele bandwydte oor ’n -10 dB $|S_{11}|$ deurlaatband, en stel ’n 13.9^{o} 3 dB-bundelwydte met ’n -20.6dB sylobvlak in die aanwins patroon oor die deurlaatband ten toon. Die totale hardlooptyd van die oplosser was 1708.14s (28.47 minute) vir die volledige gleuf plak antenna skikking optimisasie proses.

Die ontwerpsmetode wat uitgelê is in hierdie dokument is modulêr, effektief en geïntegreer met ’n algemene spasie-karterings optimisasie raamwerk Dit is hoog uitbreibaar en is een van die min, indien enige, metodes wat transmissielyn modelle gebruik vir die spasie-karterings optimisasie van ’n koppelvlak plak antenna.

Table of Contents

Chapter 1

Introduction

1.1 Problem Statement

A method is sought for the efficient design of cost-effective replacements for existing, high-specification radar antenna systems. The antenna systems are intended to be used in commercial-specification facsimiles of existing military-specification radar systems, and thus their requirements are less stringent, but their design and implementation are desired to be of a lower computational and physical cost. Systems operating in the L- to X-band frequency ranges are considered pertinent to the design problem. The solution presented in this thesis is the efficient design of a microstrip patch antenna array system.

As with most antenna structures, the design and optimisation of microstrip antennas requires some form of full-wave solution system. Full-wave solvers, while more accurate than circuit-based solvers, tend to be cumbersome and incur relatively high computational cost. When optimisations that call for many solver evaluations are considered, this cost can become almost prohibitively high. Attempts have been made to alleviate this burden through surrogate-based optimisation and the Space mapping optimisation paradigm [1] [2], whereby a less accurate 'coarse' model's response is adjusted to act as a surrogate for a finely-meshed full-wave 'fine' model. A survey of the literature shows that Space mapping procedures applied to the design of patch antennas have thus far only considered coarsely-meshed full-wave models for the 'coarse' model of the process. Even when they are coarsely-meshed, full-wave solutions are generally still considerably more computationally expensive than solutions implemented in microwave circuit solvers.

Thus, a need is presented both for a low-cost antenna design, as well as for a more efficient coarse model to apply to Space mapping optimisations of patch antennas. These two needs are combined to form the focus of this thesis.

1.2 About this Thesis

In this thesis, a method is proposed for the design of one-dimensional, uniformly spaced, nonuniform amplitude microstrip patch antenna arrays of 2^N antenna elements ($N \in 1,2,3 \ldots$). The method incorporates the design of the individual patch antenna elements, the array layout and the finite antenna/feed substrate dimensions. The method is developed to accommodate microstrip feeds, probe feeds and aperture-coupled feeds to the patch antenna elements.

The development of the method is facilitated through the design of several 1x8 patch antenna arrays with varying design specifications. Designs of below -10 dB reflection coefficient across 9-10%

fractional bandwidth are achieved at S-band and C-band, with 20dB sidelobe-level and 10-15° 3dB-beamwidth in the farfield gain pattern. The proposed method makes use of the Space mapping optimisation paradigm and introduces patch antenna transmission-line models to its use for the fast design of the patch antenna elements. The method is fast relative to Space mapping optimisations that exclusively use full-wave analysis, is simple in its implementation and can be applied to narrowband and wideband designs at frequencies between L- and X-bands. The method's versatility is in part due to its use of a general-purpose Space mapping code framework developed by Dr. D.I.L. de Villiers and Dr. R.D. Beyers.

Throughout this thesis, a number of numerical computations and simulations are performed. All of these computations are executed on a computer equipped with a dual core 2.4 GHz Intel® Core™ i7-5500U processor and 8 GB RAM.

The major contributions of this thesis are summarised as follows:

- A method for the fast design of probe-fed, microstrip-fed and aperture-fed narrowband and wideband patch antenna elements, using transmission-line models in a Space mapping optimisation procedure.
- An overall design strategy for one-dimensional, uniformly spaced, nonuniform amplitude microstrip patch antenna arrays of 2^N antenna elements.
- An analysis and comparison of the performance of various Space mapping techniques as they are applied to the above patch antenna element and array design methods.

1.3 Thesis Layout

The thesis begins with a theoretical overview of essential topics in Chapter 2. Special attention is paid to the development of the theory underpinning patch antennas, including transmission-line and cavity models. Various feeding methods of patch antennas are considered, as well as the theory of antenna arrays applicable to patch antennas.

Chapter 3 is a detailed study of the full-wave modelling of patch antenna elements. The FEKO MoM, CST Frequency Domain and CST Time Domain solver systems are all considered, and are applied to the simulation of coplanar- and aperture-fed patch antennas. Convergence studies are performed to determine the relative performance of each solution system, and the modelling of finite antenna substrates is considered. Finally, the modelling of coarsely-meshed full-wave models is discussed for use in the Space mapping procedures of the full antenna design method.

Chapter 4 analyses existing transmission-line models for various patch antenna elements. A microstrip-fed patch transmission-line model and aperture-fed transmission-line model is analysed and implemented in a commercial microwave circuit-solver system (AWR Microwave Office). The

transmission-line models' accuracy is also characterised, at least partially, by a set of three validation experiments testing the models across a range of design parameters.

Chapter 5 contains the theory of Space mapping, which is used to drive the patch element and array optimisation procedures of the full antenna design method. The application of Space mapping to the optimisation of a basic patch element, an aperture-fed patch element and a 1x8 patch antenna array is developed in detail. Examples of each of the three optimisations are provided for several Space mapping techniques.

Chapter 6 incorporates the information of the previous chapters to develop and detail the antenna array design method. The steps of the design procedure are listed and developed, and the software implementation of each step is discussed. Two antenna array designs at S-band are also developed, as examples of the execution of the antenna array design method.

The thesis is rounded off and concluded by Chapter 7, which contains closing remarks, a discussion of the work's limitations and recommendations for future related projects.

Chapter 2

Theoretical Overview

2.1 Antenna Fundamentals

In this section, an overview is provided of antennas and their operation. The section aims to create a foundation on which the more specific theory of this chapter can be built upon, and serves as a brief yet necessary explanation of antenna electromagnetic fields, radiation and the properties which are used to measure the behaviour and performance of antennas, in the context of this thesis.

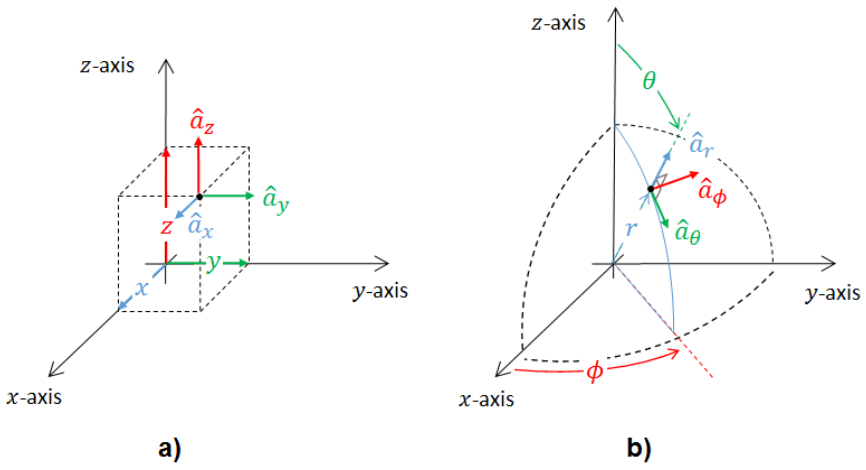

Figure 2.1 – Antenna physical coordinate systems: a) Rectangular, b) Spherical

In the context of this thesis, physical antenna structures and their electromagnetic fields are described in either rectangular or spherical coordinates. Rectangular $[\![x, y, z]\!]$ coordinates are used to describe the physical dimensions of the microstrip antenna systems under consideration, as they are mostly composed of rectangular geometries. Spherical $[\![r, \theta, \phi]\!]$ coordinates are used to describe all antenna fields and radiation characteristics, as is common practice [3]. The two coordinate systems are illustrated in Figure 2.1, as well as their orthogonal unit vectors.

The theory of this section considers antennas in the transmitting mode. The antenna structures considered in this thesis are all passive structures and are assumed to be made of linear materials, and by the Reciprocity theorem their receiving behaviour should be identical to their transmitting behaviour [4].

Antennas, broadly speaking, are structures designed to facilitate the transition of *guided* radio waves into *free space* waves [5], and vice-versa. The initial excitation is generated by a source, which is then propagated through a *feed* structure as a guided wave. The guided wave then comes into contact with

the antenna structure, where it is partially (and if the antenna is well-matched to the feed, minimally) reflected back into the feed- the remaining energy is transmitted onto the antenna. The transmitted portion of the wave then distributes across the antenna structure, where part of it is radiated into free space and the rest is either dissipated due to physical loss mechanisms (e.g. Ohmic losses) or contained in reactive electric and/or magnetic fields around the antenna [5]. A generic antenna system topology is shown in Figure 2.2a, as well as a typical electric field distribution in each section.

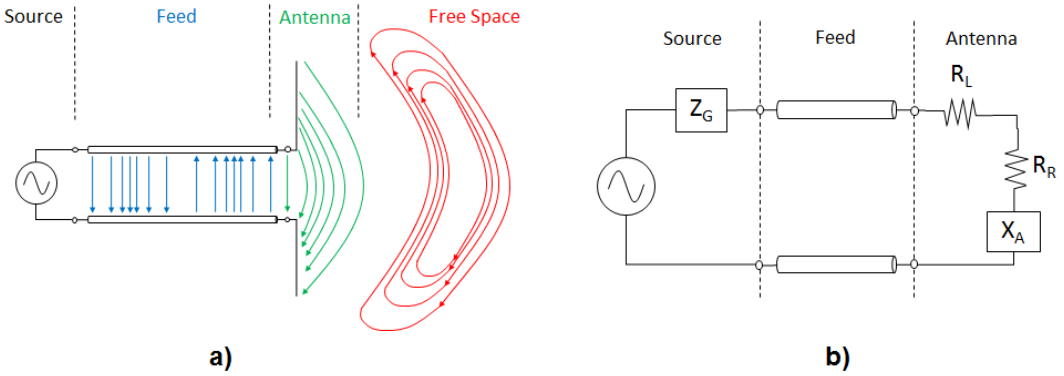

Figure 2.2- a) Generic antenna system topology and electric fields, b) Generic antenna system equivalent circuit

Figure 2.2b shows the equivalent circuit of the generic antenna topology. The antenna section is the series combination of three impedances: a resistance R_L, a resistance R_R and a reactance jX_A. These impedances represent the antenna losses, radiation and bound reactive fields, respectively [6]. This circuital representation of the antenna's electrical behaviour is the basis on which many antenna circuit and transmission-line models are patterned, such as the patch antenna transmission-line models of Section 2.2 and Chapter 4.

The laws that govern the electric and magnetic fields of antenna structures are well-documented in a variety of literature. The electromagnetic theory of cavity resonators, transmission-lines, and radiation are developed at length in [7]. For the sake of brevity, this theory is not repeated here, although it is the conceptual foundation of the antenna systems developed throughout this thesis.

2.1.1 Nearfields and Farfields

The space in which an antenna resides is usually divided into three spherical regions: the *reactive nearfield region*, the *radiating nearfield region* and the *farfield region* [6]. These regions are distinguished by the behaviour of the fields within them, and are demarcated by spherical radii r about the antenna's location.

The *reactive nearfield* region is the spherical volume immediately surrounding the antenna, where its bound reactive fields exist [6]. The region begins at the antenna origin ($r = 0$) and is commonly

considered to end at $r = 0.62\sqrt{\frac{D^3}{\lambda}}$, where D is the largest physical antenna dimension and λ is the operating wavelength [6]. This region is mostly studied in Section 2.2, where the reactive fields of microstrip antennas are analysed to determine their radiation and impedance characteristics. Throughout this work, the term *nearfield* is considered interchangeable with *reactive nearfield*.

The *radiating nearfield* region exists between the radial boundaries of the reactive nearfield region and the farfield region. This space is predominantly occupied by radiated fields that are dependent on r, and/or have field components collinear to the direction of spherical wave propagation $\hat{\boldsymbol{a}}_r$ [6]. The work of this thesis does not focus on the fields within this region.

The *farfield* region is defined where r is large enough to consider the radiated field as a free-space plane wave, and is typically defined for $r > \frac{2D^2}{\lambda}$ [6]. In this region, the radiated fields' angular distribution is effectively independent of r, and is therefore of the form:

$$\vec{\boldsymbol{\psi}}(\theta,\phi) = \hat{\boldsymbol{a}}_\theta \psi_\theta(\theta,\phi) + \hat{\boldsymbol{a}}_\phi \psi_\phi(\theta,\phi) \qquad (2.1)$$

where ψ denotes a general field quantity (e.g. electric field E, or magnetic vector potential A). The radiation properties of the antennas systems of this thesis are studied through their farfields. Any reference to radiation properties or radiated fields henceforth are assumed to be observed in the farfield region.

2.1.2 Antenna Properties

In this subsection, a selection of properties are laid out that are essential to understand the operation of the antenna systems considered in this thesis. These properties generally have several accepted definitions in literature [6], such that it is necessary to unambiguously state which definitions are relevant to this work.

2.1.2.1 Radiation Pattern

The term *radiation pattern* encompasses the various spatial functions that characterise the radiation of an antenna [6]. The patterns may measure some aspect of the radiated electric/magnetic field, or the radiated power [6]. In this work, farfield radiation patterns are considered, and are thus functions of elevation θ and/or azimuth ϕ.

The chosen definitions of the various radiation patterns correspond to those in [6]. While the patterns are mostly not restated here for the sake of brevity, the distinction between the *directivity*, *gain* and *realised gain* patterns must be made clear.

The *directivity* of an antenna is given by:

$$D(\theta,\phi) = \frac{4\pi U(\theta,\phi)}{P_{rad}} \quad (2.2)$$

where $U(\theta,\phi)$ is the radiation intensity pattern and P_{rad} is the total power radiated by the antenna structure [6]. Similarly, the *gain* is given by:

$$G(\theta,\phi) = \frac{4\pi U(\theta,\phi)}{P_{in}} \quad (2.3)$$

where P_{in} is the total power accepted by the antenna structure. The distinction is subtle, yet important, since gain incorporates the antenna's efficiency as a radiator, whereas directivity does not.

Finally, *realised gain* is given by [8]:

$$G_r(\theta,\phi) = \frac{4\pi U(\theta,\phi)}{P_{avl}} \quad (2.4)$$

Where P_{avl} is the available power provided at the interface of the feed and the antenna structure [8]. Realised gain incorporates the antenna efficiency as well as the impedance mismatch between the feed and the antenna. In some antenna designs, it is preferable to separate the feed's electrical behaviour from that of the antenna structure. However, the microstrip antennas considered in this work are integrated with their feeds, especially for coplanar microstrip feeds or aperture-coupled feeds where the feed and the antenna's radiation behaviour becomes difficult to separate. For this reason, realised gain is the preferred radiation power pattern of this thesis.

2.1.2.2 Sidelobe Level

The *sidelobes* of an antenna radiation pattern are its radiation lobes that are directed toward some (θ,ϕ) other than that of the main-lobe or back-lobe [6]. For a directive antenna design, sidelobes are undesired and should be minimised. *Sidelobe level* (SLL) is a metric that defines the sidelobe minimisation relative to the main lobe magnitude:

$$\text{SLL} = \frac{G_r(\theta_{main},\phi_{main})}{G_r(\theta_{side},\phi_{side})} \quad (2.5)$$

Where $(\theta_{main},\phi_{main})$ and $(\theta_{side},\phi_{side})$ are the orientations of the main-lobe and largest sidelobe, respectively. SLL is often stated in decibel (dB) form, where it becomes the difference between the main-lobe and sidelobe magnitudes.

2.1.2.3 Beamwidth

The *beamwidth* of an antenna is the angular separation between two identical points on opposite sides of the radiation pattern's main-lobe [6]. The main definition of beamwidth used throughout this thesis is 3dB-beamwidth.

3dB-beamwidth (or *half power*-beamwidth) measures the angular separation between the two directions where the radiated power pattern magnitude is half of the main lobe magnitude [6]. Half-power beamwidth is the default definition of beamwidth in this work.

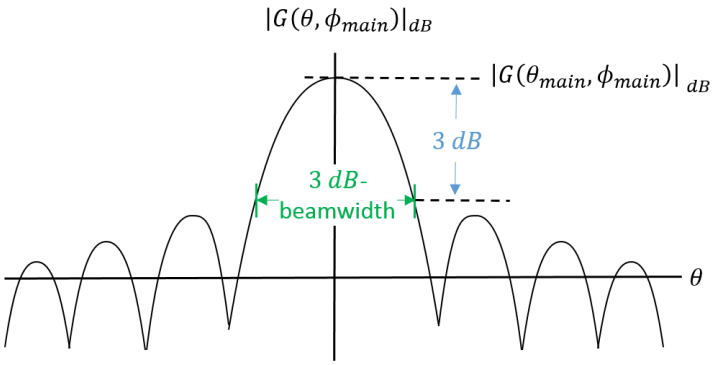

Figure 2.3 - 3dB-beamwidth of a typical antenna gain pattern

Figure 2.3 shows a typical gain pattern as a function of θ, and marks its 3dB-beamwidth. It should be noted that the above definition of beamwidth assumes a symmetrical radiation pattern about the main-lobe. This assumption is valid for most of the antennas considered in this work, and even in the few cases of radiation patterns distorted by feed asymmetry, the distortion is small enough to consider the patterns effectively symmetric.

2.1.2.4 Bandwidth

The *bandwidth* (BW) of an antenna is the frequency range for which the antenna performs at or above some minimum defined threshold, and is generally divided into the categories of *antenna bandwidth* and *impedance bandwidth* [9]. Impedance bandwidth measures the antenna's impedance matching, and is often measured as return loss or S-parameters. Radiation bandwidth is a somewhat more diverse category that can refer to various radiation characteristics, several of which are discussed in detail in the following subsections.

Whereas absolute bandwidth is measured in Hz, *fractional bandwidth* (FBW) is defined as the bandwidth normalised to the centre-frequency of the band [10]. FBW is often stated as a percentage, and is often used to distinguish between narrowband and wideband antenna systems. Similarly, *fractional frequency deviation* from a reference frequency is often stated as a percentage.

2.2 Microstrip Patch Antennas

Microstrip antennas, sometimes referred to as *printed antennas*, are a class of low-profile antenna that make use of printed-circuit-board (PCB) and microstrip technology. The structure of a microstrip antenna consists of some planar radiating conductor suspended above a ground-plane by a dielectric substrate (just as microstrip transmission-lines are, hence the name). The geometry of the radiating shape can take on a multitude of forms; rectangular, circular, triangular and dipole structures all exist commonly in literature [11], to name but a few. Microstrip antennas are most commonly fed by a coplanar microstrip line or a probe feed [12].

Figure 2.4 - Various Microstrip Antennas

Patch antennas belong to a subtype of microstrip antennas that have solid polygonal surfaces as their radiating shapes [11]. Rectangular patches in particular are easy to fabricate and analyse due to their geometric simplicity. As will be seen in the following section, the rectangular patch can be analysed using either a transmission-line model or a rectangular cavity model, the latter of which's modal expansion is facilitated by the patch's simple geometry.

Microstrip antennas, in general, are low in physical volume, cheap to produce, easy to integrate with larger microstrip networks (such as the front-end electronics of a radar transceiver), can be printed on planar or curved surfaces and are easy to fit with active electronics or microwave-frequency lumped elements. They are, however, not without disadvantages. Microstrip antennas can suffer from problems such as low radiation efficiency, poor polarisation purity and narrow fractional bandwidth in frequency (often 1-2%) [11]. Some of these disadvantages can be mitigated by techniques such as the use of multilayer *stacked patch* structures and an *aperture-coupled feed*; the former can be used to increase impedance bandwidth, while the latter improves both impedance bandwidth and polarisation purity [11]. These techniques and their effects on the performance of patch antennas will be discussed in detail, later in this chapter.

This thesis focuses on the design of antenna array elements that fall under the category of the *rectangular patch*. Its simplicity and versatility makes it an attractive and practical choice to use in the design of a low-cost antenna system. Additionally, a substantial body of research has been performed on rectangular patches with the Space mapping optimisation paradigm [2] [13] [14], which is the primary optimisation method of Chapter 6.

2.2.1 Basic Rectangular Patch

In this section, the impedance and radiation characteristics of the rectangular single-layer patch antenna will be derived and discussed. Both the *transmission-line* and *cavity* models of the patch structure are provided, as they are both popular and well-established models that provide their own insights into the operation of the antenna [11].

The models that are analysed in this chapter focus on characterising the impedance properties of the rectangular patch antenna. Both the transmission-line and cavity models provide solutions for the patch's radiation pattern, but their derivations are cumbersome, lengthy and require the evaluation of radiation integrals or asymptotic approximation [11]. More importantly, full-wave EM solvers can be used to cheaply and accurately solve the far-field radiation pattern, and will be used exclusively to model and optimise the patch antennas' far-fields in this thesis.

For the remainder of this chapter, and for all subsequent chapters of this thesis, the term *patch* is assumed to refer to a rectangular patch antenna.

2.2.1.1 Basic Patch Overview

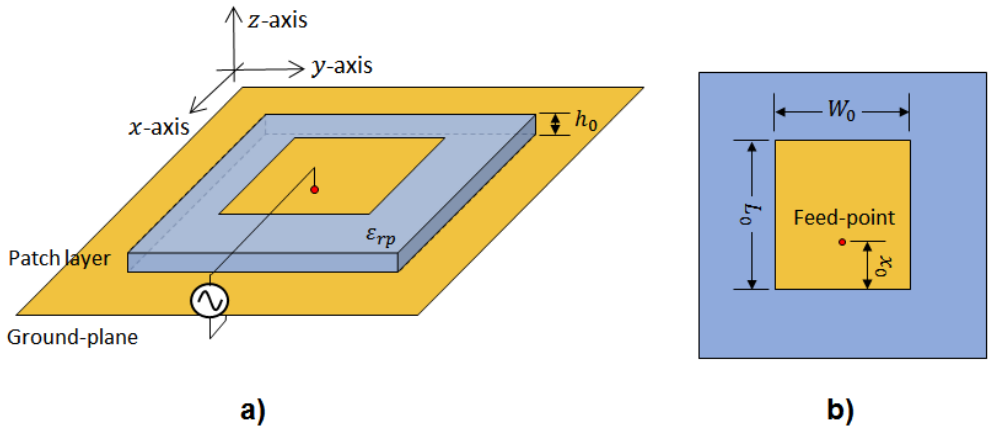

Figure 2.5 - Rectangular Patch Antenna: a) Isometric view, b) Top view

Figure 2.5 shows the structure and layout of a rectangular patch antenna. The relative permittivity of the substrate is denoted by ε_{rp}. Note that the rectangular coordinate axes that are shown in this figure

are consistent for every antenna analysed in this chapter, and that the feed-side edge of the patch exists at $[\![x,y,z]\!] = \left[\!\left[0, -\frac{W_0}{2} \leq y \leq \frac{W_0}{2}, h_0\right]\!\right]$. In the most general sense, the patch antenna operates by conducting current onto its surface from some feeding network, which distributes across that surface and some of which then radiates at certain edges of the patch. These edges are considered to function as radiating slots; as will be discussed with the cavity model, the modal excitation beneath the patch determines which edges radiate as such. Careful control of the modes excited beneath the patch is also necessary to ensure that the patch acts as a broadside radiator [11]; it is assumed henceforth that the patches in this thesis are designed to radiate a broadside main-lobe ($\theta = 0°$).

The geometry of a rectangular patch is defined by its length (L_0), width (W_0) and height above the ground-plane (h_0). In general, it is necessary that $h_0 \ll L_0$ and $h_0 \ll W_0$ [11]. The *principal E-plane* (or simply *E-plane*) is defined as the plane parallel to the L_0-defined edge and perpendicular to the patch surface (the xz-plane in Figure 2.5). Similarly, the *principal H-plane* is defined as the plane parallel to the W_0-defined edge and perpendicular to the patch surface (the yz-plane in Figure 2.5).

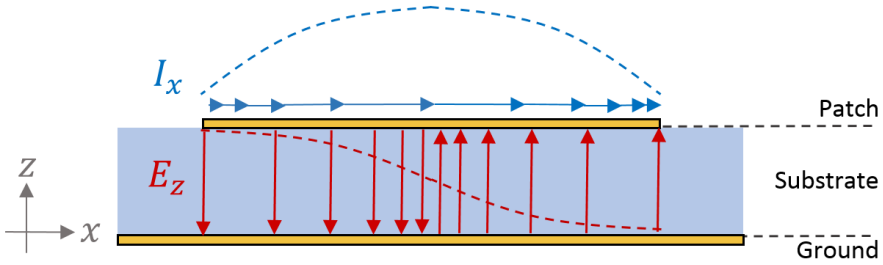

Figure 2.6 - E-plane (xz-plane) View of Patch E-fields and Surface Currents

Figure 2.6 shows an E-plane view of the z-directed electric fields beneath a patch excited in the $TM^z{}_{100}$ dominant mode, as well as the current magnitude of the upper patch surface along the E-plane (x-axis). The fields and currents are simplified approximations of the actual fields and currents, as is further discussed in Section 2.2.1.3. Note that this visualisation ignores the effect of fringing, which will be considered in the following subsection. The electric fields are assumed to be non-varying in the H-plane. The x-directed current distribution is much like that of a dipole antenna, varying sinusoidally along its length:

$$I_x(x) = \sin\left(\frac{\pi x}{L_0}\right) \qquad (2.6)$$

The patch also behaves like a dipole in the sense that it exhibits a radiating resonance for $L_0 = \frac{\lambda_p}{2}$. The resonant wavelength λ_p of the patch is given by:

$$\lambda_p = \frac{\lambda_0}{\sqrt{\varepsilon_{rpeff}}} = \frac{c_0}{f_0\sqrt{\varepsilon_{rpeff}}} \qquad (2.7)$$

where λ_0 is the free-space patch resonant wavelength, c_0 is the speed of light in free space, f_0 is the fundamental resonant frequency of the patch and ε_{rpeff} is the effective permittivity of the air/substrate dual medium that surrounds the patch. This resonance manifests as the point where the patch's input reactance (measured at the feed point) is zero. A typical response of this type is shown in Figure 2.7. Note that the peak real input impedance occurs very close to resonance.

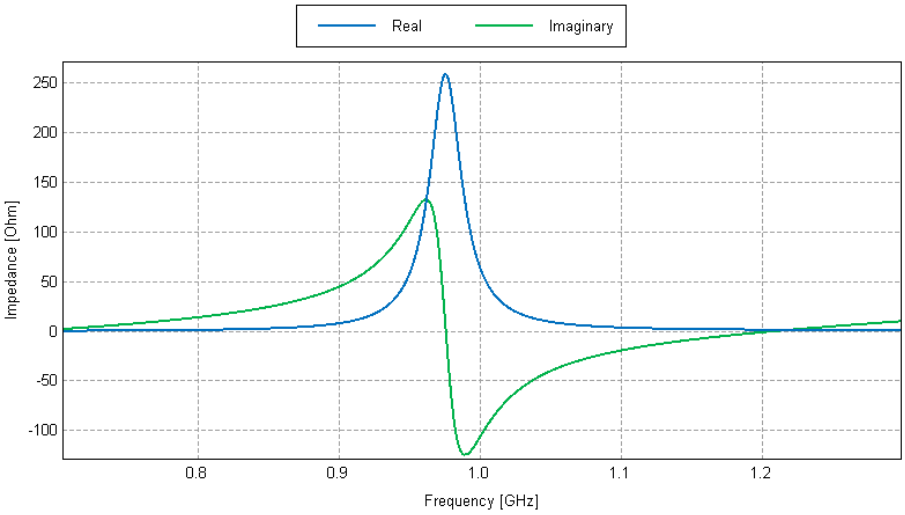

Figure 2.7 - Typical Input Impedance for an Edge-fed Patch with $f_0 \cong 1$ GHz

Assuming that the $TM^z{}_{100}$ dominant mode is excited, and ignoring the effects of fringing, the simplified resonant frequency of the patch is [11]:

$$f_{0s} = \frac{1}{2L_0\sqrt{\varepsilon_{rp}}\sqrt{\mu_0\varepsilon_0}} \qquad (2.8)$$

Where μ_0 and ε_0 are the permeability and permittivity of free space, respectively.

The exact placement of the feed on the patch significantly affects its impedance and polarisation characteristics. The magnitude of the input impedance can be varied by changing the x-axis feed-point x_0, since the E-field magnitude is zero at the patch centre and increases as the current decreases when the feed's x-position approaches the patch edges [11]. Feeding the patch on one of its edges produces the maximum input impedance; the patch of Figure 2.7 uses such a feed.

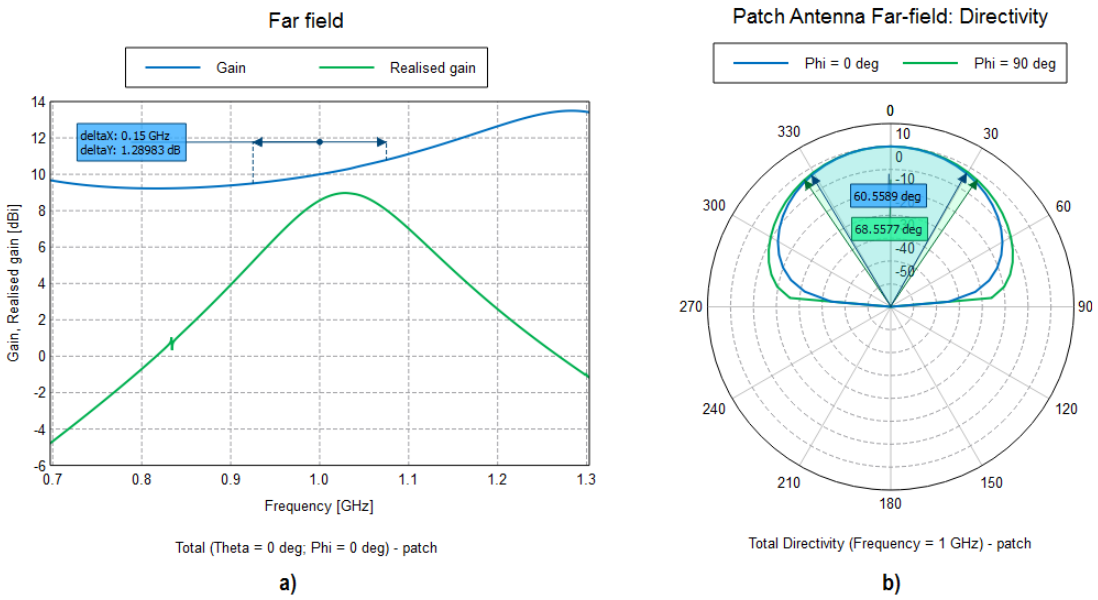

Figure 2.8 – Typical edge-fed basic patch antenna radiation characteristics: a) Gain and realised gain vs. frequency, b) E-plane and H-plane directivity

Figure 2.8a shows the ideal and realised maximum (broadside) gain versus frequency of a patch designed to resonate at $f_0 \cong 1$ GHz. It can be seen that the ideal gain is slow-varying about the resonant frequency, while the realised gain is strongly shaped by the radiating resonance. The relative flatness of the ideal gain allows the patch to operate across larger bandwidths than 1-2%, if the feed can be matched to the patch for the desired bandwidth. This is the purpose of aperture-coupled feeding, as will be discussed later in this chapter.

Figure 2.8b shows the patch antenna's E- and H-plane directivity in the far-field versus elevation. The 3dB-beamwidths in each plane, and the patterns in general, are similar to one another. Note that there is zero endfire radiation for an infinite ground-plane, which is desired in the formation of a planar antenna array so as to avoid mutual coupling through direct radiation (although the elements may still be vulnerable to surface-wave coupling effects).

2.2.1.2 Transmission-line Model

The transmission-line model (TLM) of a patch antenna is a simple and intuitive way to understand its behaviour, even if it does not yield the most accurate results [11]. The patch's rectangular shape allows it to be considered as a very wide, open-ended microstrip transmission-line. If $h_0 \ll W_0 < L_0$, then the radiating slots will occur at the H-plane edges (i.e. the edges at $\left[\!\left[0, -\frac{W_0}{2} \leq y \leq \frac{W_0}{2}, h_0\right]\!\right]$ and $\left[\!\left[L_0, -\frac{W_0}{2} \leq y \leq \frac{W_0}{2}, h_0\right]\!\right]$) [11].

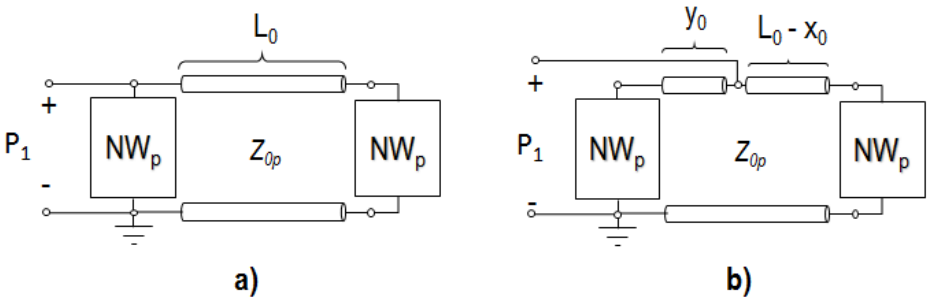

Figure 2.9- Rectangular patch TLM: a) edge-fed, b) inset feed

Figure 2.9 shows the general topology of the patch TLM, consisting of a length L_0 of ideal, lossless transmission-line with characteristic impedance Z_{0p}, terminated on either end with identical passive one-port networks NW_p. In Figure 2.9a, the feed-port P_1 is shown to be located on the end of the line, corresponding to an edge-fed basic patch, although the feed can be modelled as inset to a length x_0, as shown in Figure 2.9b.

NW_p represents the reactive and radiating qualities of the patch's radiating slots, and generally possesses some lossy element (such as a resistance or conductance), as well as a representation of the *fringing fields* at the slot (typically a capacitance). The exact composition of NW_p is discussed further in Chapter 4, where the TLM is fully developed for two proposed models.

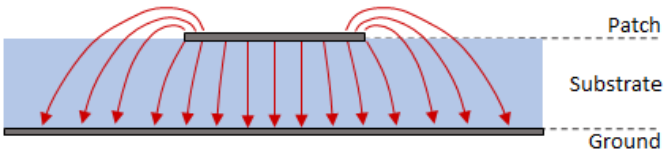

Figure 2.10 - Patch fringing E-field lines

The effect of fringing is dependent on the physical patch dimensions (L_0, W_0 and h_0) [11], and can have an effect on its impedance and radiation properties. Figure 2.10 shows the cross-sectional electric field distribution of a patch, including its fringing fields. In the E-plane, these fringes cause the patch to appear electrically longer than its physical length. Similarly In the H-plane, the fringes cause the patch to appear electrically wider. The nonhomogeneous medium (substrate and air) in which the patch resides also affects the fringing field distribution [11], as can be seen in Figure 2.10.

To account for the nonhomogeneous medium and fringing, the patch is attributed with an *effective length* and *effective permittivity*. Effective permittivity is given by [11]:

$$\varepsilon_{rpeff} = \frac{\varepsilon_{rp}+1}{2} + \frac{\varepsilon_{rp}-1}{2\sqrt{1+12\frac{h_0}{W_0}}} \qquad (2.9)$$

Where ε_{rp} is the relative permittivity of the substrate. In this instance, effective permittivity is defined as the dielectric constant of a uniform material that, when it replaces the inhomogeneous substrate-and-air medium of a given microstrip structure, provides the structure with identical electrical characteristics [11]. Since it is assumed that $h_0 \ll W_0$ for a patch antenna, ε_{rpeff} will almost always be lower than ε_{rp}, resulting in a higher characteristic impedance of the patch [11].

The effective length is given by [11]:

$$L_{eff} = L_0 + 2\Delta L \tag{2.10}$$

where

$$\Delta L = 0.412 h_0 \left(\frac{\left(\varepsilon_{rpeff} + 0.3\right)\left(\frac{W_0}{h_0} + 0.264\right)}{\left(\varepsilon_{rpeff} - 0.258\right)\left(\frac{W_0}{h_0} + 0.8\right)} \right) \tag{2.11}$$

In practice, L_{eff} should replace L_0 and ε_{reff} should replace ε_r to calculate the actual resonant frequency of the patch. The actual resonant frequency of the patch, including fringing effects, is then:

$$f_{0c} = \frac{1}{2L_{eff}\sqrt{\varepsilon_{rpeff}}\sqrt{\mu_0 \varepsilon_0}} \tag{2.12}$$

It is clear that if $L_{eff}\sqrt{\varepsilon_{rpeff}} \neq L_0\sqrt{\varepsilon_{rp}}$, then f_{0c} will differ from f_{0s}. The amount by which it differs, as well as whether f_{0c} is lower or higher than f_{0s} is dependent on the combination of W_0, h_0 and ε_{rp}, and thus will vary between different patch antenna designs.

Given a desired resonant frequency f_0, the patch length is then calculated as [11]:

$$L_0 = \frac{1}{2f_{0s}\sqrt{\varepsilon_{rpeff}}\sqrt{\mu_0 \varepsilon_0}} - 2\Delta L \tag{2.13}$$

2.2.1.3 Cavity Model

The cavity model considers the patch antenna as a lossy, dielectric-loaded cubic cavity. The model focuses on determining the modal fields between the patch surface and the ground-plane, although application of the Surface Equivalence Theorem allows one to analyse the fields radiated by the patch as well [11]. In order to represent radiation losses, the dielectric that fills the cavity is attributed an effective loss tangent $\delta_{eff} = \frac{1}{Q}$, where Q is the antenna quality factor [11].

In its simplest form, the patch antenna is modelled as a dielectric-loaded rectangular cavity bounded by Perfect Electric Conductor (PEC) at its ceiling and floor (the patch and ground-plane, respectively), and Perfect Magnetic Conductor (PMC) at its walls (the 'open' sections at the patch edges). The model is illustrated in Figure 2.11.

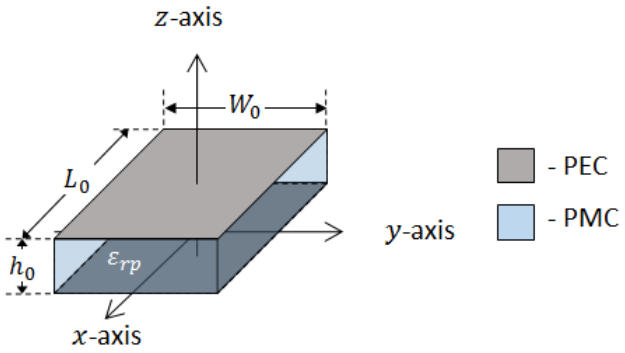

Figure 2.11- Rectangular patch antenna cavity model

The PMC walls enforce boundary conditions of the fields beneath the patch; on the PMC wall surfaces, the tangential H-fields and normal E-fields must be zero [7]. In practice, this is not the case, since the fringing fields and current flow from the top- to bottom-surface of the patch violate this boundary condition. However, the model is proven to quite accurately estimate the fields beneath the patch, and is generally a good approximation of a rectangular patch's actual behaviour [11].

A full exposition of the modal fields beneath the patch, using the magnetic vector potential A, is contained in [11]. The modal electric field x-, y- and z-components beneath the patch are thus given by:

$$\begin{aligned} E_x(x,y,z) &= -j\frac{k_x k_z}{\omega\mu_0\varepsilon_0\varepsilon_{rp}} A_{mnp}\sin(k_z z)\sin(k_x x)\cos(k_y y) \\ E_y(x,y,z) &= -j\frac{k_z k_y}{\omega\mu_0\varepsilon_0\varepsilon_{rp}} A_{mnp}\,sin(k_z z)\,cos(k_x x)\,sin(k_y y) \\ E_z(x,y,z) &= -j\frac{\left(k^2 - {k_z}^2\right)}{\omega\mu_0\varepsilon_0\varepsilon_{rp}} A_{mnp}\,cos(k_x x)\,cos(k_y y)\,cos(k_z z) \end{aligned} \qquad (2.14)$$

Where A_{mnp} is the amplitude coefficient of the ${TM^z}_{mnp}$ mode, and

$$\omega = 2\pi f \qquad (2.15)$$

$$k = \omega\sqrt{\mu_0\varepsilon_0\varepsilon_{rp}} \qquad (2.16)$$

The x-, y- and z-directed wavenumbers k_x, k_y and k_z all adhere to the constraint equation:

$$k_x{}^2 + k_y{}^2 + k_z{}^2 = \left(\frac{m\pi}{L_0}\right)^2 + \left(\frac{n\pi}{W_0}\right)^2 + \left(\frac{p\pi}{h_0}\right)^2 = 2\pi(f_r)_{mnp}^2 \qquad (2.17)$$

$$m, n, p \in 0,1,2 \ldots$$

The resonant frequency of the mnp^{th} cavity mode is given by:

$$(f_r)_{mnp} = \frac{1}{2\pi\sqrt{\mu_0\varepsilon_0\varepsilon_{rp}}}\sqrt{\left(\frac{m\pi}{L_0}\right)^2 + \left(\frac{n\pi}{W_0}\right)^2 + \left(\frac{p\pi}{h_0}\right)^2} \qquad (2.18)$$

Note that, in the above equations, it is assumed that the cavity dielectric has a relative magnetic permeability of $\mu_r = 1$. This assumption is also made for all of the dielectric patch substrates considered in this thesis.

The lowest resonant frequency corresponds to the dominant $TM^z{}_{100}$ mode [11]:

$$(f_r)_{100} = \frac{1}{2L_0\sqrt{\mu_0\varepsilon_0\varepsilon_{rp}}} \qquad (2.19)$$

Which is identical to the simplified patch resonant frequency f_{0s}. The E-field distribution beneath the patch for the $TM^z{}_{100}$ mode is therefore:

$$\begin{aligned} E_x(x,y,z) &= 0 \\ E_y(x,y,z) &= 0 \\ E_z(x,y,z) &= -j\frac{(k^2)}{\omega\mu_0\varepsilon_0\varepsilon_{rp}}A_{mnp}\cos(k_x x) \end{aligned} \qquad (2.20)$$

In the design of a patch antenna, it is useful to observe the fields beneath the patch to determine which modes are excited. Only the $TM^z{}_{100}$ mode should be excited to obtain the desired resonance and radiation characteristics, and the field equations developed in this subsection serve as a good reference for the designer to verify that a designed patch operates correctly.

2.2.1.4 Polarisation

The polarisation of a patch antenna is largely dependent on the geometry and placement of the feed [11]. Thus far, it has been assumed that the patch is fed on its surface somewhere along the E-plane ($y = 0$). This choice of feed placement ensures a mostly-linear polarisation along the E-plane [11].

The polarisation is closely linked to the modes excited beneath the patch. In general, any mode that is nonzero along only one coordinate-axis (e.g. $TM^z{}_{010}$, $TM^z{}_{200}$) is associated with linearly-polarised

radiation along either the E- or H-plane. For the designs contained in this thesis, linear polarisation along the E-plane is desired, and the geometries and feeding methods discussed in this chapter are designed as such.

2.2.1.5 Feeding Methods

The feeding network in Figure 2.5 is shown as a generalised transmitter connected to the radiating structure by an ideal pair of conducting wires. In practice, the patch must be fed by some realisable feeding structure; in this thesis, *microstrip* feeds and *probe* feeds are considered. These two types of feeds are illustrated in Figure 2.12

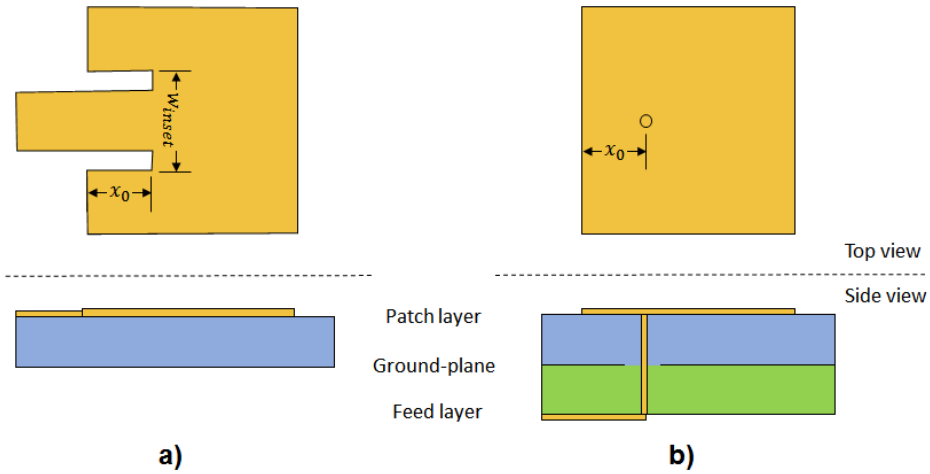

Figure 2.12 - Top and side view of Basic patch feeding methods: a) Microstrip feed, b) Probe feed

The probe feed consists of a wire connected to patch surface, extending through a small hole in the ground plane. The termination of the wire usually connects to a microstrip feed-line on the opposite side of the ground-plane. This feeding method provides shielding between the microstrip feeding structure and the antenna, although the wire itself possesses an inductance that can distort the input impedance of the patch.

The microstrip feed consists of a microstrip line on the same layer as the patch that connects directly to the patch structure. This feed only requires one substrate layer, but coplanar placement with the patch can result in the feed-line radiating spuriously and distorting the radiation pattern.

The line impedance of the microstrip feed is given by [15]:

$$Z_{0f} = \begin{cases} \dfrac{60}{\sqrt{\varepsilon_{rfeff}}} \ln\left(\dfrac{8 \cdot h_f}{w_f} + \dfrac{w_f}{4 \cdot h_f}\right) & \dfrac{w_f}{h_f} \leq 1 \\ \dfrac{120\pi}{\sqrt{\varepsilon_{rfeff}}\left[\dfrac{w_f}{h_f} + 1.393 + 0.667 \ln\left(\dfrac{w_f}{h_f} + 1.444\right)\right]} & \dfrac{w_f}{h_f} > 1 \end{cases} \quad (2.21)$$

where w_f is the width of the feed-line and h_f is the height of the substrate the feed is placed on, and the effective feed substrate permittivity ε_{rfeff} is given by [15]:

$$\varepsilon_{rfeff} = \frac{\varepsilon_{rf} + 1}{2} + \frac{\varepsilon_{rp} - 1}{2\sqrt{1 + 12\dfrac{h_0}{W_0}}} \quad (2.22)$$

The feed-lines should be set to a width to match the input port of the antenna structure. Throughout this thesis, it is assumed that the input port impedances are all 50Ω.

2.2.3 Aperture-fed Patch

In this section, a brief overview of the aperture-fed patch antenna is given, as well as a discussion of its transmission-line model and the effect of the aperture on the patch's overall electrical properties. The models presented here focus on the characterisation of the aperture itself and its coupling to the patch and the feed-line. The transmission-line model of the patch structure itself remains largely unchanged, and only differs from the prior model in the placement of its feed-point.

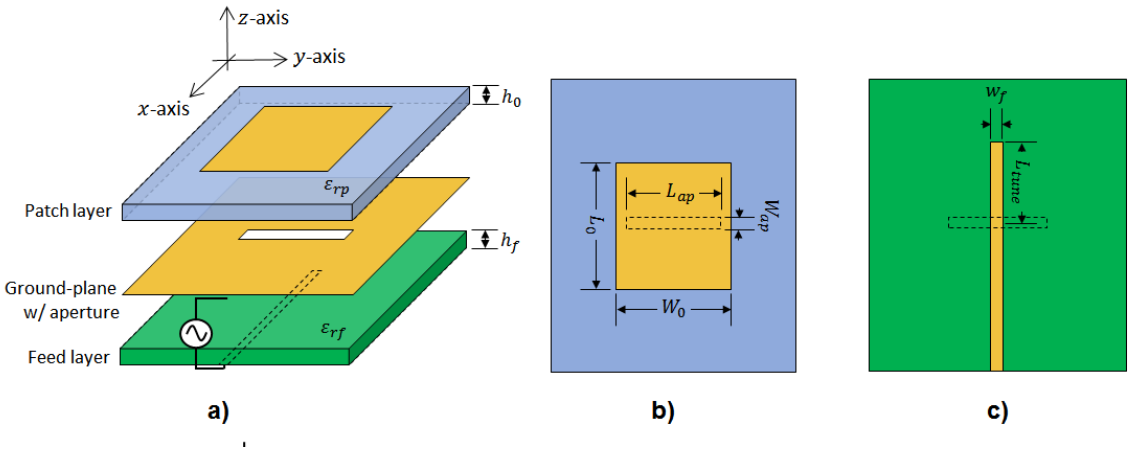

Figure 2.13- Aperture-coupled patch antenna layout: a) Exploded isometric view, b) Top view, c) Bottom view

The physical layout of the aperture-fed patch is shown in Figure 2.13. It is an enhancement of the basic rectangular patch that yields very low spurious feed radiation, improved bandwidth and high polarisation purity [16]. It is created by separating the antenna and feed substrates, placing them on opposite sides of the ground-plane, and placing an aperture of length L_{ap} and width W_{ap} in the ground-plane beneath the patch. A microstrip feed-line of width w_f runs over the aperture on the feed substrate, typically terminated in an open-ended tuning stub of length L_{tune}. The feed-line runs parallel to the antenna's E-plane. When the feed-line is energised, it electromagnetically couples to the patch through the aperture. The aperture may take on a variety of shapes, but in general it is considered to be of a narrow rectangular form.

Several design options become available with the use of the aperture-coupled feed. Firstly, the aperture's placement is to be considered, which can be used to control the input impedance, polarisation and feed-to-patch coupling strength [16]. In order to achieve maximum coupling, the aperture should be placed in the centre of the patch and at a right-angle to the feed-line (parallel to the antenna's H-plane) [16]. The primary coupling mechanism of the aperture is through the magnetic fields below the feed-line and patch, and the maximum magnetic field occurs below the patch centre [16].

The aperture's shape can be also used to control the coupling strength, as well as the shape of the open stub. However, the development of the TLM used in this thesis limits the aperture to a simple rectangle, and the stub to a uniform-width open line. This geometry is shown in Figure 2.13.

2.3 Antenna Arrays

A brief overview of the theory underpinning the operation of antenna arrays is given here. Placement of microstrip antennas in planar arrays is an effective method to increase the main-lobe of the gain

pattern and narrow the 3dB-beamwidth [17]. The radiation pattern features can be further controlled by nonuniform amplitude excitation of the array elements.

The *array factor* (AF) is a pattern multiplication function that describes the radiation pattern of an infinite or finite array of identical antenna elements. The full derivation of the array factor is contained in [18].

Further texts on array factor, nonuniform excitation, the Dolph-Chebyshev array amplitude distribution and synthesis is found in [17]. The effects of mutual coupling between patch antennas is described in [11].

2.4 Conclusion

In this chapter, a theoretical overview of essential topics has been provided, defining all of the necessary antenna and impedance properties for the scope of this thesis. Special attention is paid to the development of the theory underpinning patch antennas, including transmission-line and cavity models. Various feeding methods of patch antennas are considered, including probe-feeds, microstrip feeds and aperture-coupled feeds. A brief selection of pertinent array theory is also provided.

Chapter 3

Full-wave EM Modelling of Patch Antenna Elements

In the creation of a successful design process, it is crucial to have an accurate and stable source of reference information which can be used to determine the reliability of specific design results. Actual impedance and radiation measurements of realised patch antenna elements would be ideal, yet impractical; the next best option is to use a full-wave EM solver, which provides rigorous solutions based on comprehensive electromagnetic theory, rather than circuit theory-based approximations. In cases where complex and unexpected field interactions occur between structural components, a full-wave solver is capable of discerning and including those interactions in its results. In a planar radiating structure such as a patch antenna, a circuit solver is likely not as well-suited to fully model its behaviour as a full-wave solver is; even if the circuit solver is conditioned to solve microstrip problems, it will likely not be capable of modelling radiation effectively (or at all), and an inaccurate circuit-based substitution would have to be used. In structures with complex features such as an aperture in a ground-plane, the full-wave EM solver is undoubtedly the most reliable choice, as these features are particularly difficult to model with circuit or transmission-line elements (as has been discussed in Chapter 2).

One must bear in mind that, despite the advantages listed above, full-wave solvers are implemented digitally, and as such their results are based on an approximate discretisation of the modelled structure. It is of utmost importance to correctly discretise the structure for the sake of the model's reliability, particularly with a patch antenna that possesses a desired resonant behaviour and physical dimensions on the order of λ_0.

In this chapter, a number of available EM solver systems are proposed and their capabilities are discussed in the context of the design problem at hand. Thereafter, the solvers are applied to the modelling of the two patch antenna element designs under consideration (basic pin/microstrip-fed and aperture-fed), and their performance is quantified and compared. Finally, a study of the solvers' ability to model a practical antenna with a finite substrate and ground plane is conducted.

3.1 EM Solver Systems

Two full-wave electromagnetic solver software packages are evaluated in this study: EMSS' FEKO 7.0 and CST Microwave Studio (MWS) 2015. These solvers are available, well-documented and well-

supported in the academic environment and industry, and both have established usage in the solution of microstrip antenna systems [19] [20].

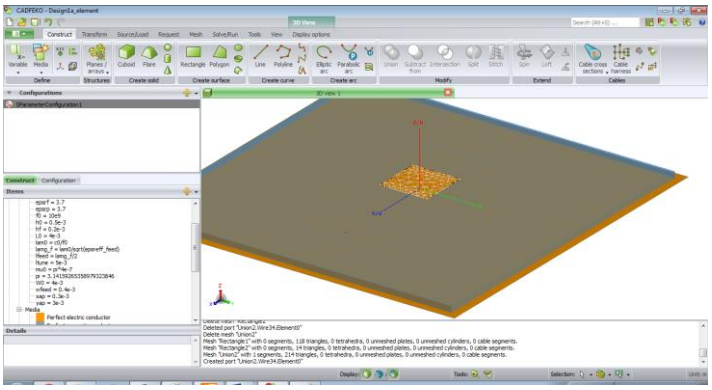

Figure 3.1- FEKO Software Environment

Three distinct solution systems are considered, in total:

- FEKO Method of Moments (MoM) solver
- CST MWS Frequency Domain solver
- CST MWS Time Domain solver

The Frequency and Time Domain solvers in CST MWS are both included in the assessment for the sake of thoroughness, as they both appear to be applicable to the design problem. The Time Domain solver appears to be the publisher's choice for simulating microstrip antenna systems [19], and indeed it may be the better solver for a basic pin/microstrip-fed patch element. However, it is worth assessing both options given the relative ease of switching between solvers (only the mesh requires re-evaluation, and no structural rebuilding is needed), especially for the case of the aperture-coupled patch antenna. The Frequency Domain solver is recommended for resonant structures with a high quality factor [21], and although the aperture-coupled patch may not have a high quality factor, the dual resonance of the patch combined with the aperture raises the question of which solver would be more accurate and/or efficient.

Within FEKO's MoM, a number of accelerative techniques are available, such as the Multilevel Fast Multipole Method (MLFMM) and the Physical Optics (PO) method [22]. MLFMM and PO are intended for electrically large structures, and a structure with physical dimensions on the order of λ_0 would be too small to benefit from their inclusion. Furthermore, FEKO's implementation of MLFMM cannot be used with Planar Green's Functions (PGF) structures such as the Planar Multilayer Substrate feature [23]. Hence, only standard MoM is applicable to the design problem under consideration.

3.1.1 FEKO MoM

FEKO's Method of Moments (MoM) solver is based on the weighted-residual method of the same name [22], and is primarily a surface-based solution method. Structures are meshed as the outer surfaces of

conductors and dielectric regions, and each mesh triangle constitutes a subdomain basis function that is attributed some electric current density [24]. By discretising the current distribution across the conductor, one can find an approximate solution for the surrounding electric and magnetic fields by use of integral equations such as Electric Field Integral Equations (EFIE) [24]. This formulation does not a bounding-box to be defined at the model extents, nor does it require the space surrounding the structure to be meshed, making MoM a good choice for antenna and farfield radiation problems.

MoM is particularly well-suited to patch antennas, since the structure is composed entirely of planar conducting surfaces and parallel dielectric regions. Additionally, The FEKO MoM solver allows infinite ground-planes and dielectric layers to be modelled without explicitly meshing them, significantly accelerating the solution process.

FEKO MoM can be accelerated by defining planes of electric and/or magnetic symmetry. Since the patch, aperture and feed-line possess magnetic symmetry about the antenna's E-plane, this feature can be taken advantage of to help reduce computational cost.

Frequency sampling in FEKO is either done by explicitly setting a number of discrete frequencies, or by using its built-in interpolant sampling method. In this chapter, interpolant sampling is used, but in further chapters where a discrete set of points is required, discrete sampling is preferred.

3.1.3 CST MWS Solvers

Both the Frequency Domain and Time Domain solvers are built upon the Finite Integration Technique (FIT), a volumetric solution method applicable to static and dynamic electromagnetic problems [25]. The method is applicable to uniform, orthogonally-gridded hexahedral meshes, as well as nonuniform grid schemes such as tetrahedral and subgridded hexahedral meshes.

Unlike FEKO MoM, the Frequency/Time Domain solvers require the entire volume within the model extents to be meshed explicitly. Additionally, boundary conditions must be set at the cubic faces of the model extents. Symmetry plane acceleration is available for both solvers, and magnetic symmetry is thus set about the patch's E-plane.

3.2 Modelling of Basic Patch

The basic patch antenna can be separated into four major components: the patch surface, the substrate dielectric, the ground-plane and the feeding port. The following subsections detail their exact construction and meshing in the three solver systems, and the considerations concerning their accuracy.

3.2.1 FEKO MoM

In the FEKO environment, the substrate and ground-plane are chosen to be constructed with the Planar Multilayer Substrate feature, and allows them to be simulated without concern for their mesh structure.

The patch surface is the only structure in this design that requires explicit meshing, and it must be meshed in such a way to accurately discern the expected surface current distribution. It should be noted that the patch surface is built as an infinitely thin PEC surface, which is not entirely accurate but is a good and efficient approximation of a very thin conductor layer on a PCB surface.

As shown in Chapter 2, the electric current density on the upper surface of a patch excited in the TM^z_{100} dominant mode is expected to vary sinusoidally along the E-plane axis, with its most rapid variation at the patch edges parallel to the H-plane. The patch should therefore be meshed more finely at those edges than at the patch centre, where the variation of current along the E-plane is near zero.

In order to realise this meshing scheme, the edges parallel to the H-plane are selected in the FEKO interface and assigned a local mesh refinement factor F_{mesh}. Meshing schemes of the patch surface for different values of F_{mesh} are shown in Figure 3.2:

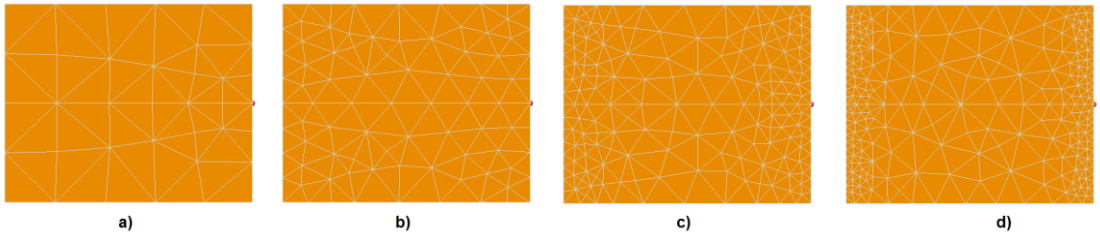

Figure 3.2 - Patch surface mesh with: a) $F_{mesh} = \frac{\lambda_0}{12}$, *b)* $F_{mesh} = \frac{\lambda_0}{30}$, *c)* $F_{mesh} = \frac{\lambda_0}{60}$, *d)* $F_{mesh} = \frac{\lambda_0}{120}$

Several choices are available to build the feeding port with, namely the *Wire*, *Edge* and *Microstrip* port options. The *Wire* port is a simple structure that places a vertical conducting wire between the patch and the ground-plane, but it also possesses the inductance associated with a wire of its length and radius. It is the most accurate result for a probe-fed port, since it actually models the presence of the probe wire.

The *Edge* port allows one to specify a finite edge as the input, which is more accurate for microstrip feeds. However, the connection to ground is a solid conducting plate that will likely interfere with the fields beneath the patch, and is best avoided unless a sufficiently long section of microstrip feed-line is inserted between the patch edge and the port.

Finally, the *Microstrip* port allows the definition of a single edge as the input, and links it to an infinite ground (such as in a *Planar Multilayer Substrate*) without needing an extraneous conducting structure as the *Edge* port requires. This is the most appropriate and accurate feed to use for a microstrip feed, but it is only useable in a substrate that exists above the specified ground-plane. For a basic microstrip-fed patch, the *Microstrip* port is the most pertinent choice.

3.2.2 CST MWS Frequency Domain Solver

In CST MWS, the substrate and ground-plane are constructed as a finite surface and cubic volume. The use of the *Open* boundary feature, however, can produce results similar to an infinite substrate and ground-plane if applied at the right boundary planes. The full set of boundary settings is illustrated in Figure 3.3. The patch, as with FEKO, is approximated by an infinitely thin PEC surface.

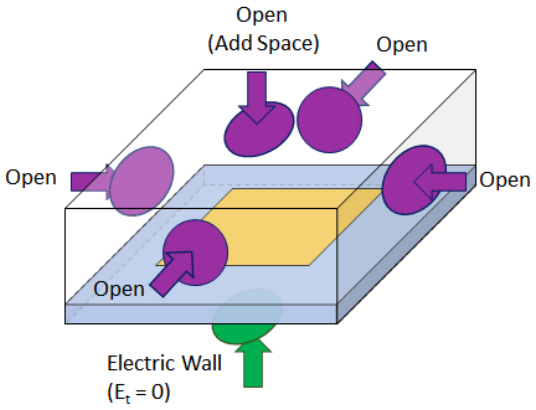

Figure 3.3 - Basic patch CST MWS boundary settings

A *Discrete* port is used to feed the patch antenna, and operates similarly to the *Wire* port in FEKO. The port does not, by default, carry the electrical properties of a wire like FEKO's *Wire* port, however, and functions as an ideal point-feed port of arbitrary input impedance [26]. The alternate option is to use a *Waveguide* port, but it requires a length of microstrip feed-line between the patch edge and itself to function adequately, and is thus only applicable to a microstrip-fed patch. This extra structure requires more computational expense, and the *Waveguide* port itself is requires extra computation due to its internal-mode calculation process [27]. For the basic probe-fed patch, the *Discrete* port is the best option.

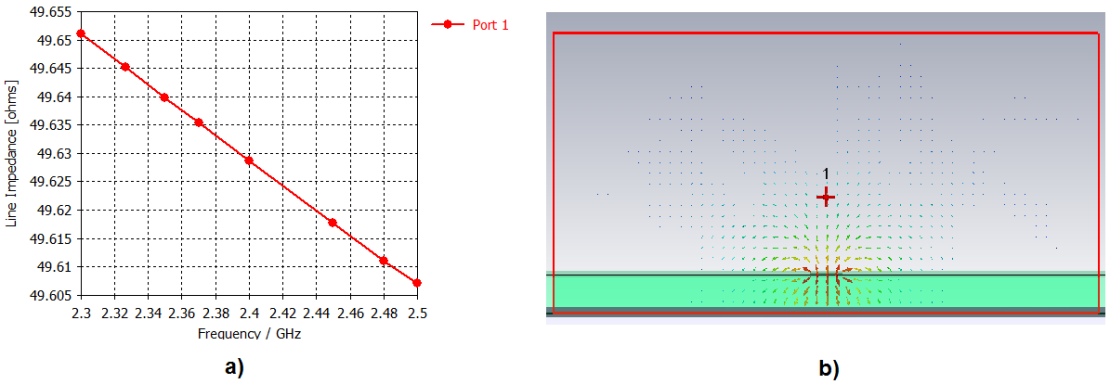

Figure 3.4- CST Waveguide port: a) Line impedance at Port 1, b) E-field at Port 1

Figure 3.4a shows the modal port impedance inside a CST MWS *Waveguide* port.

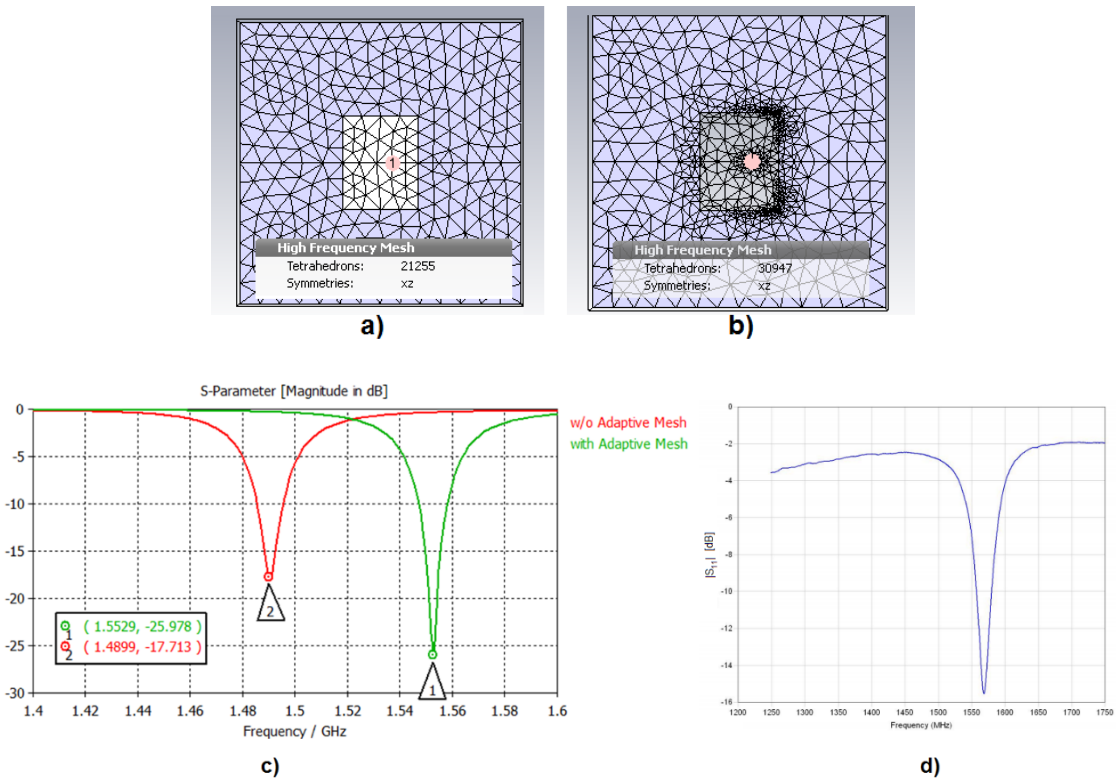

Figure 3. 5- a) CST patch model without adaptive mesh refinement and b) with adaptive mesh refinement, c) S_{11} of both patch models, d) measured S_{11} of patch manufactured to same specification

The Frequency-Domain solver standardly uses a tetrahedral volumetric mesh, although a hexahedral mesh is also available [21]. The solver also allows (and encourages) the use of an adaptive mesh refinement process that conditions the mesh to best fit the model's electrical behaviour. Figure 3. 5a shows an example of a patch antenna meshed at the default global mesh settings (4 steps per wavelength, minimum 10 steps on tetrahedral meshing) alongside the same model subjected to adaptive mesh refinement in Figure 3. 5b. Figure 3. 5c plots the two models' corresponding S-parameters ($|S_{11}|_{dB}$), while Figure 3. 5d shows the measured $|S_{11}|_{dB}$ of a patch antenna built to the same specification as the CST models ($L_0 = 46mm$, $W_0 = 57mm$, $h_0 = 1.6mm$, $\varepsilon_r = 4.1$), as originally reported in [28].

It is clear that the adaptively-refined mesh produces a more accurate result than the unrefined mesh, as its resonant frequency is much closer to that of the measured result (1.572 GHz). It can also be seen in Figure 3. 5b that the adaptive mesher has targeted the edges of the patch for refinement, where the current varies most rapidly as a function of position. This meshing scheme agrees with the FEKO meshing rationale laid out in the previous subsection, saving computational cost by applying a fine mesh only where it is necessary.

3.2.3 CST MWS Time Domain Solver

The Time Domain solver uses the same model-building features as the Frequency-Domain solver, although its meshing process is different. A hexahedral mesh must be used in this solver, which

functions as a three-dimensional grid. Local mesh refinement is standardly processed as a refinement of distance between global grid-lines; that is to say, if a small feature is finely meshed in a large volume, a space much larger than the feature will share those fine mesh properties. This is illustrated in Figure 3.6, where the mesh is set to refine at the patch edges:

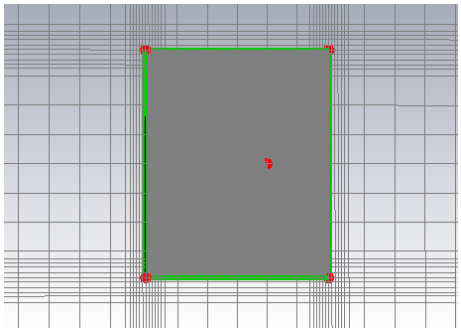

Figure 3.6- Time Domain solver hexahedral mesh refinement (refinement on patch edges)

As can be seen, the mesh is refined not only in the immediate vicinity of the patch edges, but along the entire grid-lines that pass through that vicinity. This trait could be considered as computationally costly, although the Time Domain solver is nonetheless known for its relative speed and efficiency [29].

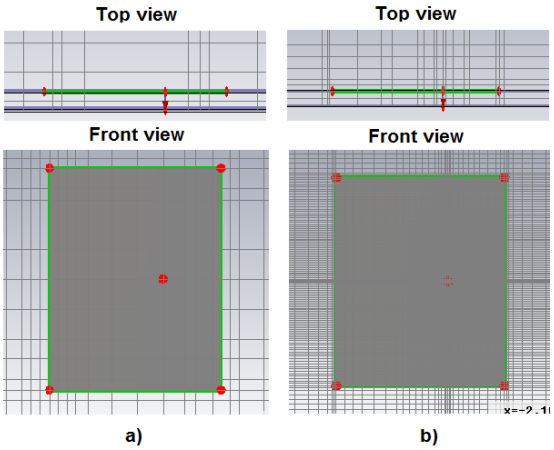

Figure 3. 7- Patch structure meshed with TD solver hexahedral mesh: a) without adaptive mesh refinement, b) with adaptive mesh refinement

An adaptive mesh refinement process is also available for the Time Domain solver. Figure 3. 7 shows the same patch structure as modelled in the previous subsection, meshed in the Time Domain solver with and without adaptive mesh refinement.

3.2.4 Convergence Study

The example design used in Section 3.2.2 and Section 3.2.3 is used here to perform a convergence study for each solver system. The study consists of simulating the same model with a range of meshes that gradually increase in fineness. When the results cease to change past a certain level of mesh fineness,

the mesh is considered to have converged and it is then known what quality of mesh is required to simulate the full electrical behaviour of the structure to the limit of the solution system's capability.

For this study, the mesh is considered to have converged when the resonant frequency of the $|S_{11}|_{dB}$ result does not shift by more than 0.5% (as a percentage of the measured resonance at 1.572GHz) between mesh iterations. The purpose of the study is to compare the three solvers' ability to converge on the correct resonant frequency, as well as the time required to do so.

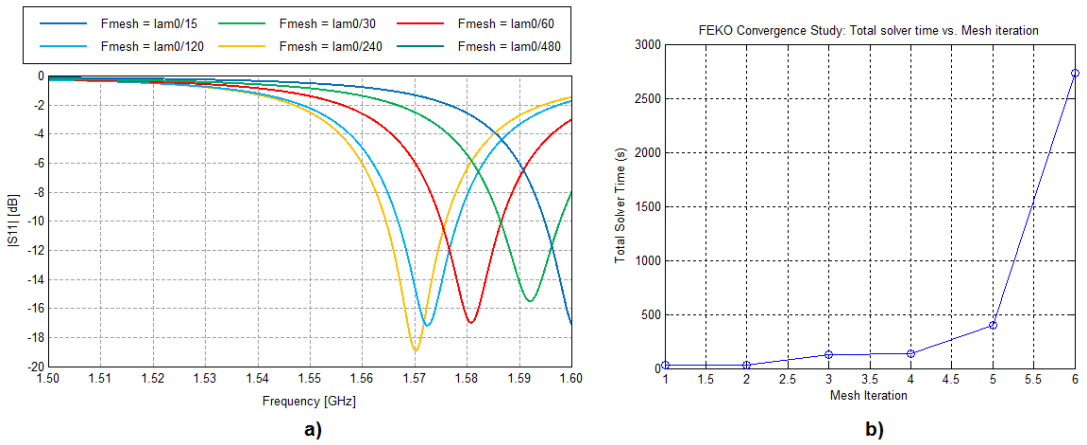

Figure 3.8- FEKO MoM solver convergence study, a) |S11|, b) Total solver time vs. mesh iteration

For FEKO's MoM solver, F_{mesh} is set to an initial value of $\frac{\lambda_0}{15}$ and doubled for each iteration of the study. The frequency sampling is set to the adaptive frequency sampling option, as is done for the CST solvers. Figure 3.8 shows the progression of $|S_{11}|_{dB}$ for each mesh iteration alongside total solver time required for each iteration. For Iteration 4 and 5 ($F_{mesh} = \frac{\lambda_0}{120}$ and $F_{mesh} = \frac{\lambda_0}{240}$ respectively), the results' resonances fall within 0.5% of one another, and the mesh is considered to have converged.

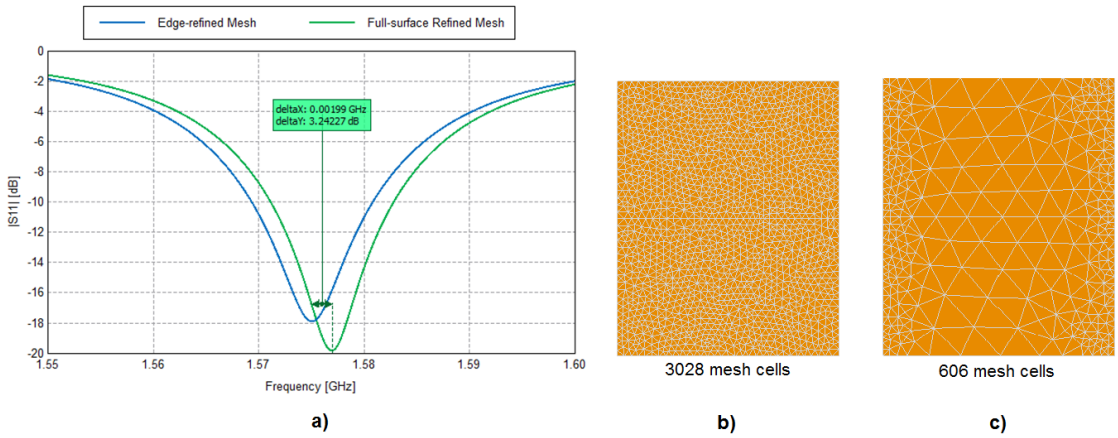

Figure 3.9- a) S_{11} of edge-refined mesh vs. full surface-refined mesh with $F_{mesh} = \frac{\lambda_0}{120}$, b) Full surface-refined patch mesh, c) edge-refined patch mesh

Figure 3.9a shows $|S_{11}|$ for the patch meshed with $F_{mesh} = \frac{\lambda_0}{120}$, as well as that of the patch meshed across its entire surface with the same refinement factor, while Figure 3.9b and Figure 3.9c show the corresponding surface meshes. It can be seen that the two meshes exhibit very similar resonances, separated in frequency by less than 0.02 GHz (0.13%). When one also considers that the full surface-meshed patch takes 2806.47s to solve versus the edge-refined patch's 127.16s, it becomes clear that the edge-refinement meshing scheme greatly improves the efficiency of the simulation with barely any loss of accuracy.

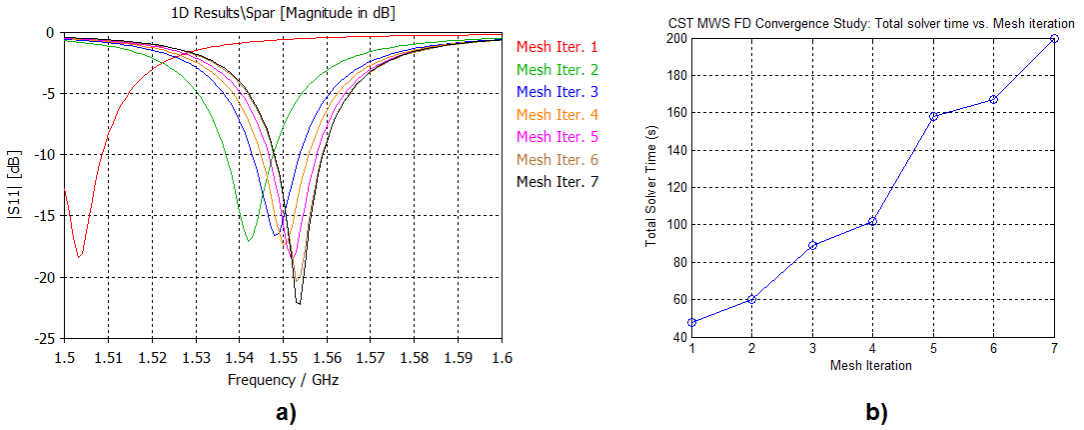

Figure 3.10- CST Frequency Domain solver convergence study, a) $|S_{11}|$, b) Total solver time vs. mesh iteration

For CST MWS' Frequency Domain solver, the adaptive mesh refinement feature is activated and its iterative results are used for the convergence study. Figure 3.10 shows the progression of $|S_{11}|_{dB}$ for each mesh iteration alongside total solver time required for each iteration. The resonant frequency can be seen to gradually converge towards 1.552 GHz; it should be noted that this is not the exact target resonance, and misses it by approximately 0.02GHz (1.27%). For a wideband patch design, this is not

a major issue, but for a narrowband design with a 1-2% FBW, it could mean that the design misses the desired frequency band completely. Iteration 6 and 7 share the converged resonant frequency, although from Iteration 4 the responses' resonant frequencies are all within 0.002 GHz (0.13%) of the converged frequency, and within 0.02 GHz of the actual target frequency. For practical purposes, the mesh is considered converged by Iteration 4.

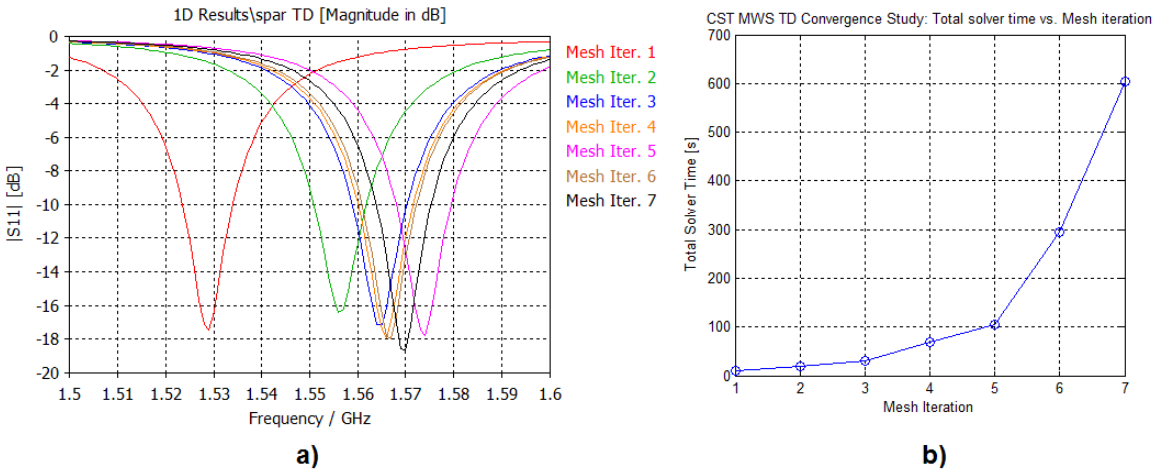

Figure 3.11- CST Time Domain solver convergence study, a) |S11|, b) Total solver time vs. mesh iteration

For CST MWS' Time Domain solver, the adaptive mesh refinement feature is also utilised. Figure 3.11- CST Time Domain solver convergence study, a) |S11|, b) Total solver time vs. mesh iteration shows the progression of $|S_{11}|$ for each mesh iteration alongside total solver time required for each iteration. The resonant frequency can be seen to gradually converge towards 1.57 GHz, whereas solver time can be seen to increase sharply after Iteration 5. Following Iteration 4, the resonances do not shift by more than 0.5%, and so the mesh is considered to have converged by Iteration 4.

3.3 Modelling of Aperture-fed Patch

The major components that are shared between a basic patch and an aperture-fed patch are modelled in exactly the same way, both in FEKO and CST MWS. The components specific to the aperture-fed patch (feed substrate, aperture, tuning stub and feed-line) are discussed in this section, and developed for each solver system.

In particular, the inclusion of an aperture can significantly complicate the meshing process. Fortunately, it is possible to overcome this issue in each solver system with the use of sensible modelling techniques.

3.3.1 FEKO MoM

The aperture-fed patch requires substrates to be placed above and below the ground-plane. Fortunately, the *Planar Multilayer Substrate* feature is able to add an arbitrary number of dielectric layers above and below the ground-plane without loss of accuracy.

The aperture can be modelled in two ways. The first option is to model an actual aperture in a ground-plane, but this cannot be used with the *Planar Multilayer Substrate* option and forces the ground-plane to be meshed explicitly. The second option is to use the *PGF Aperture* feature, which models some geometry coplanar with a PGF ground-plane as an aperture.

Table 3.1 - Cost comparison of FEKO MoM aperture modelling options at convergence

Ground/Substrate Type	Infinite (*PGF Aperture*)	Finite (Explicitly meshed)
No. of mesh cells	500	5616
Total solver time (s)	89.081	4102.116

Table 3.1 - Cost comparison of FEKO MoM aperture modelling options shows the computational cost of either aperture-modelling option, for a typical 4.7 GHz aperture-coupled patch antenna model. The explicitly-meshed ground-plane is meshed as coarsely as possible to save computational cost. The *Planar Green's Function (PGF) Aperture* feature is faster than an explicitly-meshed ground-plane with an aperture by a factor of 46, and requires ten times fewer mesh cells, making it the definite preferred modelling option.

The microstrip feed-line, like the patch, is modelled as a planar PEC surface of zero thickness. The feeding port is once again modelled with a *Microstrip* port. A minimum feed length of $\frac{\lambda_0}{8}$ is set to prevent unwanted electrical interaction between the port and the aperture.

3.3.2 CST MWS Solvers

While no special solution feature for apertures exist in CST MWS, both the Time and Frequency Domain solvers' volumetric solution methods are well-equipped to handle apertures in a ground-plane. Whereas the basic patch has its ground-plane modelled as a flat PEC surface, the aperture-coupled patch has the same with the aperture geometry subtracted from the ground-plane surface.

Since a microstrip feed-line is used as the input to the structure, the best port to use is the *Waveguide* port. The port is made ten times wider than the feed-line width, and five times higher than the feed substrate height to ensure the correct QTEM transmission mode is excited within the port.

Since two substrates are mounted on either side of the ground-plane for the aperture-coupled patch, the lower z-boundary cannot be made a PEC boundary. Instead, it is made *Open (Add Space)*.

3.3.4 Convergence Study

The convergence study is performed in the same way as that of Section 3.2.4. For this study, the example A2 in [30] is used as a target design, with the following specifications: $L_0 = 40$ mm, $W_0 = 30$ mm, $L_{ap} = 10$ mm, $L_{tune} = 11$ mm, $w_f = 1.16$ mm, $W_{ap} = 1.1$ mm, $h_0 = 1.575$ mm, $h_f = 1.27$ mm, $\varepsilon_{rp} = 2.22$, $\varepsilon_{rf} = 10.2$. The aperture-fed patch diagram of Chapter 2 is redrawn in Figure 3.12 for the sake of clarity.

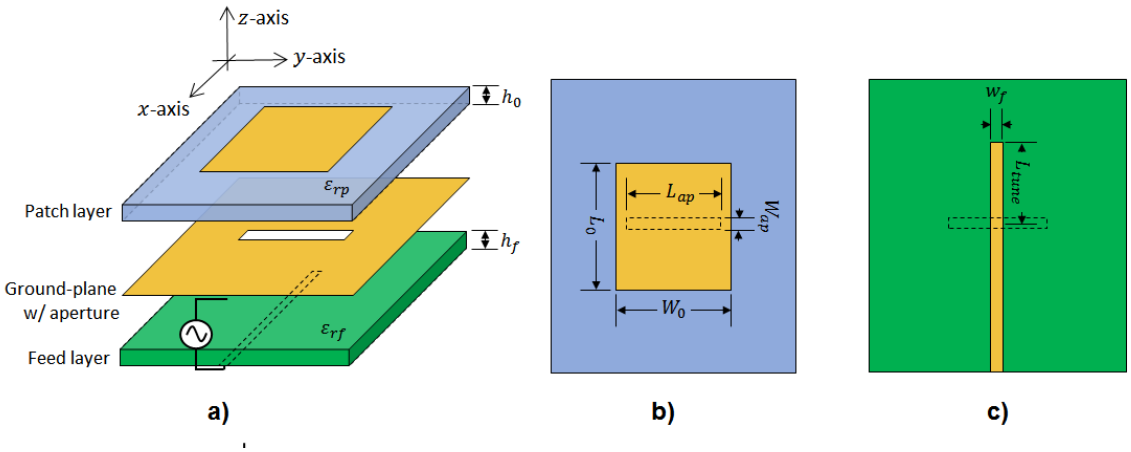

Figure 3.12 - Aperture-coupled patch antenna layout: a) Exploded isometric view, b) Top view, c) Bottom view

Seeing as the previous study already determined the best mesh for the patch surface, the main interest of this study is the aperture and feed-line. For FEKO MoM, The feed-line is studied in a separate model to determine its required mesh resolution. The line is to be meshed uniformly. The model consists of a half-wavelength microstrip line with the same width as the feed-line of A2 (1.16mm), terminated in a discrete 25Ω impedance. The model is compared to a closed-form solution implemented in AWR MWO 2010.

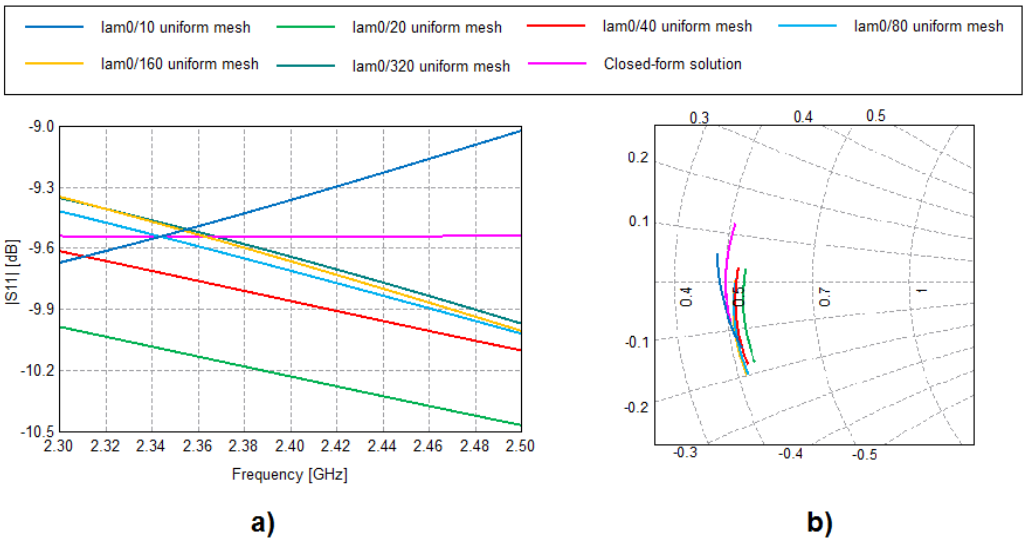

Figure 3.13 - FEKO MoM feed-line convergence study: a) $|S_{11}|$, b) Smith Chart

Figure 3.13a shows the progression of $|S_{11}|$ for each feed-line mesh iteration alongside total solver time required for each iteration, while Figure 3.13b plots the corresponding Smith Chart loci normalised to 50Ω. It is important, in this case, to note the position of the loci on the Smith Chart in order to determine how accurately the line length is simulated. All of the results are observed to be close to the closed-form solution, although the mesh only begins to converge at Iteration 6 ($\frac{\lambda_0}{320}$ mesh cell length). The converged impedance response is not exactly that of the closed-form response, but it remains roughly within a 0.3dB error margin across the sampled frequency band.

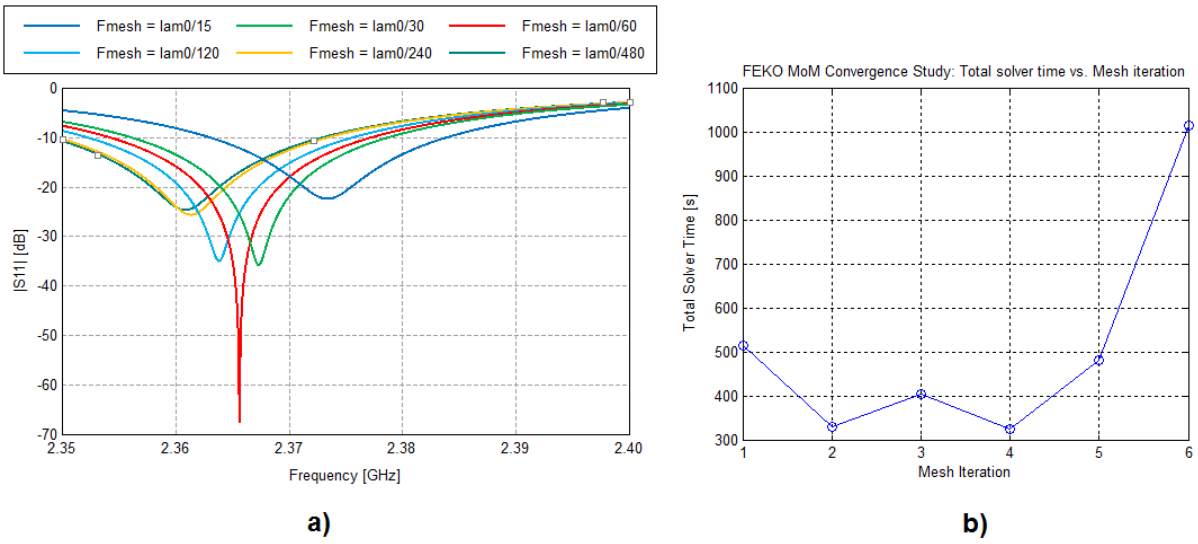

Figure 3.14- FEKO MoM convergence study, a) |S11|, b) Total solver time vs. mesh iteration

Having determined the feed-line's required mesh cell length $\left(\frac{\lambda_0}{320}\right)$, the only remaining mesh that must be developed is that of the aperture. The full model of the aperture-coupled patch antenna is used for

this study, with the patch and feed-line meshes set as the aperture mesh is varied. Figure 3.14 shows the progression of $|S_{11}|$ for each mesh iteration alongside total solver time required for each iteration. The mesh reaches convergence between Iteration 5 and 6 ($F_{mesh} = \frac{\lambda_0}{120}$ and $F_{mesh} = \frac{\lambda_0}{240}$ of Figure 3.14a, respectively), and converges with an error of 0.0137 GHz (0.58%) from the actual centre frequency of 2.375 GHz.

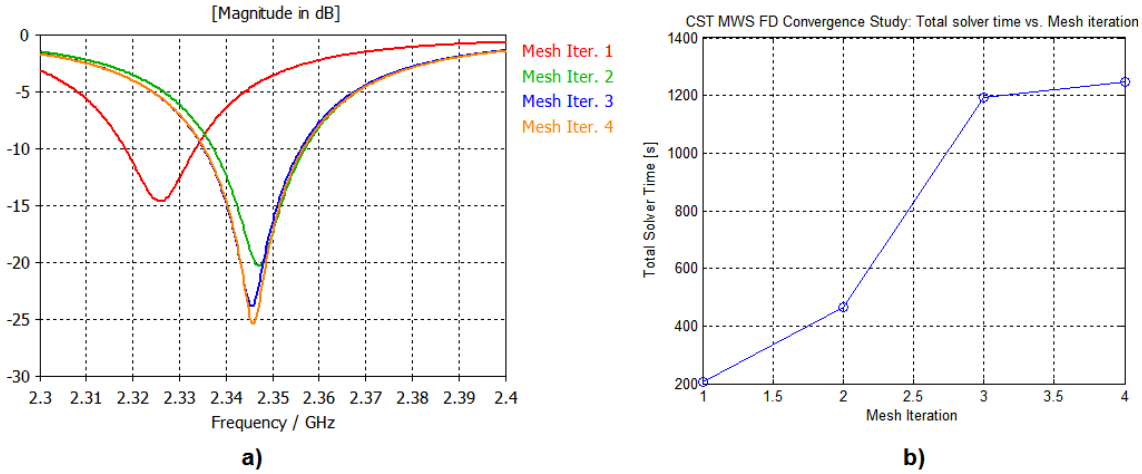

Figure 3.15 - CST MWS FD convergence study, a) |S11|, b) Total solver time vs. mesh iteration

For the CST MWS solvers, adaptive meshing is activated and the study is run on the entire aperture-coupled patch structure. Figure 3.15 shows the progression of $|S_{11}|$ for each mesh iteration alongside total solver time required for each iteration. The mesh reaches convergence between iteration 3 and 4, and converges with an error of 0.03 GHz (1.25%) from the actual centre frequency of 2.375 GHz.

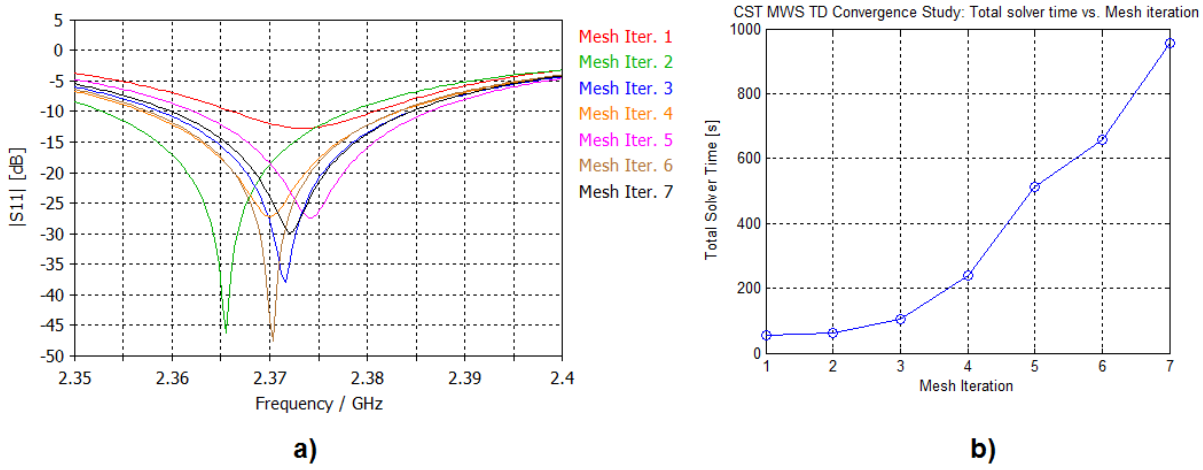

Figure 3.16 - CST MWS TD convergence study, a) |S11|, b) Total solver time vs. mesh iteration

Figure 3.16 shows the progression of $|S_{11}|$ for each mesh iteration alongside total solver time required for each iteration, for the Time Domain solver. From Iteration 3 onwards, the resonant frequency of

each iteration does not move out of the 2.37-2.375 GHz (FBW = 0.2%) band, and so the mesh is considered to have converged with a resonant frequency error of less than 0.2%.

3.4 Performance Summary

Table 3.2 is a summary of the three solvers' performances, each at a state of mesh convergence. The results are tabulated for both the basic and aperture-fed patch structures, and their computational cost as well as their relative accuracy is given. The solvers' accuracy is measured by the percentage error of their resonant frequencies from the actual target frequencies (1.572 GHz for the basic patch and 2.375 GHz for the aperture-fed patch).

Table 3.2 - EM solver performance summary

	FEKO MoM		CST MWS FD		CST MWS TD	
Patch Type	Solver Time (s)	Freq. Error (%)	Solver Time (s)	Freq. Error (%)	Solver Time (s)	Freq. Error (%)
Basic	209.4	0.19	102	1.27	604.7	0.13
Aperture-fed	481.6	0.58	1191	1.25	224.6	0.2

The results of the convergence study show that the CST MWS Time Domain solver produces the most accurate result for both patch geometries, although it has the longest solver time for the basic patch. The Frequency Domain solver consistently produces the least accurate results, and is by far the slowest to simulate the aperture-fed patch.

It is decided that FEKO MoM will be used to simulate the full-wave models of Chapter 5 and Chapter 6, for several reasons. Firstly, it produces reasonably accurate results for a reasonable computational cost. Secondly, it is simple to access from an environment such as MATLAB, where the optimisation procedure of Chapter 6 will be run from. The combination of its relatively good solver performance and accessibility from an external software environment makes FEKO MoM the first choice of full-wave solver.

3.4 Practical Substrate Modelling

While it is highly efficient to model the substrate and ground-plane as infinite structures, it is not quite practical. If it is desired to minimise the substrate size, then the use of an infinite substrate will produce increasingly inaccurate results as the distance between the patch and substrate edges shrinks. The design process of this thesis does not intend to minimise the substrate quite so drastically, as the resultant fringing fields at the substrate edges would severely complicate the modelling of a functioning coarse transmission-line model of the patch. Instead, the substrate must be kept large enough so that the patch behaves as if it were on an infinite substrate, but only as large as is necessary for the sake of reducing

manufacturing cost. If the design is approached in this manner, the patch can then be designed on an infinite substrate, and the actual size of the practical substrate can be subsequently optimised.

Table 3.3 - Performance comparison for finite-substrate basic patch

Solver Type	Total solver time [s]
FEKO MoM	32793
CST MWS FD	141
CST MWS TD	635.6

While FEKO MoM is capable of handling infinite planar structures, it is not well-suited to efficiently simulate a finite ground-plane and dielectric regions. Table 3.3 compares the computational cost required for each solver to run the basic patch simulation of Section 3.2, but with a finite substrate and ground-plane. The dimensions of the substrate/ground-plane are set to twice those of the patch. The results show that it is FEKO MoM requires a prohibitively long solver time to run even one iteration of the finite-substrate structure, whereas either CST MWS solver is able to run the same structure 50 times faster.

The full design procedure of Chapter 7 further addresses the optimisation of the entire array's substrate size, using the CST MWS Time Domain solver.

3.5 Full-wave Coarse Modelling

The Space mapping (SM) optimisation process detailed in Chapter 6 involves the use of fine- and coarse-fidelity models. The full-wave models developed in the previous sections are intended for use as fine models, and their coarse counterparts must still be developed.

The formulation of a coarse model is primarily concerned with attaining the fastest possible model, without sacrificing the underlying electrical behaviour of the structure being modelled. In principle, a coarsely-meshed model should still behave somewhat like its fine counterpart regardless of how coarse the mesh is, unless some physical feature of the model is completely removed or a highly sensitive electrical characteristic is affected. The patch structures under consideration are composed of mostly simple shapes with robust electrical characteristics, and their response features would likely survive a coarse meshing scheme. However, the aperture structure is one component that must be handled with care, as was seen in the convergence study of Section 3.3.4.

In general, coarse models exhibit specific errors in their responses that reflect the nature of the mesh used. For instance, a patch surface that is too coarsely meshed appears electrically longer than it actually

is, resulting in its response having a lower-frequency resonance than it should. The aperture, however, is not just a resonator but a strong through-coupling mechanism that can severely affect the entire shape of the aperture-coupled patch's frequency response, if it is not correctly meshed. The convergence study of Section 3.3.4 illustrates this issue.

Chapter 5 further investigates the issue by practically applying coarse full-wave models to an SM process. The convergence studies of this chapter provide a progressive set of reference results with which suitable coarse models can be constructed.

3.6 Conclusion

In this chapter, a thorough study of the available full-wave EM solver options has been performed and analysed. The three solution systems (FEKO MoM, CST MWS Frequency Domain solver and CST MWS Time Domain solver) have been described in function and capability, and have been applied to the modelling of basic and aperture-fed patch antenna structures' impedance characteristics. Their computational cost and accuracy have been quantified for each modelling problem, and convergence studies have been performed for the structures. The issue of modelling a finite substrate has also been discussed, as well as that of extracting coarse models from the results obtained in this chapter. This chapter serves as a foundation for the formulation of the fine models used in Chapter 5's optimisation procedures.

Chapter 4

Transmission-line Modelling of Patch Antenna Elements

The crux of the design method proposed in this thesis involves the use of fast *transmission-line models* to be optimised in place of slow full-wave models. This chapter provides an exposition of the patch antenna TLMs used in this thesis, as well as a set of validation experiments in an attempt to determine their applicability to a variety of patch antenna design problems.

The TLMs developed in this chapter are all constructed and simulated in AWR Microwave Office (MWO) 2010. MWO is particularly well-suited to high-frequency applications and has extensive libraries for microstrip structures, many of which have efficient closed-form solutions.

4.1 Basic Edge-fed Patch TLM

Section 2.2.1.2 laid out the fundamentals of the patch antenna's TLM, representing the patch with a transmission-line terminated in identical edge networks NW_p. It was also stated that NW_p models the patch's radiation and the reactive fringing fields at the radiating edges. In this section, NW_p is developed in detail with two proposed models, and their performance is compared relative to a finely-meshed full-wave model.

4.1.1 Edge Network NW_p – Balanis Model

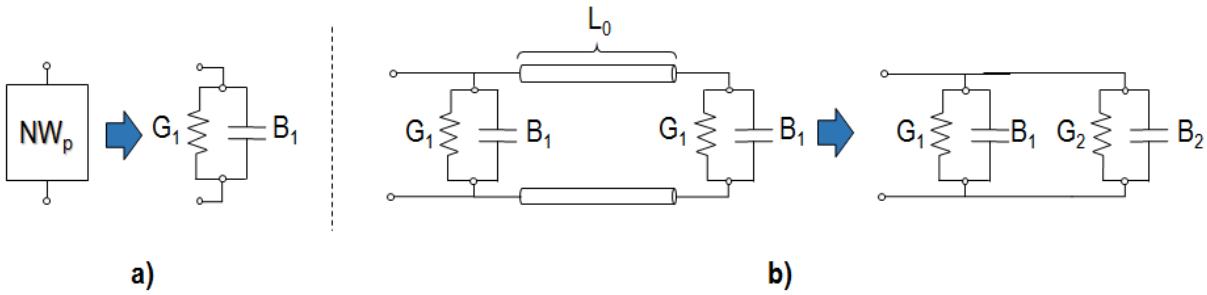

Figure 4.1- a) NW_p as complex shunt admittance Y_1, b) Full patch TLM and transformation to dual shunt admittances Y_1 and Y_2

Figure 4.1a shows the circuit of NW_p, as proposed in [20]. The circuit is composed of a simple shunt admittance $Y_1 = G_1 + jB_1$. Specifically, G_1 represents the radiation at the patch edges, while jB_1 represents their capacitive fringing fields. If $\frac{h_0}{\lambda_p} < 0.1$, Y_1 is given by:

$$Y_1 = G_1 + jB_1 \qquad (4.1)$$

where

$$G_1 = \frac{W_0}{120\lambda_p}\left(1 - \frac{1}{24}(k_0 h_0)^2\right) \quad (4.2)$$

$$B_1 = \frac{W_0}{120\lambda_p}\left(1 - 0.636\ln(k_0 h_0)\right) \quad (4.4)$$

L_0, W_0 and h_0 are the patch dimensions and λ_p is the patch's resonant wavelength, as defined in Chapter 2. The wavenumber k_0 at resonance is given by:

$$k_0 = \omega_0\sqrt{\mu_0 \varepsilon_0 \varepsilon_{rp}} \quad (4.5)$$

where ω_0 is the resonant radian frequency, as defined in Chapter 2.

A series transmission line of length L_0 separates the two admittances, and represents the E-plane distance between the radiating edges. The input admittance of the patch is given by $Y_{in} = Y_1 + Y_2$, where $Y_2 = G_2 + jB_2$ is the combined admittance of the transmission-line and rightmost edge admittance. Y_2 can be found by transforming the right-hand edge admittance through the transmission-line length L_0 [15]:

$$Y_2 = \frac{1}{Z_{in2}} = \frac{Z_0 + jZ_1\tan(\beta L_0)}{Z_0(Z_1 + jZ_0\tan(\beta L_0))} \quad (4.6)$$

where Z_{0p} and β_p are the characteristic impedance and propagation constant of the patch transmission-line, respectively.

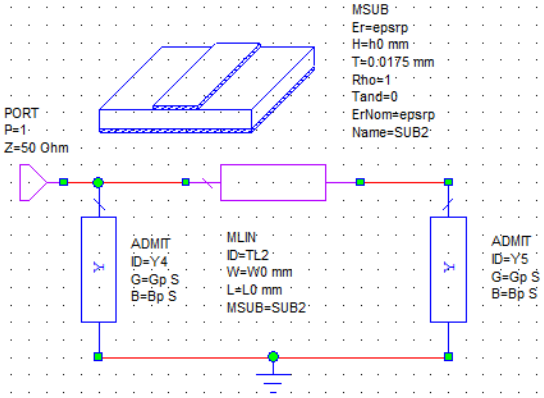

Figure 4.2- Balanis' edge-fed basic patch TLM implemented in AWR MWO 2010

Figure 4.2 shows the edge-fed basic patch TLM using Balanis' NW_p, modelled in MWO. The transmission-line is implemented with a MLIN microstrip line element, while the shunt admittances are built with an ADMIT general complex admittance. MSUB defines the substrate on which MLIN is

placed. While an ideal transmission-line could be used in place of MLIN, the use of MLIN provides a more accurate representation of the patch as a microstrip structure, and reduces the level of abstraction in the TLM.

This formulation of NW_p is simple and intuitive, and is easy to implement in a circuit-solver or with a MATLAB script. However, its simplicity may also lead to inaccuracy in the TLM. The following subsection considers a more sophisticated model, in an attempt to determine whether Balanis' straightforward formulation of NW_p can be improved upon.

4.1.2 Edge Network NW_p – Jaisson Model

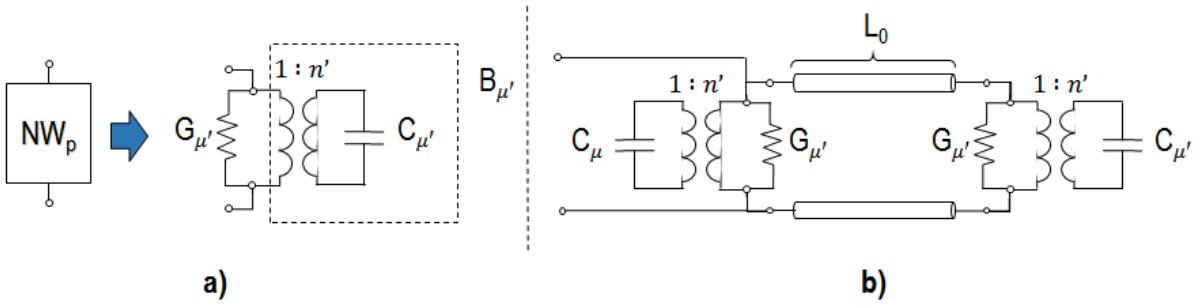

Figure 4.3 – Jaisson's model of NW_p, b) Full patch TLM

Figure 4.3 shows the model of NW_p as developed and explained in [31]. The model consists of a shunt conductance $G_\mu{}'$ and a shunt susceptance $jB_\mu{}'$, where $jB_\mu{}'$ is modelled as a $1{:}\,n'$ ideal transformer and a shunt capacitance C_μ. The conductance and susceptance are given by:

$$G_\mu' = (1 + F_G)G_\mu \tag{4.7}$$

$$B_\mu' = (1 + F_b K_b)B_\mu \tag{4.8}$$

In the above equation, B_μ is the susceptance of C_μ. The remaining terms F_G, G_μ, F_b, K_b and are given by [31]:

$$F_G = \mathrm{J}_0(\Theta_l) + \left(\frac{{\Theta_h}^2}{a}\right)\mathrm{J}_2(\Theta_l) \tag{4.9}$$

$$G_\mu = \frac{a\left[\Theta_w\,\mathrm{Si}(\Theta_w) + \frac{\sin\Theta_w}{\Theta_w} + \cos\Theta_w - 2\right]}{24\pi Z_0} + \frac{{\Theta_h}^2\left[0.333 + \left(\cos\Theta_w - \frac{\sin\Theta_w}{\Theta_w}\right){\Theta_w}^{-2}\right]}{12\pi Z_0} \tag{4.10}$$

$$F_b = \frac{\pi\left[\mathrm{Y}_0(\Theta_l) + \left(\frac{{\Theta_h}^2}{a}\right)\mathrm{Y}_2(\Theta_l)\left(24 - {\Theta_h}^2\right)^{-1}\right]}{2\left(\log(\Theta_h) - 1.616 + \frac{{\Theta_h}^2}{12a}\right)} \quad (4.11)$$

$$K_b = 1 - e^{-0.21\Theta_w} \quad (4.12)$$

where $\mathrm{J}_n(x)$ and $\mathrm{Y}_n(x)$ are the n^{th}-order Bessel functions of the first and second kind, respectively [32]. The terms Θ_l, Θ_h and Θ_w are given by [31]:

$$\Theta_l = k_0(L_0 + 2h_0) \quad (4.13)$$

$$\Theta_h = 2k_0h_0 \quad (4.14)$$

$$\Theta_w = k_0 \quad (4.15)$$

Finally, the transformer turns ratio n' is given by:

$$n' = \sqrt{1 + F_bK_b} \quad (4.16)$$

The shunt capacitance C_μ is representative of the fringing fields at the patch edges, and is typically modelled by a closed-form microstrip end-effect element common in many microwave-frequency circuit solvers [31].

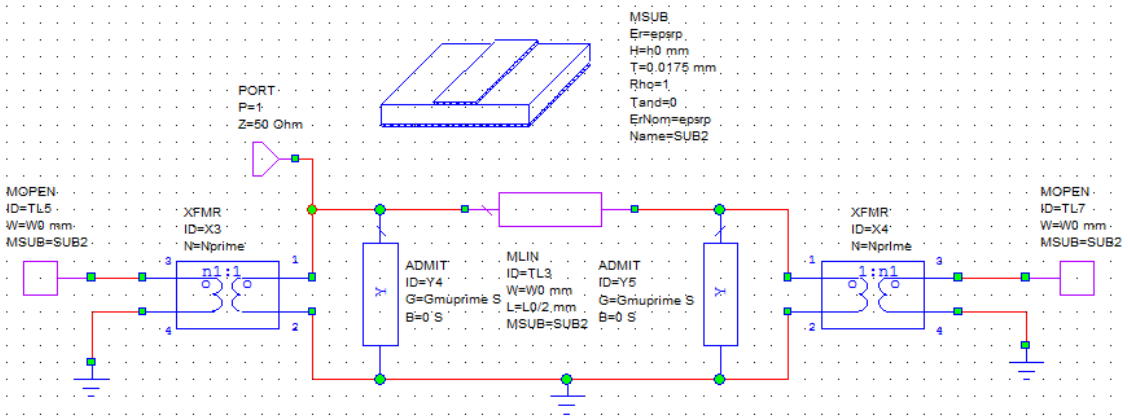

Figure 4.4 - Jaisson's edge-fed basic patch TLM implemented in AWR MWO 2010

Figure 4.4 shows the edge-fed basic patch TLM using Jaisson's NW_p, modelled in MWO. The MLIN element is again used to model the microstrip line, ADMIT models G'_μ, The XFMR two-port network is used to model the ideal transformer and MOPEN models C_μ.

This model is more complex than Balanis' TLM, and requires more sophisticated circuit elements, but they are all implemented as closed-form solutions and are not expected to be noticeably less efficient than the implementation of Balanis' TLM. The following section will consider the two models' relative efficiency as a factor in their overall usefulness.

4.1.3 Model Validation- TLM Experiment 1

In order to decide which model of NW_p is to be used in the optimisation process of Chapter 6, the performance of each TLM is evaluated and compared to a finely-meshed EM model. The EM model is implemented in FEKO 7.0, and is meshed according to the convergence study of Chapter 2. All of the models are sampled at 31 frequency points in the range of 2.1-2.7 GHz. The study is conducted on a set of patches designed to resonate about 2.4 GHz, and is performed across a range of patch substrate permittivities ε_{rp} and heights h_0.

Upon inspection of Equations (2.4-2.6), it is seen that the resonant frequency of basic patch antenna is dependent on both ε_{rp} and h_0. It is desired to observe the TLMs' effectiveness near the 2.4 GHz target resonance, and if ε_{rp} and h_0 are varied, then the patch will clearly not remain at resonance for only a single calculation of L_0. Therefore, for each combination of ε_{rp} and h_0, the length of the patch is recalculated to produce resonance at 2.4 GHz, using Equation (2.13).

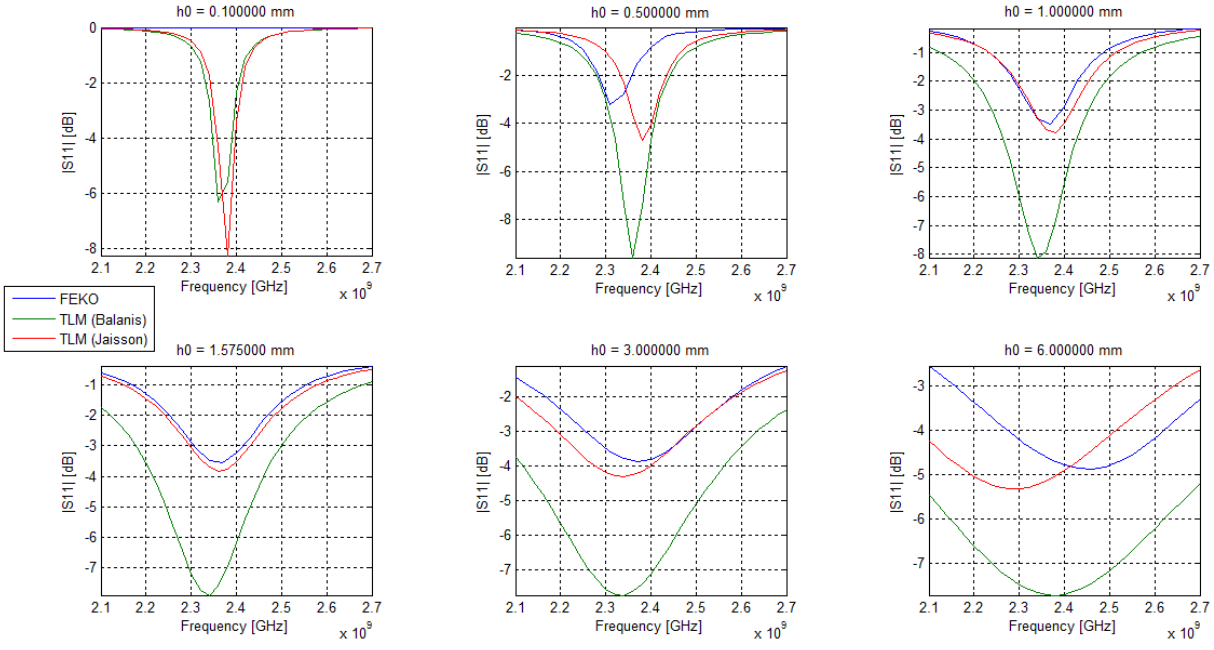

Figure 4.5 - S11 comparison of Edge-fed patch TLMs ($\varepsilon_{rp} = 1$)

Figure 4.5 shows the $|S_{11}|$ responses of Balanis' TLM, Jaisson's TLM and the FEKO fine model, for $\varepsilon_{rp} = 1$ and $h_0 = [\![0.1; 0.5; 1; 1.575; 3; 6]\!]$ mm. For $h_0 = 0.1$ mm, both TLMs fail, but for the remaining simulations, Jaisson's TLM consistently produces a response more accurate in magnitude

than Balanis' TLM. Furthermore, Jaisson's TLM produces a more accurate resonant frequency than Balanis' for three of the five remaining simulations ($h_0 = [\![1; 1.575; 3]\!]$ mm); in fact, Jaisson's TLM is remarkably accurate to the FEKO response for these three cases. The results imply, at least for $\varepsilon_{rp} = 1$, that Jaisson's TLM is the more accurate model, excepting a mismatch in resonant frequency for very small or large values of h_0.

Appendix A contains the rest of the validation study's results, for $\varepsilon_{rp} = [\![1; 1.5; 2.2; 3; 3.5]\!]$ and the same range of h_0. The trend observed in Figure 4.5 remains consistent for the full set of responses, although Balanis' TLM does appear to increase in accuracy for higher values of ε_{rp}. In general, however, Jaisson's TLM is the more reliable choice, and performs adequately over a wide set of practical substrate parameters.

Table 4.1 - Model validation: Solution time comparison

Model	Solver Time [s]
Balanis' TLM	0.354
Jaisson's TLM	0.369
FEKO fine model	209.4

Table 4.1 is a comparison of the total solver time required for each model, for the 31 discrete frequency points used in the validation study. Both TLMs are shown to be faster than the corresponding FEKO fine model by a factor larger than 500, which makes them good candidates to use in large-scale global optimisation or surrogate-based optimisation. Moreover, Jaisson's TLM is shown to be closely accurate to the FEKO fine model, and as expected, it is as efficient as Balanis' TLM.

In summary, Jaisson's TLM is proven to function well as a fast and accurate approximation of the slower full-wave model, for the studied set of substrate parameters. Of the two TLMs considered, Jaisson's TLM is consistently the most accurate without any loss of efficiency. Even in cases where the TLM loses some of its accuracy, its underlying behaviour seems to mimic that of the full-wave model, and an optimisation technique such as Space mapping could possibly correct the error between the models.

4.2 Aperture-fed Patch TLM

Figure 4.6 shows the transmission-line model of the aperture-coupled patch [33] [34] [35]. As is shown in Figure 4.6b, the model can be divided into three distinct parts that account for the parts of the structure (feed-line, aperture and patch).

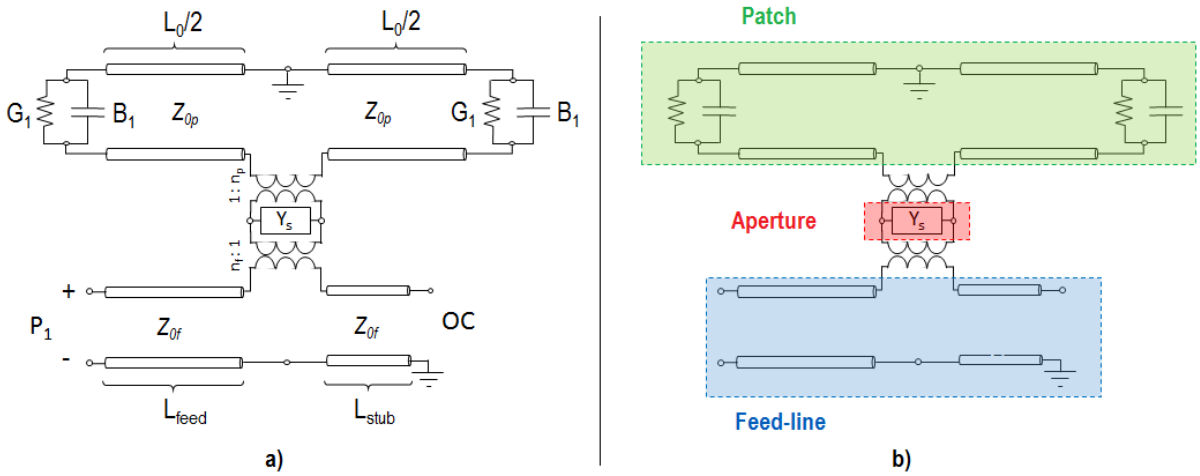

Figure 4.6- a) Aperture-coupled patch antenna TLM, b) Component regions

The feed-line is simply modelled as two transmission-lines of characteristic impedance Z_{0f}, with the right-hand line of length L_{stub} terminated in an open-circuit to represent the tuning stub.

The aperture is modelled simply as an admittance Y_s connected in shunt between the transformer terminals, and represents the reactive energy stored around the aperture. The calculation of the value of Y_s is nontrivial, and is further discussed in the next subsection.

The patch antenna is represented by the same transmission-line model as in Figure 4.3, with the exception of the feed point. In this case, the patch is fed at its centre from the aperture, and thus the single transmission line of length L_0 is replaced with two lines of length $\frac{L_0}{2}$, which each represent one half of the patch surface.

A transformer with a turns ratio of $n_f:1$ is placed in series between the two lines to represent the coupling between the feed-line and the aperture. Similarly, the coupling between the patch and the aperture is represented by a transformer with a turns ratio of $n_p:1$. As is the case with the aperture admittance, the calculation of the turns ratios is an involved process and is discussed in a following subsection.

4.1.1 Aperture Admittance

Several methods have been developed that attempt to characterise the admittance of the coupling aperture [35] [34] [36] [37]. These approaches are summarised in [30], and their applicability to the physical problem of an aperture-coupled antenna is briefly discussed. The article further proposes its own solution to the aperture admittance, which takes into account the limitations of the other methods and attempts to overcome them. This subsection is a brief exposition of the pertinent sections of [30], where the aperture admittance is derived.

The method of [30] makes use of the Reciprocity and Equivalence theorems of electromagnetic field theory [7]. It is an attempt to simplify [36], which makes extensive use of Green's functions and is a computationally expensive procedure. In this method, the aperture's stored and radiated energy is modelled by two radiating strips of magnetic current density $2\boldsymbol{M}_s^{\pm}$ situated just above and below the aperture surface ($z = 0^+$ and $z = 0^-$, respectively). The strips individually account for the fields on the feed-side and patch-side of the aperture, and each strip is embedded in a dielectric slab with height and dielectric constant equal to that as illustrated in Figure 4.7:

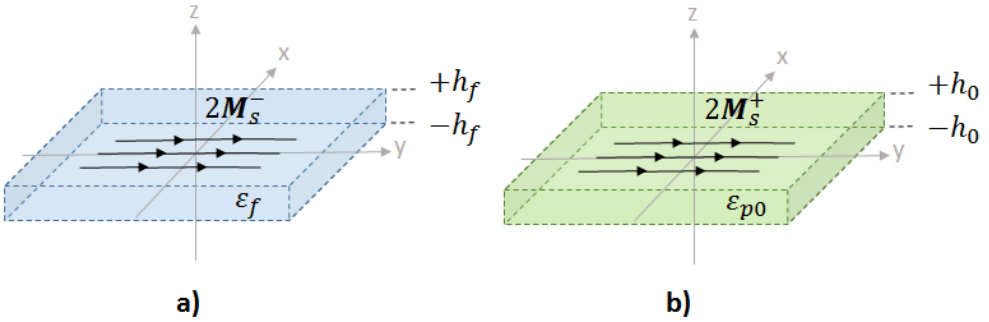

Figure 4.7 - Aperture Magnetic Currents: a) Feed-side (z = 0⁻), b) Patch-side (z = 0⁺)

The aperture admittance is defined as $Y_s = Y^+ + Y^-$, where $\frac{Y^{\pm}}{2}$ is the input admittance of the magnetic current densities $2\boldsymbol{M}_s^{\pm}$. The work in [30] defines Y^- as:

$$\frac{Y^-}{2} = \frac{Z_{wi}}{{Z_0}^2} \qquad (4.17)$$

Z_0 is the wave impedance of free space, whereas Z_{wi} is the input impedance of the magnetic current density strip $2\boldsymbol{M}_s^{\pm}$. Z_{wi} is further defined by [38] as being equal to the mutual impedance of two parallel thin-wire dipoles of length L_s, separated by a distance a:

$$Z_{wi} = Z_{12}(a)$$

$$= \frac{Z_0\left[2(2+\cos\Theta)\boldsymbol{E}(\Theta_0) - 4\cos\Theta\left(e^{j\Theta}\boldsymbol{E}(\Theta_1) + e^{-j\Theta}\boldsymbol{E}(\Theta_{-1})\right) + e^{j2\Theta}\boldsymbol{E}(\Theta_2) + e^{-j2\Theta}\boldsymbol{E}(\Theta_{-2})\right]}{4\pi\sin^2\Theta} \qquad (4.18)$$

where Θ, Θ_m and $\boldsymbol{E}(x)$ are given by:

$$\Theta = \frac{k_0 L_{ap}}{2} \qquad (4.19)$$

$$\Theta_m = \Theta\left(\sqrt{m^2 + \left(\frac{2W_{ap}}{L_{ap}}\right)^2} + m\right) \qquad m \in 0,1,2 \qquad (4.20)$$

$$\boldsymbol{E}(x) = Ci(x) - jSi(x) \qquad (4.21)$$

In the above equations, W_{ap} is the aperture width, and $Ci(x)$ and $Si(x)$ are the cosine and sine integral functions respectively. $Ci(x)$ and $Si(x)$ are given by [39] [40]:

$$\begin{aligned} Ci(x) &= \int_x^{\infty} \frac{\cos(t)}{t} dt \\ Si(x) &= \int_0^{x} \frac{\sin(t)}{t} dt \end{aligned} \qquad (4.22)$$

The sine and cosine integral functions may also be expressed in series-expansion form [39] [40]:

$$Ci(x) = \gamma + \ln(x) + \sum_{k=1}^{\infty}\left(\frac{(-x^2)^k}{2k(2k)!}\right) \qquad (4.23)$$

$$Si(x) = \sum_{k=1}^{\infty}\left((-1)^{(k-1)}\frac{x^{(2k-1)}}{(2k-1)(2k-1)!}\right) \qquad (4.24)$$

where γ is the Euler-Mascheroni Constant [41]. The series expansion forms are used to numerically approximate the sine and cosine integrals in the TLM, implemented in MATLAB and MWO. It is found that $Ci(x)$ can be truncated to 15 expansion terms with acceptably accurate results, and $Si(x)$ to 20 terms.

Of the options discussed, the model developed in [30] is of greatest interest, and is fully capable of being built and simulated in a solver system such as MWO. This particular model also contains integrated formulations of the transformer turns ratios that account for the feed-to-aperture and aperture-to-patch coupling, and so the entire model is considered as a whole to apply to the aperture-coupled patch TLM. The following subsection details the calculation of the turns ratios n_p and n_f.

4.1.2 Coupling Transformer Turns Ratios

The transformer turns ratios n_p and n_f represent the coupling of the feed to the patch, through the aperture in the ground-plane. The feed-to-aperture coupling is approximated by [30]:

$$n_f \cong \frac{2G(w) - G(w+l) - G(w-l)}{2\pi wl} \qquad (4.25)$$

where:

$$G(x) = (1 - x^2) \cdot \tan^{-1}(x) + x \cdot \ln(1 + x^2) \quad (4.26)$$

$$w = \frac{w_f}{2h_f} \quad (4.27)$$

$$l = \frac{L_{ap}}{2h_f} \quad (4.28)$$

In the above equations, w_f is the width of the feed-line and h_f is the height of the feed substrate.

The aperture-to-patch coupling is given by [30]:

$$n_p = \frac{L_{ap}}{2 \cdot w'_{eff}} \quad (4.29)$$

where w'_{eff} is the width of a parallel-plate waveguide with height h_0 and characteristic impedance Z_{0p}:

$$w'_{eff} = \sqrt{\frac{\mu_0}{\varepsilon_0 \varepsilon_{rp}}} \cdot \left(\frac{h_0}{Z_{0p}}\right) \quad (4.30)$$

4.1.3 Model Validation

The example design labelled A2 in [30] is considered here as the first step in validating the accuracy of the aperture-coupled patch TLM. The patch is designed to resonate at 2.4 GHz and has the following specifications: $L_0 = 40mm$, $W_0 = 30mm$, $L_{ap} = 10$ mm, $L_{tune} = 11$ mm, $W_{ap} = 1.1$ mm, $w_f = 1.16$ mm, $\varepsilon_{rf} = 10.2$, $\varepsilon_{rp} = 2.2$, $h_f = 1.27$ mm and $h_0 = 1.575$ mm.

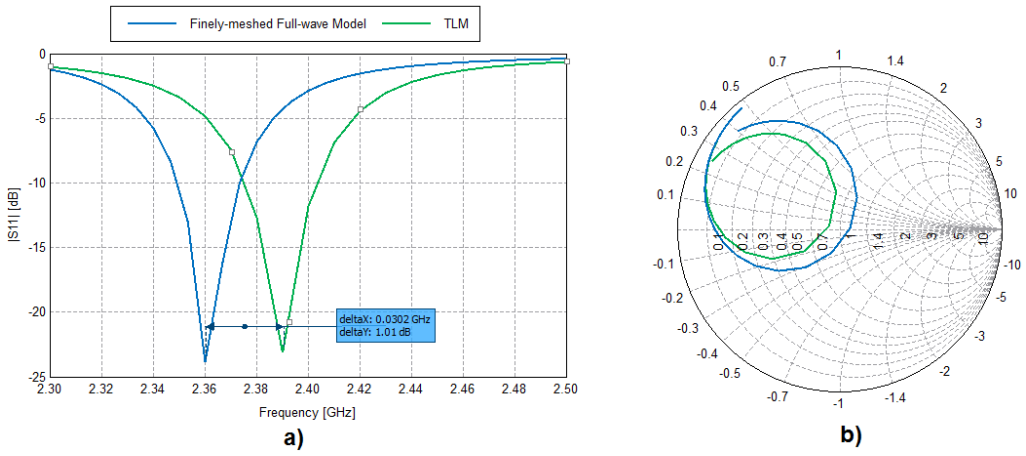

Figure 4.8- TLM vs. finely-meshed full wave model impedance response: a) |S11|, b) Smith Chart

Figure 4.8 shows the TLM's $|S_{11}|$ and Smith chart responses for A2, as well as those of a finely-meshed full-wave model to compare against the TLM's response. The full-wave model is implemented in CST MWS 2015's Time Domain solver, and is meshed according to the convergence study of Section 3.3.4.

The TLM's response can be seen to have an almost identical response form to the full-wave response, and its only distinct difference is that the response is shifted in frequency by 0.03 GHz (a 1.27% deviation from the full-wave resonant frequency). The TLM, at least for this specific substrate combination, is thus shown to perform well as a surrogate for the full-wave model, and would require only small adjustments to match its response to the full-wave response.

4.3 Conclusion

In this chapter, the transmission-line models for the basic and aperture-fed patch have been developed and tested through a set of validation experiments. The models proved to run many times faster than a full-wave model, and are acceptably accurate for the parameters under which the models have been tested. Implementations for the models in the AWR MWO environment were also provided, as they will be implemented in the optimisation procedures of Chapter 5 and Chapter 6.

Chapter 5

Optimisation Framework

In the solution of the complex design problems, it is common practice to make use of optimisation techniques at various stages of the design. Where analytic solutions are not available or ill-conditioned for a specific problem, the judicious use of an optimiser can often yield the desired results. Through the use of an appropriate method and a suitable control of the optimisation parameters, a local or global optimum can be found without excessive computational cost.

This thesis is primarily focused on the use of surrogate-based optimisation (SBO) and Space mapping (SM) techniques [42]. Hence, this chapter is largely devoted to a development of SM theory and its application to the design of a one-dimensional patch antenna array. Nonetheless, SM relies on the use of some or other direct optimisation method, and so the section on SM theory is prefaced with a discussion of local and global direct optimisation techniques.

5.1 Local vs. Global Optimisation

Optimisation, as is regarded within the context of this thesis, is the systematic minimisation/maximisation of a real-valued function given a set of real-valued inputs, with each input value constrained to some upper and lower bound. Note that only a single function is to be maximised/minimised, and hence this thesis exclusively considers *single-objective* optimisation techniques.

Optimisation algorithms can generally be categorised either as *local* or *global* searches. Local searches tend to limit themselves to some subspace around the input's start-values, often through some form of convergence mechanism. Global searches, conversely, combine convergence with an exploration trait that continues to search for a global optimum even after the algorithm converges on a perceived optimum.

The choice of whether to use local or global optimisation relies on the problem under consideration. In terms of computational cost, a local technique will almost always be cheaper than a global technique. The use of a local technique, however, is only useful if one is confident that a satisfactory response exists close to the chosen start-values of the inputs. If such a response is not found, or if it is in fact desired that the *global* optimum be found, then a global search must be used. Effectively, a local search is desirable unless it is certain to fail, and a global search is the more exhaustive yet costly alternative. The design procedure developed in this thesis makes use of both global and local searches, where they are found to be best-suited to a particular task.

5.1.1 Nelder-Mead Simplex Algorithm

The Nelder-Mead Simplex algorithm is the local optimiser of choice within the context of this thesis. The algorithm is a direct search method that operates on single-objective optimisation problems accepting n input parameters, and generates a simplex of $n + 1$ points spanning all dimensions of the parameter space [43]. For a nonzero set of starting input values $\boldsymbol{x_{init}} = [x_{init\cdot 1}, x_{init\cdot 2} \dots x_{init\cdot n}]^T$, the initial simplex's vertices are composed of the starting input vector and n points generated by adding 5% of each starting input to the starting input vector. An exemplary illustration of such an initial simplex is given in Figure 5.1.

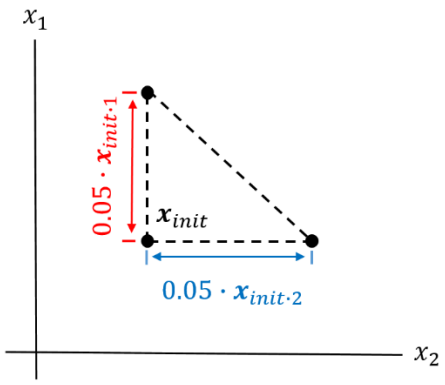

Figure 5.1 – Example of Nelder-Mead initial simplex generation ($n = 2$)

Once an initial simplex has been established, the algorithm iteratively traverses the local parameter space with a set of conditions that either expand, reflect, shrink or contract the simplex until a suitable termination criterion is met [43]. In this work, the Nelder-Mead simplex algorithm is implemented through the *fminsearch* MATLAB function.

5.1.2 Population-based Incremental Learning

Population-based Incremental Learning (PBIL) is the global optimiser of choice within the context of this thesis. PBIL combines aspects of genetic algorithms and competitive learning, and is implemented in an algorithm that is simpler in structure than most genetic algorithms [44]. A range of test problems have been executed for which PBIL is shown to be capable of outperforming standard genetic algorithms [45].

In the PBIL algorithm, the constrained parameter space under consideration is mapped to a binary bit vector. The number of bits in the vector determine how finely the parameter space is discretised into regions. In this work, only real-valued parameter spaces are considered, although PBIL itself is not limited to operating on parameter spaces composed of a set of real numbers.

A real-valued probability vector is generated that specifies the likelihood of generating a one in each index of the bit vector to which the parameter space is mapped. Potential solution vectors, otherwise

known as *chromosomes*, are found by stochastically sampling the probability vector. At the initialisation of the algorithm all indices of the probability vector are set to equal likelihood (0.5), and so the focus of PBIL is to iteratively alter the probability vector until it yields good responses with high probability.

A *population* of solution vectors are maintained and ranked according to their fitness. The probability vector is then altered towards the best solutions and away from the worst solutions, representing positive and negative learning rates respectively. To promote diversity and prevent the premature convergence of the probability vector towards local optima, *mutation* is implemented by randomly selecting indices of the probability vector and adjusting their values towards 0.5. The algorithm terminates either when better solutions have not been found after a set number of iterations (convergence), or when the maximum number of iterations/function evaluations has elapsed.

5.2 Space mapping

Space mapping (SM) is an optimisation methodology that belongs to the class of surrogate-based optimisation (SBO) [1]. The methodology has been consistently developed since its formulation in 1994, and is well-established in the field of RF and microwave simulation and design.

The following subsection details the mechanics of SM, based on the work in [42], and provides a discussion of the various types of SM that are considered and implemented in this thesis.

5.2.1 Space mapping Algorithm

The core concept of space mapping is to replace the optimisation of a fine, physically accurate model with that of a faster *surrogate model* (or simply a *surrogate*). The surrogate model is created by modifying a *coarse model* (a simpler, but less accurate version of the fine model) by linearly mapping its inputs, its implicit parameters or its outputs to those of the fine model, thereby creating an approximation of the fine model with significantly reduced computational cost.

A solution is sought for:

$$\boldsymbol{x_{f.opt}} = \arg\min_{\boldsymbol{x}\in X_f} U(\boldsymbol{R_f}(\boldsymbol{x})) \qquad (5.1)$$

Where $\boldsymbol{R_f}: X_f \rightarrow R^m$, $\boldsymbol{x} \subseteq X_f$ denotes the fine response, and U is a given objective/cost function [42]. The parameter space X_f is real, n-dimensional and constrained by upper and lower bounds; that is to say, $X_f \subseteq R^{\boldsymbol{n}}$. While this problem could be solved by direct optimisation, it is assumed that it is a computationally expensive process and that similar, comparatively faster results can be obtained by using some surrogate model.

Through the linear mapping of parameters and/or responses (outputs), the coarse and fine models are *aligned* in order to make the coarse response fit the fine response; that is to say, alignment minimises the difference between the coarse and fine responses *at a specific point in the parameter space*. It is not likely, nor expected that this alignment will apply across the entire parameter space; realistically, even a good surrogate will only be well-aligned in some local subspace about the point X_s where the surrogate was built. A *good surrogate* is considered to be one that produces an acceptably small error between its response and that of the fine model for an acceptably large parametric subspace about X_s. The exact definitions of 'acceptably small' and 'acceptably large' depend on the design problem, and a practical definition of either is *large/small enough for the optimiser to converge on a solution that meets the design specification*.

The limitation of alignment is overcome by iteratively building surrogates and optimizing them, using their optimal parameters as starting positions for the next surrogate to be built. The intent of SM is that this iterative process will converge to a well-aligned surrogate with a set of parameters that produce an optimal (or at least acceptable) fine response. It is important to ensure that the coarse model resembles the fine model enough to have a similar response, yet simple enough to be computationally cheap.

A sequence of points $\boldsymbol{x}^{(i)}$ is generated in the parameter space X_f, and a family of surrogate models $\boldsymbol{R_s}^{(i)}: X_s{}^{(i)} \rightarrow R_m$, $i = 0,1,2 \ldots$ such that:

$$\boldsymbol{x}^{(i+1)} = \arg \min_{\boldsymbol{x_f} \in X_f \cap X_s{}^{(i)}} U(\boldsymbol{R_s}^{(i)}(\boldsymbol{x})) \qquad (5.2)$$

So, beginning with a fine and coarse model, and an initial set of input parameters $\boldsymbol{x}^{(0)}$, *parameter extraction* is performed in order to find the first surrogate $\boldsymbol{R_s}^{(1)}$, which is then optimized to find the first set of 'optimal' parameters $\boldsymbol{x}^{(1)}$. Then the fine model is evaluated at $\boldsymbol{x}^{(1)}$, and if it satisfies the termination condition of the cost function U, the process is complete. The termination condition is defined as in [42], and thus is met if $\left| \boldsymbol{x}^{(i+1)} - \boldsymbol{x}^{(i)} \right| < \delta$, where δ is a small constant. If it is not met, $\boldsymbol{x}^{(1)}$ is used as an initial point to build $\boldsymbol{R_s}^{(2)}$, which is then optimized, and so on. Each response at the i^{th} iteration takes the form of a $m \times 1$ vector; if $m > 1$, the response is typically sampled in frequency (e.g. $|S_{11}|$ as a function of frequency). The process is summarised in the flowchart of Figure 5.2.

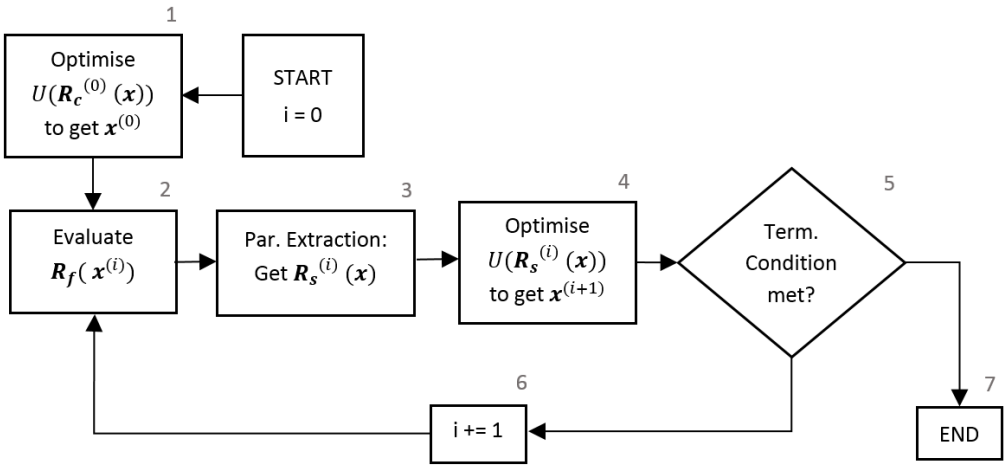

Figure 5.2- General SM Flowchart

$\boldsymbol{R_s}^{(i)}$ is defined in its most general form as:

$$\boldsymbol{R_s}^{(i)}(\boldsymbol{x}) = \boldsymbol{A^{(i)}} \cdot \boldsymbol{R_c}\left(\boldsymbol{B^{(i)}} \cdot \boldsymbol{x} + \boldsymbol{c^{(i)}}, \boldsymbol{x_p}^{(i)}\right) + \boldsymbol{d^{(i)}} \quad (5.3)$$

Where $\boldsymbol{R_c}$ denotes the coarse response. This definition of $\boldsymbol{R_s}^{(i)}$ here differs from [42] in the sense that it omits the $\boldsymbol{G^{(i)}}$ and $\boldsymbol{E^{(i)}}$ terms; these are not included because they belong to two SM techniques (namely, input-dependent implicit SM and Jacobian-matching SM) that are not considered in the scope of this thesis.

The various terms of Equation (5.3) require some further definition. $\boldsymbol{A^{(i)}}$ is a $m \times m$ diagonal matrix containing multiplicative output factors $\left\{a_1^{(i)} \dots a_m^{(i)}\right\}$, $\boldsymbol{B^{(i)}}$ is a $n \times n$ matrix containing multiplicative input factors, $\boldsymbol{c^{(i)}}$ is a $n \times 1$ vector containing additive input values $\left\{c_1^{(i)} \dots c_n^{(i)}\right\}$, $\boldsymbol{d^{(i)}}$ is a $m \times 1$ vector containing additive output values $\left\{d_1^{(i)} \dots d_n^{(i)}\right\}$ and $\boldsymbol{x_p}^{(i)}$ is a $q \times 1$ vector containing additive implicit values $\left\{x_{p1}^{(i)} \dots x_{pq}^{(i)}\right\}$. Each of these terms is linked with a specific SM technique, as is discussed in the following section.

5.2.2 SM Techniques

SM can be applied to a design through several distinct techniques, either singularly or as a combination of techniques [42]. As indicated in the previous section, each of the lettered terms in Equation (5.3) is associated with one of these techniques.

The following methods are considered in the scope this thesis:

- **Input SM:** Maps the direct input parameters of the coarse model to the fine model with the multiplicative factors $\boldsymbol{B}^{(i)}$ and/or the additive offsets $\boldsymbol{c}^{(i)}$. The coarse model must be iteratively re-evaluated throughout the parameter extraction process.
- **Implicit SM:** Maps implicit model parameters (that is, parameters that are not dimensions of the parameter space) with the additive implicit offsets $\boldsymbol{x_p}^{(i)}$. Like Input SM, the coarse model must be iteratively re-evaluated throughout the parameter extraction process.
- **Output SM (OSM):** Maps the response/output of the coarse model to the fine model with the multiplicative factors $\boldsymbol{A}^{(i)}$ and/or the additive offsets $\boldsymbol{d}^{(i)}$. The values of $\boldsymbol{A}^{(i)}$ and $\boldsymbol{d}^{(i)}$ may be set to a single value applied to the whole response, or individually calculated for all m response points. During parameter extraction, $\boldsymbol{A}^{(i)}$ is determined iteratively but without requiring an iterative re-evaluation of the coarse model; $\boldsymbol{d}^{(i)}$, however, is determined at the end of the parameter extraction process.
- **Frequency SM (FSM):** Maps a coherent set of coarse response points (typically a frequency response, hence the name) to its corresponding fine response points using an affine transformation vector $\boldsymbol{F} = \left[{f_0}^{(i)}\ {f_1}^{(i)}\right]$. If the response is calculated across an axis ω, the transformation is applied such that $\omega \rightarrow {f_0}^{(i)} + {f_1}^{(i)}\omega$. This method is useful if it can be predicted that the major error between the fine and coarse model is some constant frequency offset. FSM does not require an iterative re-evaluation of the coarse model throughout parameter extraction.

Table 5.1 - SM Techniques Summary

SM Technique	Term	Mapping Operation	No. of Coarse Re-evaluations in Parameter Extraction
Output	$\boldsymbol{A}, \boldsymbol{d}$	Response (output)	1
Input	$\boldsymbol{B}, \boldsymbol{c}$	Input parameters	$\gg 1$ (Iterative evaluation)
Implicit	$\boldsymbol{x_p}$	Implicit parameters	$\gg 1$ (Iterative evaluation)
Frequency	$\boldsymbol{F}$	Affine Response Transformation	1

Figure 5.2 summarises the listed SM techniques and their features, as well as their corresponding mapping terms in Equation (5.3). The use of Input and/or Implicit SM is disadvantaged by its need for

iterative coarse model re-evaluation during the parameter extraction process, but this potential problem is reduced or effectively negated if the coarse model is fast enough.

For any of the SM techniques listed above, parameter extraction involves directly optimising the values of the mapping term(s) such that $\boldsymbol{R_s}^{(i)}\left(\boldsymbol{x}^{(i)}\right)$ resembles $\boldsymbol{R_f}\left(\boldsymbol{x}^{(i)}\right)$ as closely as possible. The optimisation of the mapping terms can be handled by either local or global optimisation schemes.

The merit of any of the listed SM techniques is dependent on the nature of the design problem at hand. Ideally, a technique is selected that can produce a good surrogate (as defined earlier in this chapter). However, this would require that the nature of the error between the fine and coarse model is known, which is not always possible. Input and Implicit SM possibly benefit from the fact that they directly affect parameters that may control the underlying behaviour of the structure under consideration, and may be able to affect the response in a more refined manner than OSM or FSM. This is only possible for a well-parameterised structure with a sufficient control of the response through the input parameters; the aperture-coupled patch antenna is a good example of such a structure, having its impedance behaviour well-controlled through the physical parameters considered in [16].

5.3 Basic Patch Antenna SM

The first application of SM to the overall design procedure is to optimise the patch antenna element. The basic patch is considered first, as it is the simplest structure with the fewest degrees of freedom. The physical dimensions of the patch are to be used as input variables. Both the full-wave EM model and Jaisson's TLM will be used as coarse models, for the purpose of comparing their effectiveness. The full-wave models are implemented in FEKO.

In this section, the defining components of the basic patch's SM process are discussed. The output, inputs and choice of SM technique are considered, and an explanatory example is provided.

5.3.1 Response and Cost Function

The response function for the basic patch antenna must optimise the patch's impedance characteristics, and is chosen to be of the same form as is used in Chapter 3 and Chapter 4:

$$R(\boldsymbol{x}, f_k) \equiv |S_{11}|(f_k) \qquad k \in 1,2 \ldots m \tag{5.4}$$

Where f_k is the discrete set of m frequency points at which the response is sampled:

$$f_k \equiv \left[f_0 - \frac{BW_{max}}{2}\right] + \frac{BW_{max} \cdot (k-1)}{m} \tag{5.5}$$

The exact value of m depends on the size of the band and desired frequency resolution, and is therefore specific to each individual design. The response is measured across a frequency band BW_{max} about the design's desired centre-frequency f_0.

A cost function must be designed to use in the optimisation of the surrogate model (block 5 in Figure 5.2). Since the design procedure is intended for both narrowband and wideband systems, the cost function must quantify both bandwidth BW and deviation of the passband Δf from the desired centre-frequency. If only bandwidth is measured about a fixed target centre-frequency, then designs approaching the optimum may be missed simply because they are de-tuned from the desired centre-frequency.

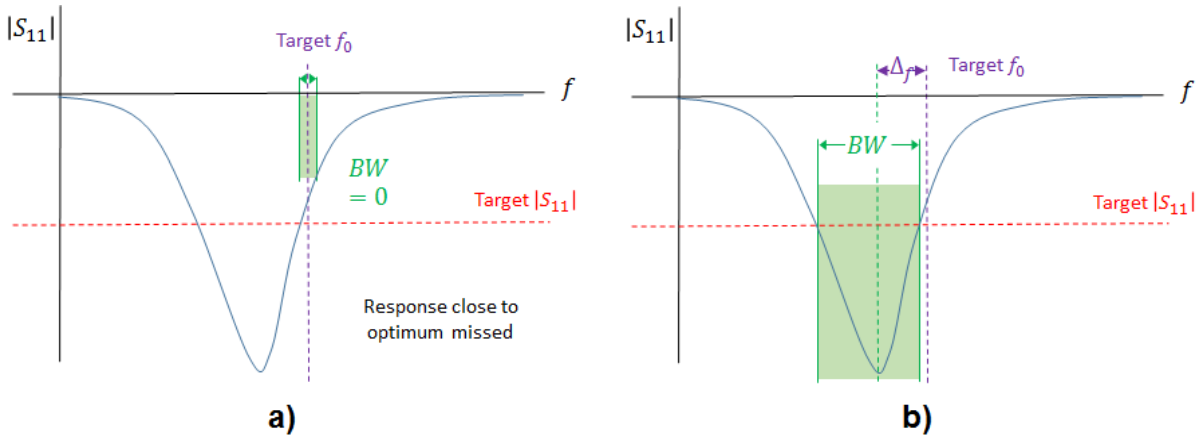

Figure 5.3 - $|S_{11}(f)|$ Cost schemes applied to a close-to-optimum response: a) BW only, b) BW and Δ_f

Figure 5.3 illustrates the difference between the two cost schemes described above. The cost function including bandwidth and frequency deviation is formulated as:

$$c_0 \equiv w_{BW} \left| \frac{BW - BW_{max}}{BW_{max}} \right| + w_{\Delta f} \left| \frac{\Delta f - \Delta f_{max}}{\Delta f_{max}} \right| \qquad (5.6)$$

Where Δf_{max} is the maximum measurable frequency deviation $\left(\frac{BW_{max}}{2}\right)$, w_{BW} is the bandwidth weighting factor and $w_{\Delta f}$ is the frequency deviation weighting factor. The weighting factors are included so that the designer may choose to prioritise one goal over another; for example, a narrowband design with a strict centre-frequency specification can be accommodated by weighting the cost function so that the bandwidth term becomes small or negligible.

The merit terms of the cost function must still be defined. The deviation Δf from f_0 is determined as the distance between f_0 and the actual centre-frequency of the response:

$$\Delta f \equiv | f_0 - f_c | \qquad (5.7)$$

The response's actual centre-frequency is defined as the minimum value of the response across frequency:

$$f_c \equiv \min_{f_k} \{R_s(\boldsymbol{x}, f_k)\} \quad (5.8)$$

This definition of f_c assumes that the impedance response takes the form of a single distinct resonance, which is a good assumption for a basic patch antenna.

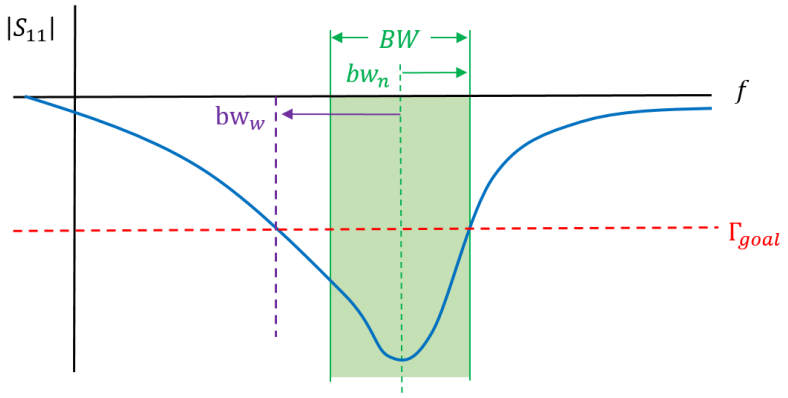

Figure 5.4 – Cost function calculation of BW

The bandwidth BW is determined as the largest *symmetrical* band about f_c that is equal to or lower than the desired goal value Γ_{goal}. Figure 5.4 illustrates the calculation of BW for an asymmetric response passband about f_c. The passband is split into two sub-bands about f_c: a wide sub-band bw_w and a narrow sub-band bw_n. The bandwidth BW is thus determined by bw_n:

$$BW \equiv 2 \cdot bw_n \quad (5.9)$$

An alternate way to calculate BW would be to set it to the full size of the entire passband, and to define f_c as the frequency at its centre. However, the above method is preferred because its definition of f_c is more consistent and is able to condition symmetry of $|S_{11}|$ about f_c.

5.3.2 Model Parameters

5.3.2.1 Input Parameters

Although several physical parameters affect the impedance response of the basic patch, not all of them can realistically be used as inputs to the optimisation process. It is impractical to set the substrate parameters as input variables, because commercially available substrates are produced in a limited number of thicknesses and an even more limited number of permittivities.

The dimensions L_0, W_0 and x_0 are the only parameters that can be considered viable inputs, and their combined ability to influence the patch's impedance response is strong. It should be noted that the upper and lower limits of the two parameters are not equal, since small changes in L_0 can significantly affect the patch's resonant frequency. W_0 requires a comparatively larger parametric space to vary through, as its effect on the patch's impedance locus on the Smith Chart requires much larger changes in the parameter to have a significant effect.

5.3.2.2 Implicit Parameters

In the selection of a good set of implicit parameters for Implicit SM, it should be anticipated what effect those parameters have on the underlying behaviour of the design problem at hand. Implicit parameters are often selected because their influence on the design is known, yet they cannot be made direct input parameters due to design constraints (e.g. substrate properties, when a design is limited to a specific type of manufactured substrate).

In the case of the basic patch antenna, the substrate parameters h_0 and ε_{rp} stand out as good candidates for Implicit SM. As discussed in Chapter 2, these two parameters affect the resonant frequency, matching and bandwidth of the basic patch's impedance response, and the extent to which they do so can be predicted analytically.

5.3.3 Choice of SM Technique

The final choice of SM technique for the basic patch design is largely dependent on the choice of coarse model. The most appropriate technique, as discussed throughout this chapter, would be one that most effectively minimises the error between the fine and coarse models over the largest possible subspace within the parameter space. The correct choice requires insight into the limitations of the coarse models available, combined with the strategic application of a method that can circumvent those limitations.

5.3.3.1 Full-wave Coarse Model

A distinct advantage of using a full-wave coarse model is that its solution method is the same as the fine model, and therefore its underlying behaviour will be similar (provided that the structure is not so coarsely meshed that it becomes unrecognisable from the fine model). Errors between the models are consequently due to meshing inaccuracies that can be predicted- in the case of the patch, the coarser mesh leads to L_0 and W_0 appearing shorter than they actually are, resulting in a raised resonant frequency and a broader impedance locus.

With the above in mind, Input SM presents itself as a good choice. The fact that the coarse model's response error can be directly linked to the input parameters makes Input SM a natural solution to the problem, although the parameter extraction process would be expensive for many re-evaluations of a full-wave coarse model. Implicit SM using the permittivity ε_{rp} and height h_0 of the patch substrate could also work well, given the parameters' influence on the patch's input impedance and resonant frequency.

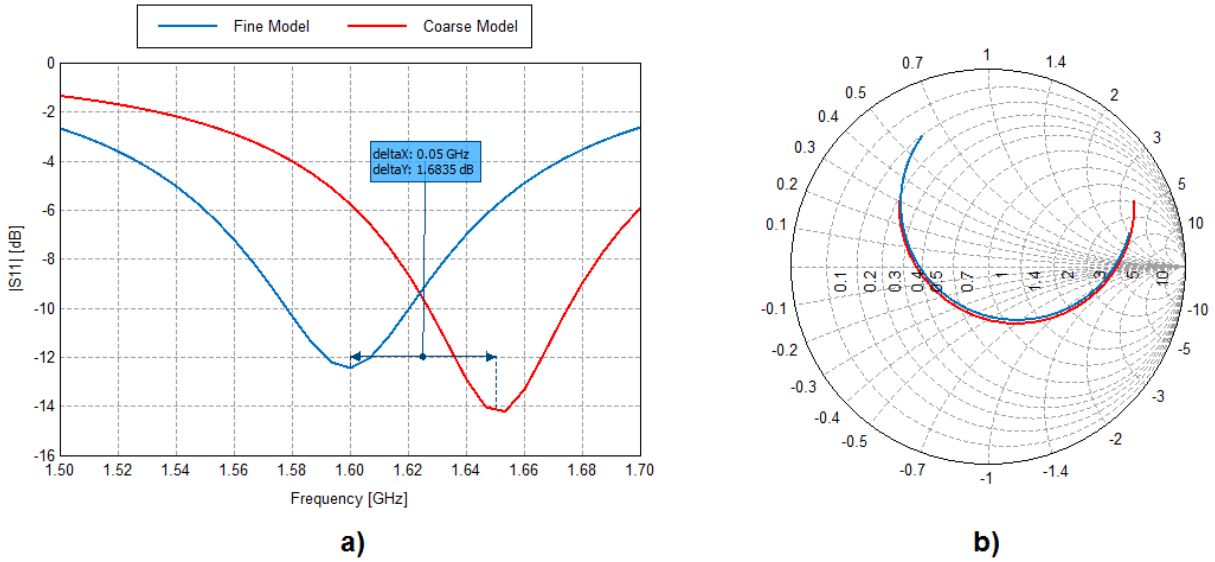

Figure 5.5 - Fine vs. Coarse model of 1.6 GHz patch: a) |S11|, b) Smith Chart

Figure 5.5 shows the fine and coarse responses of an example 1.6 GHz basic patch design with the following specifications: $L_0 = 44$ mm, $W_0 = 58$ mm, $x_0 = 0$ mm, $h_0 = 6$ mm, $\varepsilon_{rp} = 4.1$. The computational cost of the full-wave fine and coarse models are summarised in Table 5.2. The coarse model is meshed as coarsely as possible while still preserving the general response features of the fine model. It can be seen that the coarse response does not differ much from the fine response, even for such a significant reduction in mesh cells and solver time.

Table 5.2- Fine vs. Coarse model of 1.6 GHz basic patch: Computational cost summary

Model	No. of Mesh Cells	Solver Time [s]
Fine	606	107.4
Coarse (full-wave)	22	4.1

Although the above results point to Input SM being the best choice for the basic patch's full-wave coarse model, the solver time remains a problem. The parameter extraction process could require many evaluations of the coarse model, which would result in significant computational expense for a solver time of 4.1s per coarse evaluation.

The coarse response of Figure 5.5a mostly differs from the fine response in resonant frequency; in fact, the coarse response is roughly a frequency-scaled version of the fine response. Thus, FSM is also worth considering for the full-wave coarse model. FSM is a more abstracted technique than Input SM, but it is effective if it can be predicted that the coarse model has some constant frequency offset from the fine model. In the case of the basic patch, L_0 exclusively controls the resonant frequency, and a consistent

ratio of fine-to-coarse mesh size would lead to a constant frequency offset between the fine and coarse response.

In the design example further in this section, the performance of Input SM, Implicit SM and FSM are tested with the TLM coarse model and compared.

5.3.3.2 TLM Coarse Model

In Chapter 4, it was shown that Jaisson's TLM is a fast and accurate solution for the impedance response of a basic patch. With a solver time of 0.369s, the iterative process of Input or Implicit SM's parameter extraction would likely require very little computational cost, even if a global optimisation procedure is used.

Without the burden of computational expense, Input SM appears to be a good option for the TLM coarse model. In the SM design example that follows, Input SM with the TLM coarse model is applied to the design problem.

5.3.4 Basic Patch SM Example

In this section, a set of SM processes are applied to the design of a basic patch antenna. The antenna is designed to resonate at 2.4 GHz, and is built on a substrate with $h_0 = 9\ mm$, $\varepsilon_{rp} = 3.5$. The following SM processes are performed on the design example:

- Input SM (full-wave coarse model)
- Input SM (TLM coarse model)
- Implicit SM (TLM coarse model)
- FSM (TLM coarse model)

The SM process is limited to 3 full SM iterations, with only the fine model being evaluated in Iteration 4. The aim of the optimisation is to attain $|S_{11}| \leq -10$ dB at $f_0 = 2.4$ GHz. The starting value for the input parameters are $L_0 = 32.2$ mm, $W_0 = 30.3$ mm $(0.8 \cdot L_0)$, $x_0 = 9.7$ mm $(0.25 \cdot L_0)$. The response is sampled at $m = 31$ points between 2.1 GHz and 2.7 GHz, for both the fine and coarse models. In the case of Implicit SM, the substrate parameters All local optimisations are controlled by the Nelder-Mead Simplex algorithm, and global optimisations are controlled by the PBIL algorithm. The PBIL process is set to a 7-bit initial chromosome, a population size of 100 and a maximum number of 1000 coarse model evaluations. The limit of 1000 coarse model evaluations is perhaps restrictive for PBIL, but as will be shown in the results, it is sufficient for the design at hand. Global optimisation is set to be used on the coarse/surrogate optimisation of the first SM iteration, and local optimisation thereafter. The parameter extraction step is set to use local optimisation throughout the SM process.

The full-wave coarse model, implemented in FEKO, is meshed with an edge refinement factor of $F_{mesh} = \frac{\lambda_0}{25}$ and has a solver time of 5.08s when simulated with the starting input parameters. The fine model is meshed with is meshed with an edge refinement factor of $F_{mesh} = \frac{\lambda_0}{100}$ and has a solver time of 140.1s when simulated with the starting input parameters.

The main aim of this example is to compare the performance of the TLM as a coarse model for the three listed SM techniques. The process using the full-wave coarse model serves as a reference for the time required to complete a 'conventional' patch SM process.

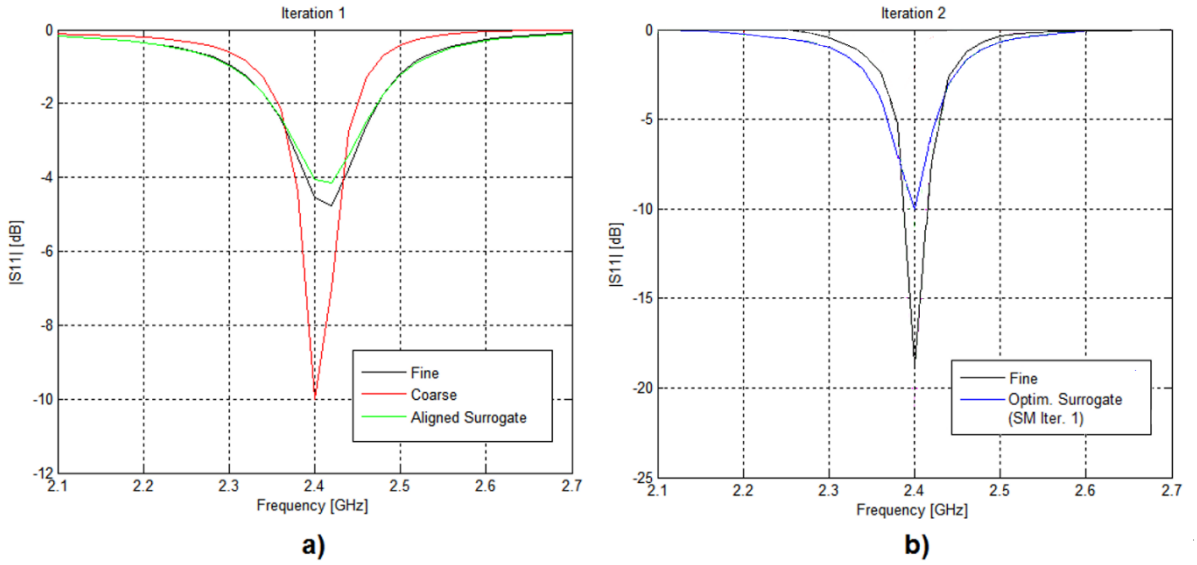

Figure 5.6 - Basic patch antenna Input SM example- Full-wave coarse model results

Figure 5.6 shows the results of the full-wave coarse model's Input SM process. The coarse model optimisation step (block 2 of Figure 5.2) has clearly optimised the initial coarse model to the correct resonant frequency and $|S_{11}|$ magnitude in Figure 5.6a. While the fine response is not perfectly aligned to the coarse response in Iteration 1, the aligned surrogate fits the fine response fairly closely.

It can be seen in Figure 5.6b that Iteration 1's optimised surrogate response (blue curve) has been tuned to the correct frequency and set to $|S_{11}| = -10$ dB at resonance (2.4 GHz). The fine response of Iteration 2 is also tuned to 2.4 GHz with $|S_{11}| = -19.2$ dB at resonance, and therefore the design specification has been satisfied by Iteration 2, through a suitable alignment of the fine and optimised surrogate responses. The total solver time for the entire SM process is 30326s.

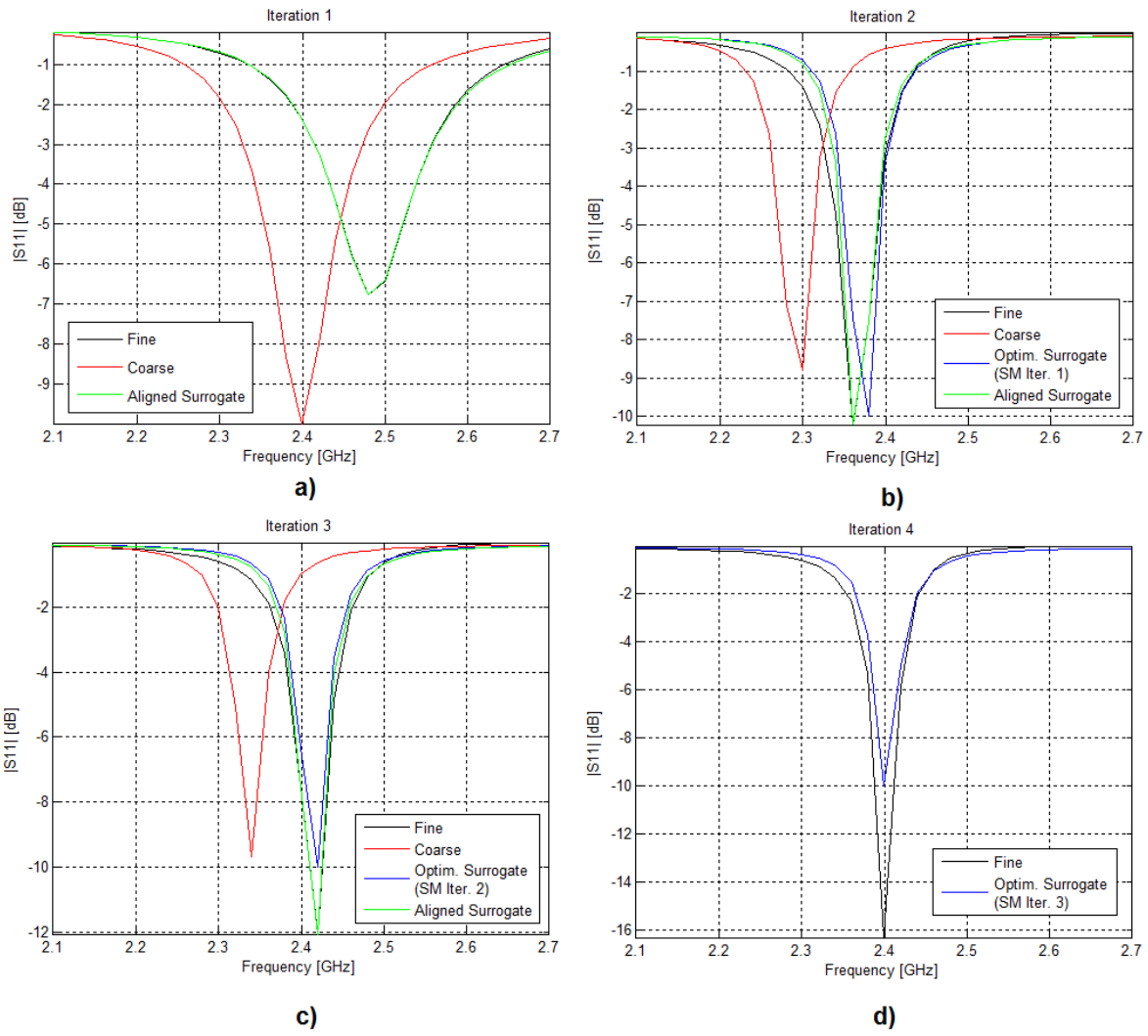

Figure 5.7 - Basic patch antenna Input SM example- TLM coarse model results

Figure 5.7 shows the results of the TLM coarse model's Input SM process. The coarse model optimisation step (block 2 of Figure 5.2) has clearly optimised the initial coarse model to the correct resonant frequency and $|S_{11}|$ magnitude in Figure 5.7a. While the fine response is not perfectly aligned to the coarse response in Iteration 1, the aligned surrogate almost perfectly fits the fine response.

This trend continues throughout the three SM iterations until the final fine response is correctly tuned to 2.4 GHz with $|S_{11}| = -16$ dB at resonance. The set of inputs for the final response are $L_0 = 34.3$ mm, $W_0 = 20.1$ mm, $x_0 = 15.3$ mm. The total solver time for the entire SM process is 927.4s.

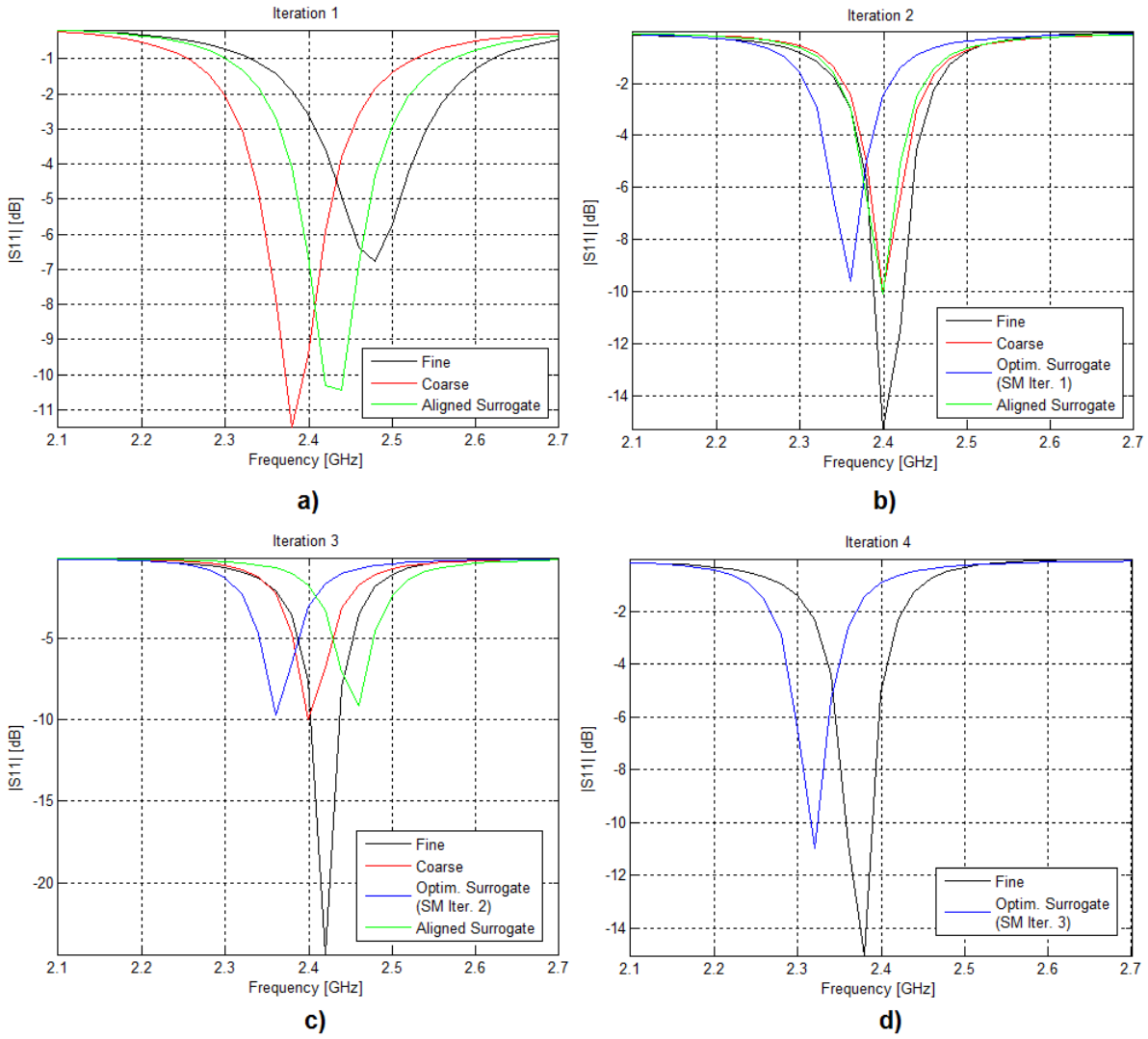

Figure 5.8- Basic patch antenna Implicit SM example- TLM coarse model results

Figure 5.8 shows the results of the TLM coarse model's Implicit SM process. The coarse model optimisation step (block 2 of Figure 5.2) has optimised the initial coarse model close to the correct resonant frequency and $|S_{11}|$ magnitude in Figure 5.8a. The surrogate is not aligned as well to the fine model as in the Input SM process of Figure 5.6, but after surrogate optimisation it does appear to produce a desirable fine response in Iteration 2 (Figure 5.8b). It is important to note that the optimised surrogate of Iteration 1 (the blue plot of Figure 5.8b) is also misaligned with the fine response of Iteration 2, whereas the Input SM process's alignment between the fine and surrogate models is more consistent.

The trend established in Iteration 1 continues throughout the three SM iterations. The final fine response is tuned to just below 2.4 GHz with $|S_{11}| = -15$ dB at resonance. The inaccuracy in the resonant frequency may seem small, but for this type of narrowband design it is enough to miss the desired

passband. The set of inputs for the final response are $L_0 = 32.9$ mm, $W_0 = 17.9$ mm, $x_0 = 14.5$ mm. The total solver time for the entire SM process is 1098.3s.

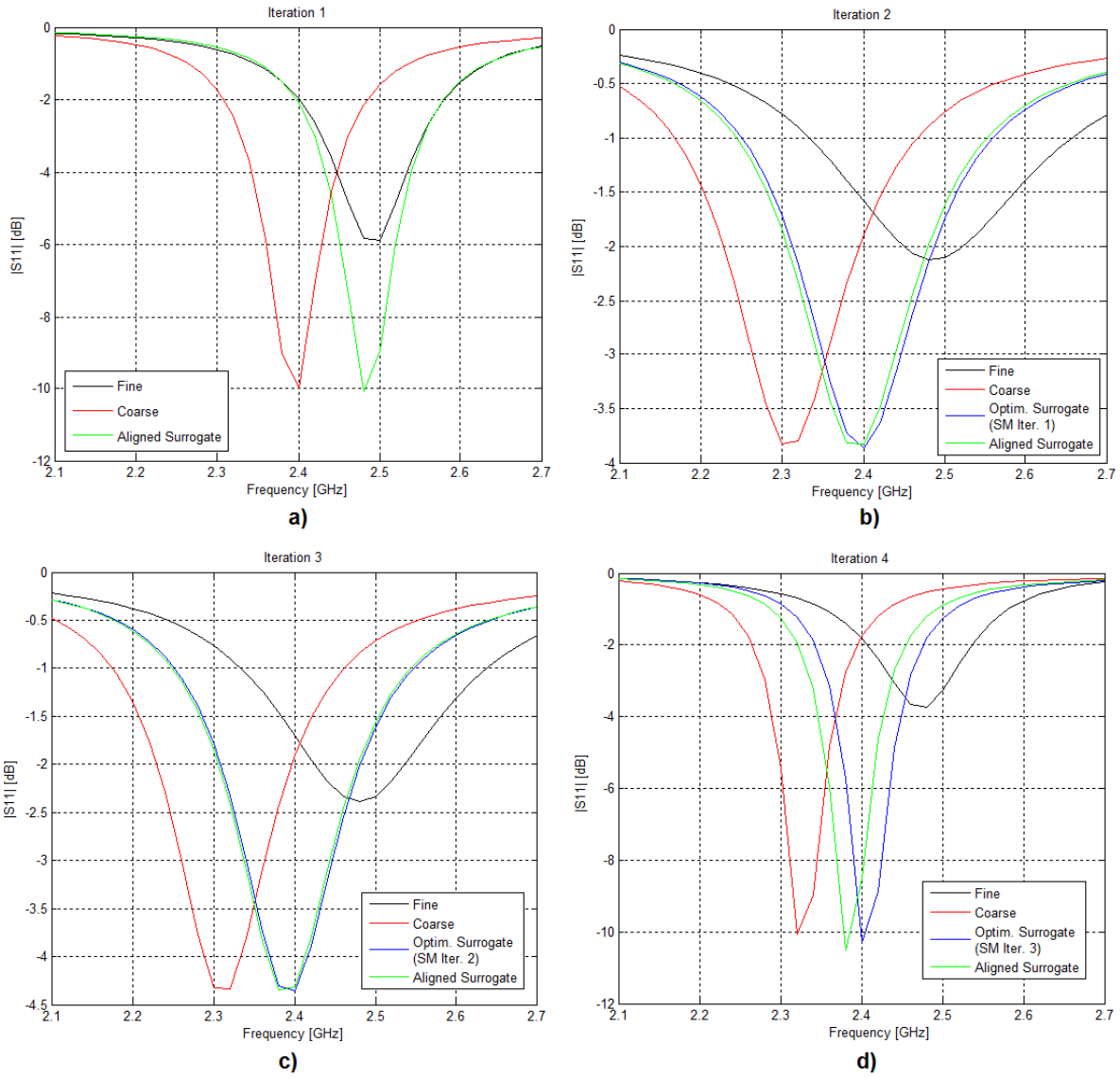

Figure 5.9- Basic patch antenna FSM example- TLM coarse model results

Figure 5.9 shows the results of the TLM coarse model's FSM process. The coarse model optimisation step (block 2 of Figure 5.2) has clearly optimised the initial coarse model to the correct resonant frequency and $|S_{11}|$ magnitude in Figure 5.9a. The surrogate is as well-aligned in Iteration 1 as FSM is capable of, matching its resonant frequency to the fine response. However, the process clearly begins to break down from Iteration 2 onwards. Besides the fact that the optimised surrogate of Iteration 1 (the blue plot of Figure 5.9b) does not meet the -10 dB magnitude goal at resonance, the surrogate fails to align itself in frequency to the fine response in Iteration 2.

This trend continues until the final fine response is tuned towards 2.5 GHz with $|S_{11}| = -3.7$ dB at resonance. The set of inputs for the final response are $L_0 = 31.5$ mm, $W_0 = 32.1$ mm, $x_0 = 9.1$ mm. The total solver time for the entire SM process is 678.8s.

Table 5.3- Basic patch SM example summary

SM type (Coarse model)	Total solver time [s]	Frequency error [GHz / %]	Magnitude error [dB]
Input (Full-wave)	30326	0	0
Input (TLM)	927.4	0	0
Implicit (TLM)	1098.3	0.025 / 1.04%	0
FSM (TLM)	678.8	0.075 / 3.13%	6.3

Table 5.5 summarises the results of the example SM processes. Of the SM techniques considered for the TLM, Input SM produces the best results overall. While Implicit SM's results are partially effective, its inability to align the surrogate response as well as Input SM makes it a less attractive choice, as well as its slightly higher solver time. FSM is shown to be faster than the other techniques for this example, as is expected since its parameter extraction process is almost instantaneous relative to Input or Implicit SM. However, its lack of accuracy is too great for it to be seriously considered as a good fit for the basic patch SM process.

In comparison to the full-wave Input SM process, the TLM input SM process is more than 30 times faster and with similar performance. This, combined with the accuracy and stability of the process, make it the primary choice for the optimisation of basic patch elements in Chapter 7.

5.4 Aperture-fed Patch Antenna SM

The SM procedure for the aperture-fed patch antenna shares many of the same properties as the basic patch's SM procedure, since both processes occupy the same stage of the overall design process of the antenna array. Its more complex structure, however, provides a number of extra degrees of freedom that change the applicability of the SM techniques under consideration.

The goals and cost function for the aperture-fed patch are the same as those defined in Section 5.3. The input parameters and choice of SM technique are handled differently from the basic patch, however, and are the subject of this section.

5.4.1 Model Parameters

The structure of the aperture-fed antenna introduce a number of extra degrees of freedom that must be considered in the construction of an appropriate SM process. This section considers the potential inputs and implicit parameters that are available for the model.

5.4.1.1 Input Parameters

The aperture-fed patch shares the L_0 and W_0 parameters with the basic patch, although their influence on the response changes somewhat. L_0 still controls the resonant frequency, but does so alongside the aperture length L_{ap}. W_0 controls the size of the impedance locus on the Smith Chart, but distinctly less so than L_{ap}. The tuning stub length L_{tune} is undoubtedly a good choice to include as an input parameter, having the ability to tune the input reactance of the antenna in a predictable and finely adjustable manner.

The influence of L_{ap} on the impedance response is so pronounced that it is difficult to determine whether or not it is a good input parameter. L_{ap} strongly affects both the resonant frequency and the overall feed-to-patch coupling, which manifests as a powerful tightening/broadening of the impedance locus on the Smith Chart. Allowing L_{ap} to vary too wildly could cause the response to converge on an undesired local optimum, in the form of the desired resonance but with poor feed-to-patch coupling. Setting L_{ap} to a static value, however, may deny the optimisation an extra mechanism for fine-tuning the coupling or the resonant frequency in small increments. For this reason, it is decided that L_{ap} is included as an input parameter but limited to a relatively tight set of bounds around its starting value. The starting value should be experimentally pre-determined to provide good initial feed-to-patch coupling.

It is important that the set of input parameters is not made too large, for the sake of computational cost. For n input parameters, an n-dimensional parameter space must be traversed during the parameter extraction and optimisation process. Therefore, it is desirable to select the smallest set of inputs that still allow the designer to exercise the necessary control of the response features. In light of this, the input set $[\![L_0 \;\; L_{tune} \;\; L_{ap}]\!]$ is chosen. The exclusion of W_0 allows it to be set to a fixed value smaller than L_0 to ensure the TM^z_{100} patch mode, and its influence of the response is similar to L_{ap}.

5.4.1.2 Implicit Parameters

If a full-wave coarse model is used here, there are not many options available to include useful implicit parameters. The feed and patch substrates' heights or permittivities could be used, but it has already been shown in Section 6.3 that the patch substrate is not a particularly effective source of implicit parameters. The variation of the feed substrates' properties might be able to adjust for the feed-to-aperture coupling, but would also significantly affect the impedance characteristics of the feed-line.

If the TLM is used as a coarse model, several opportunities are provided to use Implicit SM. The aperture admittance Y_s and the turns ratios n_f and n_p are approximate values that are not direct physical parameters of the structure, and their adjustment could be an effective way to increase the TLM's accuracy. Specifically, in designs where the patch substrate is made too thick or its permittivity is too low, the TLM's fidelity is shown to degrade, and an adjustment of the aforementioned three values could help to repair the degradation.

It must also be considered whether the patch substrate's influence on the TLM's accuracy is likely to change as the inputs are varied across the parameter space. If not, then it may be sufficient to pre-adjust the aperture admittance and/or the coupling transformers' turns ratios before commencing the SM process.

5.4.2 Choice of SM Technique

The observations made for the basic patch's full-wave and coarse models also apply to those of the aperture-fed patch. The only notable exception is that the aperture-fed patch's full-wave coarse model is even more computationally expensive.

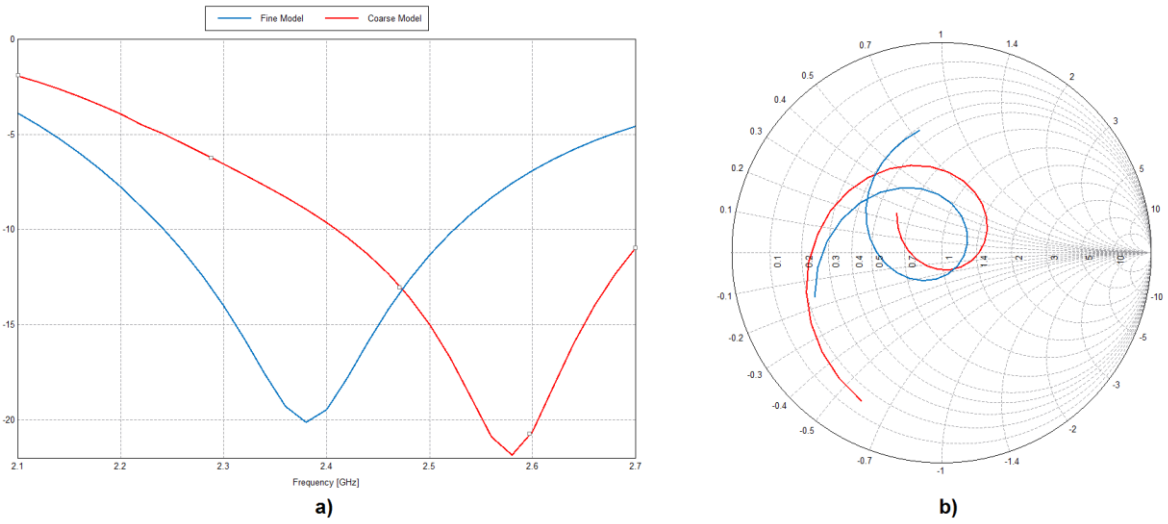

Figure 5.10 – FEKO Fine vs. Coarse model of 2.4 GHz aperture-fed patch: a) |S11| , b) Smith Chart

Figure 5.2 shows the FEKO-simulated fine and coarse responses of an example 2.4 GHz aperture-fed patch design with the following specifications: $L_0 = 26.1$ mm, $W_0 = 22.8$ mm, $L_{ap} = 23.4$ mm, $L_{tune} = 9$ mm, $w_f = 1.1$ mm, $h_0 = 9$ mm, $h_f = 0.5$ mm, $\varepsilon_{rp} = 3.5$, $\varepsilon_{rf} = 3.5$. The computational cost of the full-wave fine and coarse models are summarised in Table 5.4. The coarse model is meshed as coarsely as possible while still preserving the general response features of the fine model. It can be seen that the coarse response does not differ much from the fine response, even for such a significant reduction in mesh cells and solver time. The greatest difference between the responses is their shift in resonant frequency.

Table 5.4 - Fine vs. Coarse model of 2.4 GHz aperture-fed patch: Computational cost summary

Model	No. of Mesh Cells	Solver Time [s]
Fine	912	224.1
Coarse (full-wave)	32	59.3

The computational cost of the 2.4 GHz aperture-fed patch's full-wave fine and coarse models are summarised in Table 5.4. Despite the great difference in the two models' number of mesh cells, the coarse response is only 3.77 times faster than the fine response. It is assured that a full SM process, even one restricted to local optimisation techniques, would be prohibitively slow with models such as those shown above. Hence, the SM example of the next subsection will only consider the TLM as a coarse model.

The results of the basic-patch SM example have already indicated that FSM is not as well-suited to the optimisation of a patch antenna structure with a TLM coarse model as Input SM or Implicit SM. The inclusion of an aperture feeding structure would only exacerbate this, because of the additional resonating element introduced by the aperture itself. For this reason, the SM example of the next subsection only considers Input and Implicit SM.

5.4.3 Aperture-fed Patch SM Example

In this section, a set of SM processes are applied to the design of an aperture-coupled patch antenna. The antenna is designed to resonate at 2.4 GHz, and is built on a substrate combination with $h_0 = 9$ mm, $h_f = 0.5$ mm, $\varepsilon_{rp} = 3.5$, $\varepsilon_{rf} = 3.5$, $W_{ap} = 1$ mm, $w_f = 1.1$ mm. Input SM, using a TLM coarse model, is performed on the design example.

The aim of the optimisation is to attain $|S_{11}| \leq -10$ dB at $f_0 = 2.4$ GHz, with 10% FBW. The starting value for the input parameters are $L_0 = 28.5$ mm, $L_{ap} = 20$ mm, $L_{tune} = 18.9$ mm, and the patch width is set to $W_0 = 22.8$ mm $(0.8 \cdot L_0)$. The response is sampled at $m = 31$ points between 2.1 GHz and 2.7 GHz, for both the fine and coarse models. All local optimisations are controlled by the Nelder-Mead Simplex algorithm, and global optimisations are controlled by the PBIL algorithm. The PBIL process is set to a 7-bit initial chromosome, a population size of 100 and a maximum number of 1000 coarse model evaluations. Global optimisation is set to be used on the coarse/surrogate optimisation of the first SM iteration, and local optimisation thereafter. The parameter extraction step is set to use local optimisation throughout the SM process.

It should be noted that, in this example, the coarse model optimisation step (block 2 of Figure 5.2) is deactivated, to illustrate the process's ability to find an optimum response from a relatively poor initial fine response.

The full-wave fine model, implemented in FEKO, is meshed as the example design of Figure 5.10. The response has a solution time of 224.1s.

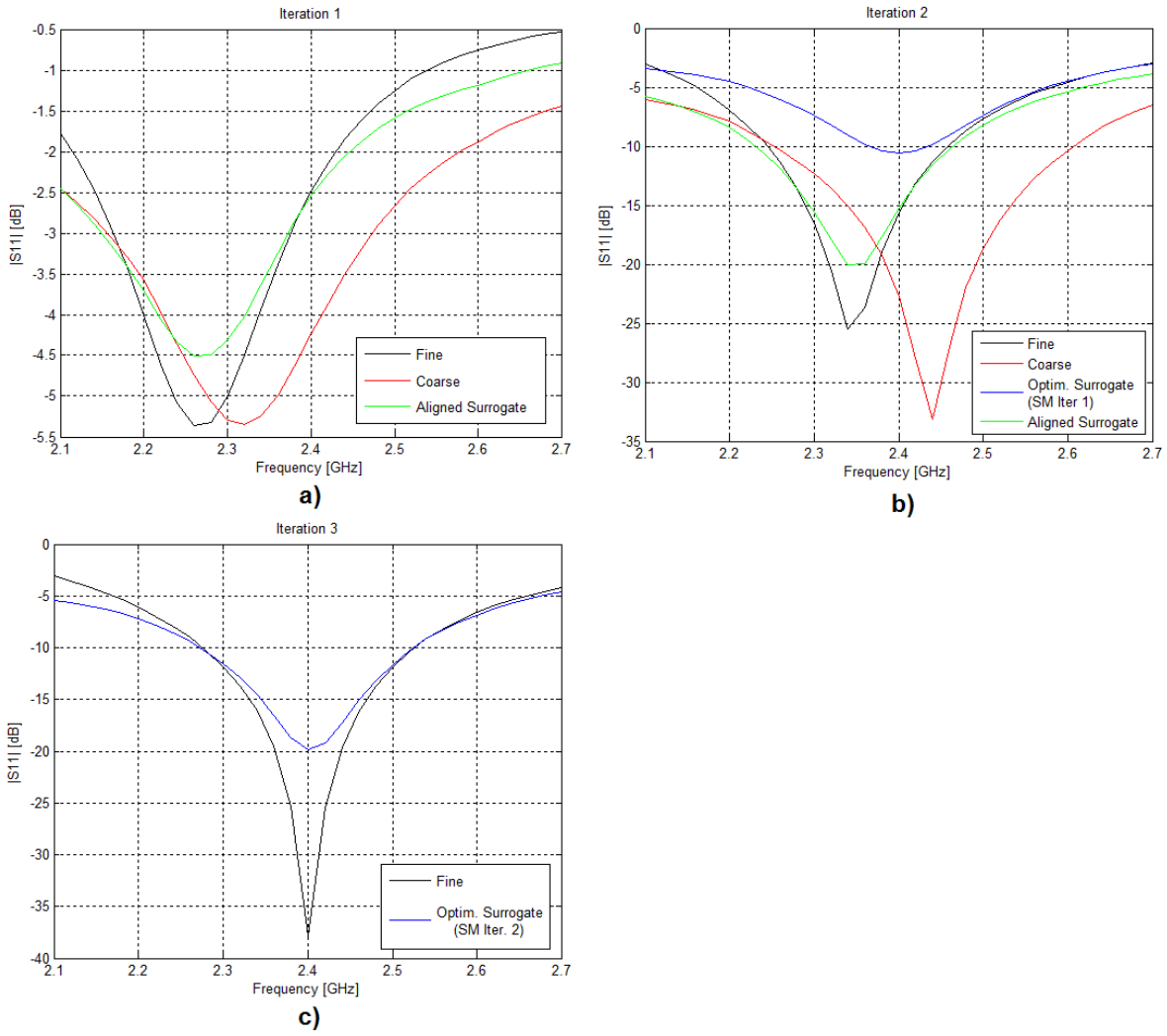

Figure 5.11 - Aperture-fed patch antenna Input SM example- TLM coarse model results

Figure 5.11 shows the results of the TLM coarse model's Input SM process. The initial coarse response in Iteration 1 is clearly far from the optimum desired response. The surrogate manages to match the fine response's resonant frequency, but does not quite match the magnitude or the slope of the response curve. Nonetheless, the optimised surrogate response of Iteration 1 (blue plot of Figure 5.11b) possesses the desired resonant frequency, and produces a fine response in Iteration 2 that is close to the desired resonance. The aligned surrogate of Iteration 2 is well-matched to the fine response.

The final fine response (pink plot of Figure 5.11b) after the surrogate optimisation of Iteration 2 possesses the desired resonant frequency and a bandwidth of 0.24 GHz (10% FBW) below the target -10 dB magnitude. The set of inputs for the final response are $L_0 = 26$ mm, $L_{ap} = 23.4$ mm, $L_{tune} = 9$ mm. The total solver time for the entire SM process is 829.8s.

5.5 Linear Antenna Array SM

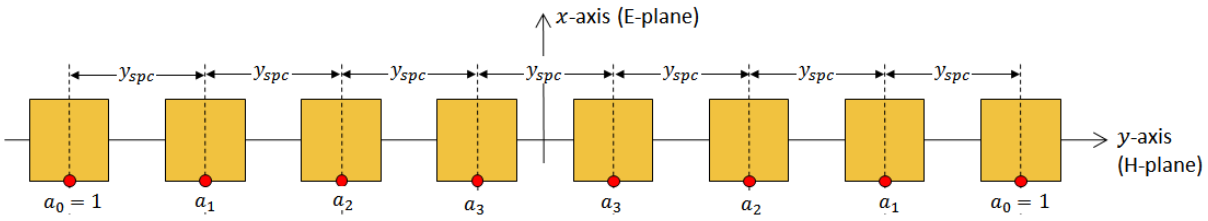

Figure 5.12- 1xN (N=8) array spacing and amplitude coefficients

The second application of SM to the overall design procedure is to optimise the radiation pattern of a linear, uniformly-spaced, nonuniform-amplitude finite patch antenna array. The H-plane element spacing y_{spc} and symmetrical amplitude weights $a_{1\ldots}\ a_{N-1}$ (for an even-numbered $2N$-element array) are to be used as input parameters. A full-wave FEKO simulation will be used as the fine model, and an analytical model based on the patch element's array-factor (AF) will be used as the coarse model.

5.5.1 Response and Cost Function

The H-plane farfield realised gain of the antenna array, calculated at the desired resonant frequency, is chosen for the response function:

$$R(\boldsymbol{x}, \theta_k) \equiv |G_r(\theta_k, \phi)| \ \ |_{\phi=90°} \qquad\qquad k \in 1,2 \ldots m \qquad\qquad (5.10)$$

Where:

$$\theta_k \equiv \left(\frac{k-1}{m}\right) \cdot 180° \qquad\qquad (5.11)$$

The geometric symmetry of the patch elements about the E-plane axis will produce a symmetrical pattern in θ about the broadside angle ($\theta = 0°$). The gain pattern is thus sampled across m points in elevation angle θ, from $0 - 180°$.

The primary goal of this optimisation is to minimise the H-plane sidelobe level (SLL) of the gain pattern. Although there is no strict specification on H-plane beamwidth for this design problem, the 3dB-beamwidth is included as a secondary goal should the designer wish to include such a requirement. The cost function therefore is defined as:

$$c_0 \equiv w_{SLL}\left|\frac{SLL - SLL_{goal}}{SLL_{goal}}\right| + w_{beam}\left|\frac{\theta_{beam} - \theta_{goal}}{\theta_{goal}}\right| \quad (5.12)$$

Where SLL_{goal} is the desired SLL, θ_{goal} is the desired 3dB-beamwidth, w_{SLL} is the SLL weighting factor and w_{beam} is the 3dB-beamwidth weighting factor.

The merit terms of the cost function, SLL and θ_{beam}, are defined as per the definitions of SLL and 3dB-beamwidth in Section 2.1.2.

5.5.2 Choice of SM Technique

The primary goal of the array optimisation process is to minimise the array radiation pattern's SLL. One of the chosen approaches is adapted from [2], which makes use of standard additive OSM ($\vec{\boldsymbol{d}}$) to match a full-wave fine antenna radiation pattern to an analytical AF-based coarse pattern:

$$R_s(\boldsymbol{x}, \theta_k) = R_c(\boldsymbol{x}, \theta_k) + D(\theta_k) \quad (5.13)$$

$D(\theta_k)$ is simply the difference between the fine and coarse radiation responses. It is assumed in [2] that the fine and coarse responses share the same pattern nulls, and remain so throughout the optimisation process. The assumption is not applicable to this SM process, since the chosen input parameters are certain to change the widths of the main-lobe and sidelobes as they are varied during optimisation. Figure 5.13a shows an example of standard OSM applied to fine and coarse responses whose nulls do not overlap, and the resulting $D(\theta_k)$ function.

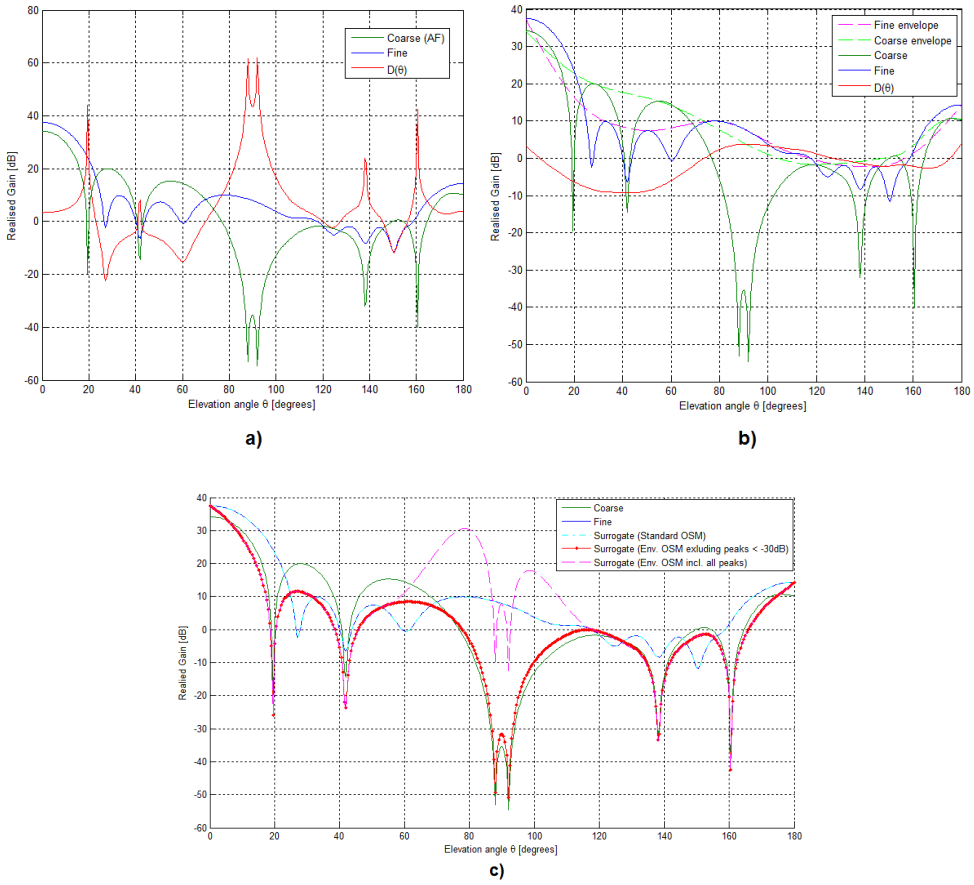

Figure 5.13- a) D(θ_k) using Standard OSM, b) D(θ_k) using OSM with envelope functions, c) OSM Surrogate response comparison

While the use of standard OSM here would match the coarse and fine response exactly at the current point in the parameter space, it would create a severely misaligned surrogate for most other inputs. To avoid this, the surrogate is built using envelope functions $R_{env}(\theta_k)$ of the fine and coarse responses. The envelope function of a response is constructed by identifying its peaks, and creating an interpolant function between them. This is easily computed in an environment such as MATLAB, where the *interp1* function is a built-in function [46] and the *peakseek* function is available as an open-source M-file [47].

Figure 5.13b shows the envelopes of the fine and coarse responses, represented as purple and green dashed-line plots respectively. It should be noted that the peak near $\theta = 90°$ is not included in the envelope because it is practically at the magnitude of a null, and would distort the surrogate response just as badly. The *peakseek* function is capable of filtering out peaks below a minimum amplitude [47], which must be pre-set before the SM process is initialised. In the case of Figure 5.13b, the minimum amplitude is set to -30dB.

The surrogate response for OSM, with envelope functions, is given by:

$$R_s(\boldsymbol{x}, \theta_k) = R_c(\boldsymbol{x}, \theta_k) + D_{env}(\theta_k) \qquad (5.14)$$

where:

$$D_{env}(\theta_k) = R_{f.env}(\theta_k) - R_{c.env}(\theta_k) \quad (5.15)$$

$R_{c.env}$ and $R_{f.env}$ are the coarse and fine envelope functions, respectively. Figure 5.13b shows $D_{env}(\theta_k)$, which is clearly a smoother function than $D(\theta_k)$ and which does not possess any of the sharp features created by the nulls in the fine and coarse responses.

Figure 5.13c compares the surrogate responses of standard OSM against OSM with envelope functions, plotted both with and without the peak near $\theta = 90°$ included in the coarse response's envelope. It can be seen that, when the peak near $\theta = 90°$ is included, the surrogate response is well-aligned at $\theta = 90°$ but significantly distorted around $\theta = 80°$ and $\theta = 100°$. When the peak is excluded, however, the surrogate response's profile fits the fine response well across the entire θ-range. The example SM process in Section 5.5.4 uses $D_{env}(\theta_k)$ to show the effectiveness of using envelope functions for OSM on radiation patterns.

Since the AF-based coarse model has a solution time of 0.179s, it can also accommodate Input SM. In the following subsection, OSM, Input SM and a combination of the two are performed on an example 1x8 patch array and their performance is compared.

5.5.4 Array SM Example

In this section, a set of SM processes are applied to the design of a 1x8 basic patch antenna array. The patch elements are designed to resonate at 2.4 GHz, and is built on a substrate with $h_0 = 9\ mm$, $\varepsilon_{rp} = 3.5$. The following SM processes are performed on the design example:

- Input SM
- OSM
- Input SM combined with OSM

The SM process is limited to 3 full SM iterations, with only the fine model being evaluated in Iteration 4. The aim of the optimisation is to attain an H-plane realised gain pattern $|G_r(\theta, 90°)|$ with $SLL \leq -20$ dB and $\theta_{beam} \leq 10°$. The starting value for the input parameters are $y_{spc} = 62.5$ mm (half-wavelength spacing), $a_0 = 1$, $a_1 = 1.9783$, $a_2 = 3.0965$, $a_3 = 3.8136$. The starting values of $a_0 \dots a_3$ are determined as the Dolph-Chebyshev distribution for a 1x8 array with $SLL = -30$ dB [48]. The distribution is calculated for $SLL = -30$ dB to give the initial response a wide main-beam, to determine which of the SM techniques are capable of balancing the desired SLL and 3dB-beamwidth.

The response is sampled at $m = 181$ points over the elevation angle range of $\theta \in [0;180]°$, for both the fine and coarse models at 2.4 GHz. All local optimisations are controlled by the Nelder-Mead Simplex algorithm and global optimisations are controlled by the PBIL algorithm. The PBIL process is

set to a 12-bit initial chromosome, a population size of 500 and a maximum number of 20000 coarse model evaluations. Global optimisation is set to be used on the coarse/surrogate optimisation throughout the SM process. The parameter extraction step is set to use local optimisation throughout the SM process.

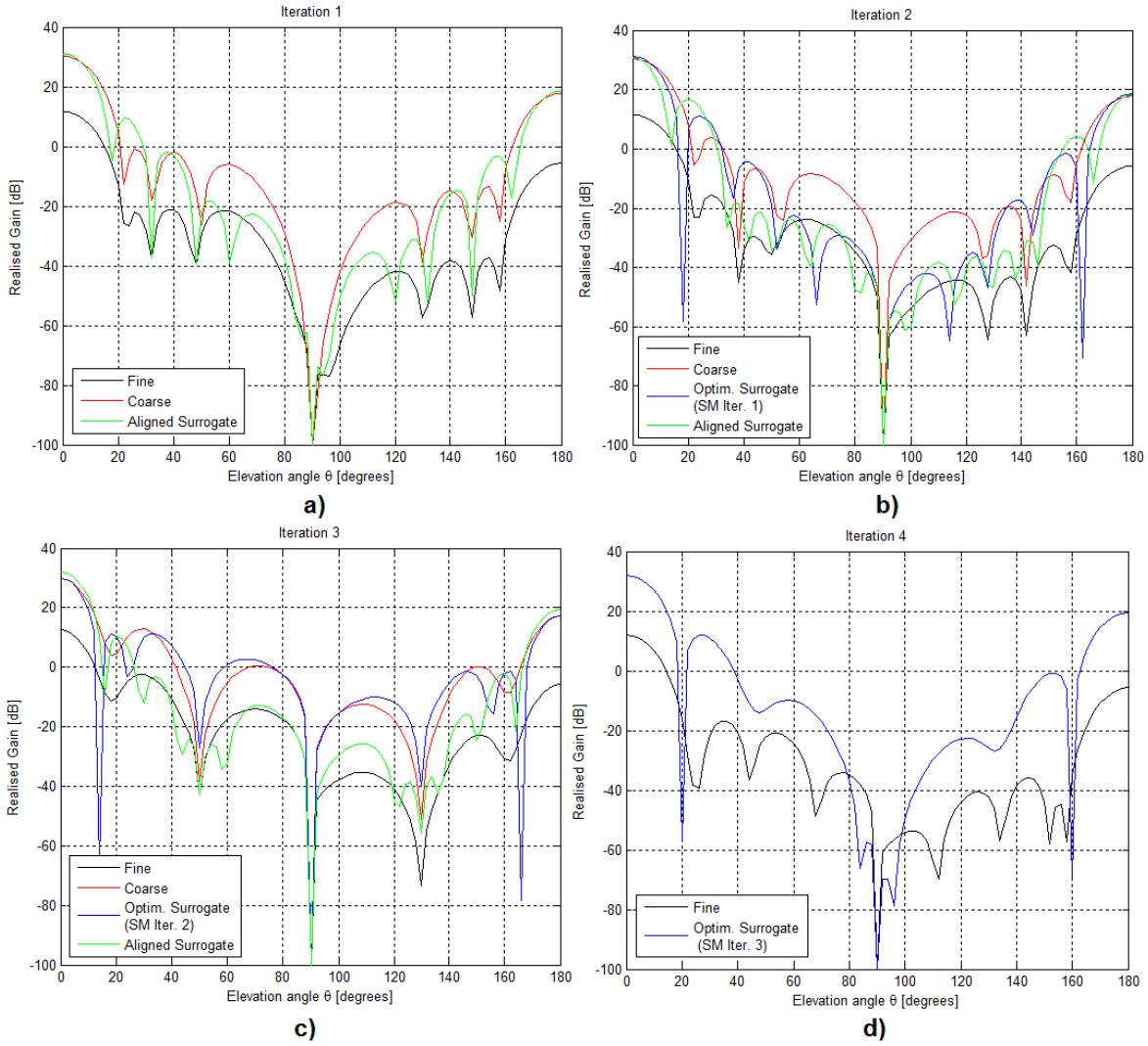

Figure 5.14- Array Input SM example- AF-based coarse model results

Figure 5.14 shows the results of the AF-based coarse model's Input SM process. The initial fine response exhibits $SLL = 32.8$ dB and $\theta_{beam} = 16°$. The surrogate is shown not to align very well with the fine model in any of the iterations, and the fine responses throughout the iterations do not improve for SLL or 3dB-beamwidth.

The final fine response (pink plot in Figure 5.14c) exhibits $SLL = 28.7$ dB and $\theta_{beam} = 13°$, which is significantly above the desired SLL but does not meet the target 3dB-beamwidth. The set of inputs for the final response are $y_{spc} = 67.1$ mm, $a_1 = 1.9281$, $a_2 = 3.0788$, $a_3 = 3.9648$. The total solver time for the entire SM process is 933.3s.

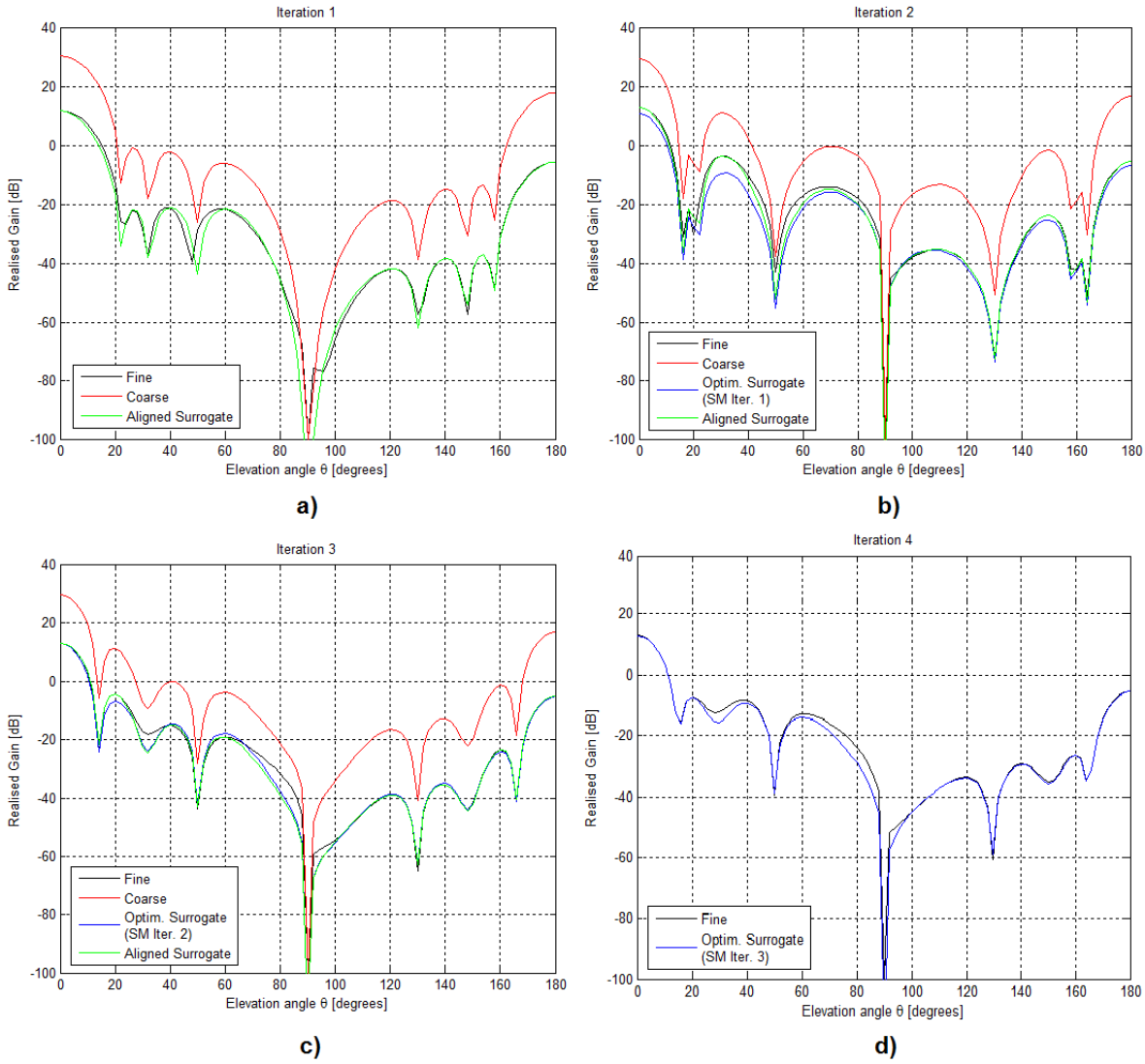

Figure 5.15 - Array OSM example- AF-based coarse model results

Figure 5.15 shows the results of the AF-based coarse model's OSM process, using envelope functions. The surrogate of Iteration 1 is shown to be well-aligned to the initial fine response. In Figure 5.15b, the surrogate has optimised Iteration 2's fine response to a narrower 3dB-beamwidth, although amplitude misalignment on the first sidelobe causes the SLL to lower undesirably. Iteration 3 improves the SLL, however, and further narrows the 3dB-beamwidth.

The final fine response (pink plot in Figure 5.15c) exhibits $SLL = 20.23$ dB and $\theta_{beam} = 10.7°$, which is above the desired SLL and 0.3° wider than the target 3dB-beamwidth. The set of inputs for the final response are $y_{spc} = 85.9$ mm, $a_1 = 1.7216$, $a_2 = 3.1131$, $a_3 = 2.6168$. The total solver time for the entire SM process is 878.34s.

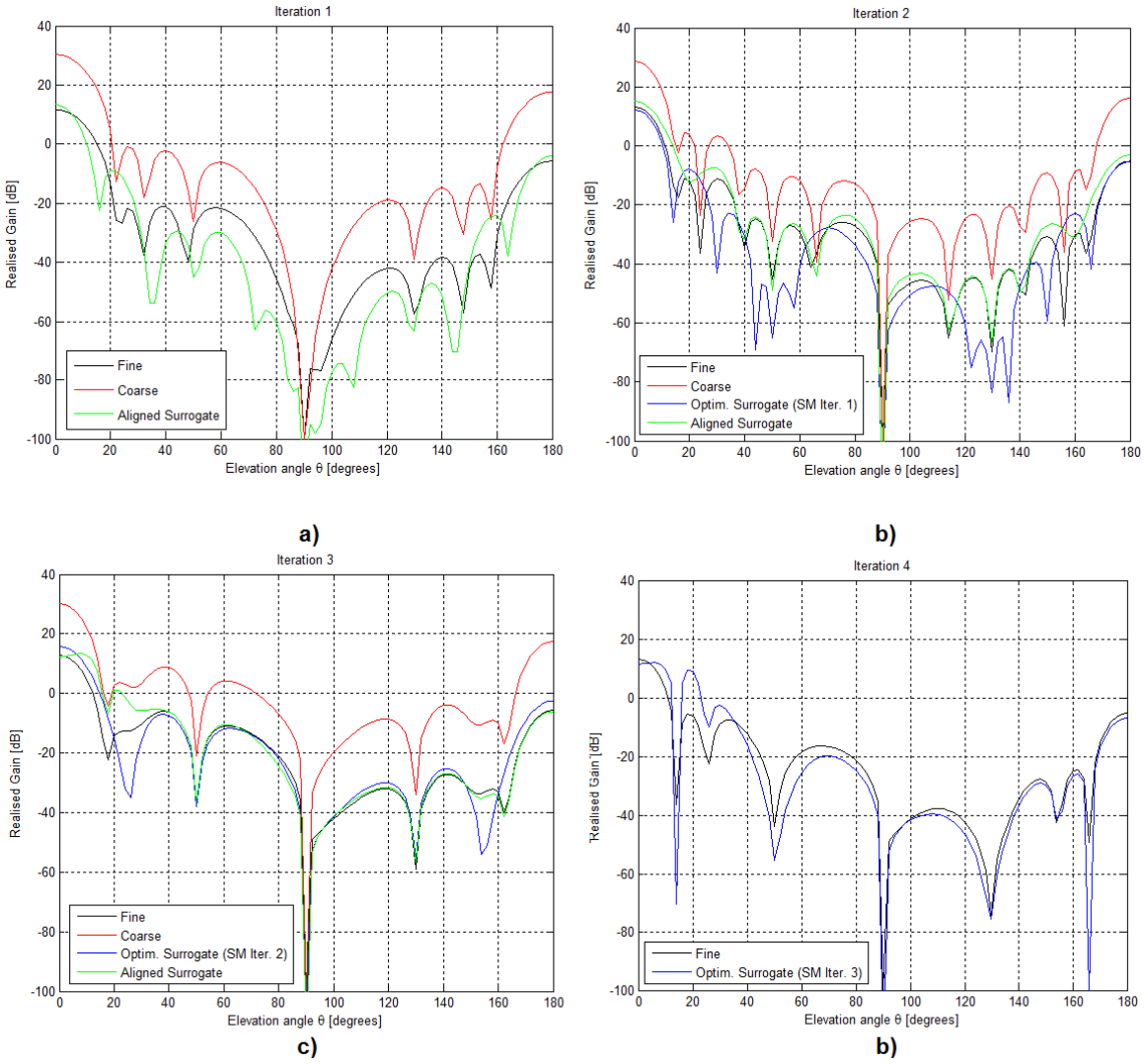

Figure 5.16 - Array Input SM/OSM example- AF-based coarse model results

Figure 5.16 shows the results of the AF-based coarse model's Input SM/OSM process, using envelope functions. The surrogate of Iteration 1 is shown to be reasonably well-aligned to the initial fine response, although it can be seen that the combination of Input SM and OSM does not function as well together as OSM by itself. In Figure 5.16b, the surrogate has optimised Iteration 2's fine response to $SLL = 24.3$ dB and $\theta_{beam} = 11.9°$.

Iteration 2 has the best fine response of the SM process, as the subsequent fine responses' sidelobes are driven up to the point where $SLL < 20$ dB. The set of inputs for the final response are $y_{spc} = 82.8$ mm, $a_1 = 2.4114$, $a_2 = 2.4609$, $a_3 = 3.0471$. The total solver time for the entire SM process is 1036.2s.

Table 5.5 - Array SM example summary

SM type	Total solver time [s]	3db-Beamwidth Error [°]	SLL error [dB]
Input	933.28	3	0
Output	878.34	0.7	0
Input + Output	1036.2	1.9	0

Table 5.5 summarises the results of the example array SM processes. Of the SM techniques considered for the AF-based coarse model, OSM produces the best results overall, achieving the desired SLL and having a minimal error in 3dB-beamwidth from the desired value. Input SM fares poorly in comparison, and is marginally slower than OSM. The combination of Input SM and OSM performs slightly worse than OSM and takes longer than Input SM to execute.

Given the results of this experiment, OSM (with envelope functions) is chosen as the SM technique to apply to the array design procedure of Chapter 7.

5.6 Conclusion

This chapter has provided a comprehensive analysis of the optimisation methods used in this thesis. An exposition of space mapping theory has been provided, as well as a discussion of various types of space mapping techniques. The application of space mapping to the design of patch elements and 1xN arrays has been discussed in detail, and the optimisation parameters and cost functions for each design problem have been developed. Finally, SM design examples have been provided to help ascertain which SM technique is best suited for each particular design problem.

Chapter 6

Design and Optimisation of 1x8 Patch Antenna Arrays

The previous chapters have thus far built up to describing a design process for a 1x8 array of patch antenna elements. In this chapter, the design procedure is laid out in a detailed and systematic manner to guide a designer through the process step-by-step.

The chapter begins with a discrete breakdown of the design of a 1x8 uniformly-spaced, nonuniform amplitude patch antenna array. The design process incorporates the patch element and array design, and determines the practical substrate dimensions for a finite PCB. Each step is further broken down into subprocesses that systematically outline the required tasks to complete the step.

A set of two example designs are also provide a demonstration of the design process for different patch elements and array configurations. The examples test the usefulness of basic probe-fed patch and aperture-fed patch structures as elements in an S-band antenna array design.

6.1 Design Strategy

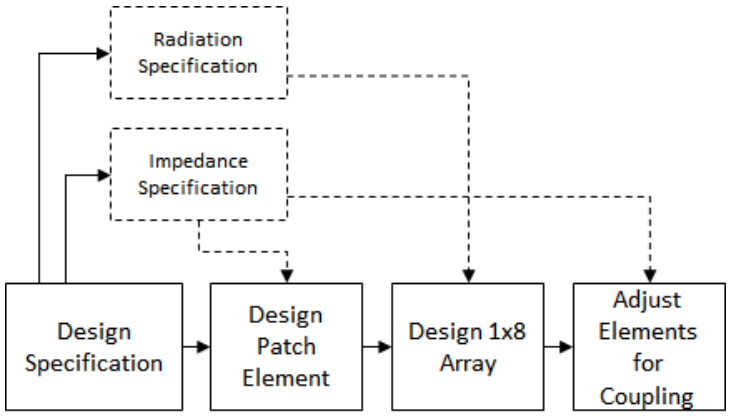

Figure 6.1 - Top-level design flowchart

Figure 6.1 shows the full design flowchart at its highest level of abstraction. The flowchart encompasses the entire design process from start to finish, and indicates the specification that governs each step of the process.

All of the SM optimisation procedures contained in this design method are centrally driven by a MATLAB script. The core of the MATLAB script is a general-purpose SM framework developed by Dr. D.I.L. de Villiers and Dr. R.D. Beyers of the University of Stellenbosch's Electrical and Electronic Engineering department.

6.1.1 Step 1 – Design Specification

The first step in the design process is to clearly define the performance requirements and design constraints of the antenna system. Three major outputs are generated by this step that feed into the subsequent steps of the design: an impedance specification, a radiation specification and an initial substrate specification.

The impedance specification defines the performance requirements of the patch antenna element in terms of its input impedance or reflection coefficient $|S_{11}|$ measured at the antenna's input terminals. The specification feeds into Step 2 and Step 4. The impedance specification comprises:

- Desired resonant frequency, in GHz
- Bandwidth/FBW, in GHz/%
- Passband magnitude, in dB

The radiation specification defines the performance requirements of the 1x8 patch array in terms of its H-plane farfield realised gain pattern $|G_r(\theta, 90°)|$. The specification feeds into Step 3, and comprises:

- Sidelobe level (SLL), in dB
- 3dB-Beamwidth, in degrees

The above terms are defined across the bandwidth defined in the impedance specification. In all of the designs of this chapter, it is further desired that linear polarisation is achieved along the E-plane. For the purposes of defining the realised gain for the individual antenna elements, the array elements must be fed and measured as laid out in Chapter 3.

The initial substrate specification is a design constraint that influences the impedance and radiation characteristics. For an array of basic probe/microstrip-fed patch elements, only a patch substrate needs to be specified. For an array of aperture-fed patch elements, both a patch and feed substrate must be specified. The specification comprises:

- Patch substrate height h_0, in mm
- Patch substrate permittivity ε_{rp}
- Feed substrate height h_f, in mm (if aperture-coupled patch elements are used)
- Feed substrate permittivity ε_{rf} (if aperture-coupled patch elements are used)

The substrate specification is labelled *initial* to reflect the fact that the substrate is not completely defined at this stage, and is modelled as an infinite structure in the xy-plane. In Step 3, the substrate's full set of finite dimensions are defined.

6.1.2 Step 2 – Design Patch Element

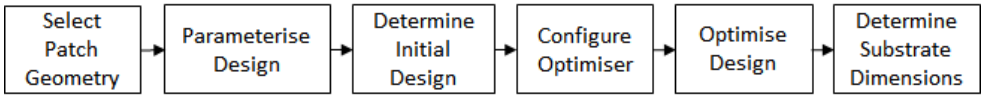

Figure 6.2- Step 2 (Design Patch Element) flowchart

The second step of the design procedure is patterned from the patch design examples of Chapter 5. Each step of the procedure required to design and optimise a patch antenna element is stated here, as is illustrated in Figure 6.2.

The patch element optimisation process uses the TLM coarse models developed in Chapter 4, implemented in AWR MWO 2010. The full-wave fine models are implemented in FEKO 7.0 and meshed according to the convergence studies of Chapter 3.

The patch geometry should be selected to fit the impedance and radiation specification. If a narrowband antenna is to be designed, then either a basic probe/microstrip-fed patch or aperture-fed patch can be used. A basic probe/microstrip-fed patch is recommended if cost and/or antenna volume is to be minimised, although the polarisation purity may not be as high as with an aperture-coupled patch. A basic probe/microstrip-fed patch also ensures a smaller radiation back-lobe than an aperture-fed patch due to its solid ground-plane. If a wideband antenna is to be designed, then an aperture-fed patch geometry must be used.

6.1.2.1 Basic Patch

The basic patch's input parameters must be defined, as well as the bounds of the parameter space. The input vector $[\![L_0\ W_0\ x_0]\!]$ is used, and the bounds of the basic patch's parameter space are set to:

$$\begin{bmatrix}\!\!\begin{bmatrix}0.75\cdot L_{0\cdot init}\\ 0.33\cdot W_{0\cdot init}\\ 0\end{bmatrix}\!\!\end{bmatrix} \leq \begin{bmatrix}\!\!\begin{bmatrix}L_0\\ W_0\\ x_0\end{bmatrix}\!\!\end{bmatrix} \leq \begin{bmatrix}\!\!\begin{bmatrix}1.25\cdot L_{0\cdot init}\\ L_{0\cdot init}\\ 0.5\cdot L_{0\cdot init}\end{bmatrix}\!\!\end{bmatrix} \qquad (6.1)$$

where $L_{0\cdot init}$ is the initial (starting) value for L_0. The initial design parameters must now be determined. The starting value for L_0 is given by Equation 2.13. To ensure initial excitation of the $TM^z{}_{100}$ patch mode, the starting value of W_0 is set to:

$$W_{0\cdot init} = 0.8\cdot L_0 \qquad (6.2)$$

The starting value of the inset E-plane feed-point distance x_0 is set to:

$$x_{0\cdot init} = 0.25\cdot L_0 \qquad (6.3)$$

The physical parametric settings of the basic patch design are now established, and the optimisation procedure must still be defined. Following the design example of Chapter 5, Input SM is chosen to be

applied to the optimisation process. The SM process is configured in the same manner as the basic patch SM design example of Chapter 5: the response is sampled at $m = 31$ points over a pertinent frequency range, for both the fine and coarse models. All local optimisations are controlled by the Nelder-Mead Simplex algorithm, and global optimisations are controlled by the PBIL algorithm. The PBIL process is set to a 7-bit initial chromosome, a population size of 100 and a maximum number of 1000 coarse model evaluations. Global optimisation is set to be used on the coarse/surrogate optimisation of the first SM iteration, and local optimisation thereafter. The parameter extraction step is set to use local optimisation throughout the SM process.

6.1.2.2 Aperture-fed Patch

The aperture-fed patch's input parameters must be defined, as well as the bounds of the parameter space. The input vector $[\![L_0\ L_{ap}\ L_{tune}]\!]$ is used, and the bounds of the aperture-fed patch's parameter space are set to:

$$\begin{bmatrix} 0.75 \cdot L_{0 \cdot init} \\ 0.75 \cdot L_{ap \cdot init} \\ 0.125 \cdot \lambda_{g \cdot f} \end{bmatrix} \leq \begin{bmatrix} L_0 \\ L_{ap} \\ L_{tune} \end{bmatrix} \leq \begin{bmatrix} 1.25 \cdot L_{0 \cdot init} \\ 1.1 \cdot L_{ap \cdot init} \\ 0.375 \cdot \lambda_{g \cdot f} \end{bmatrix} \qquad (6.4)$$

where $\lambda_{g \cdot f}$ is the guided wavelength of the feed-line within the feed substrate:

$$\lambda_{g \cdot f} = \frac{c_0}{f_0 \sqrt{\varepsilon_{rfeff}}} \qquad (6.5)$$

The upper bound of L_{ap} is more restrictive than its lower bound due to the observations made in Section 4.1.3.1, to prevent the TLM's accuracy from degrading for larger values of L_{ap}.

The initial design parameters must then be determined. The starting values for L_0 and W_0 are the same as for the basic patch, but in this case W_0 is a fixed parameter that does not vary during the optimisation process. The value of $L_{ap \cdot init}$ is pre-determined experimentally, for the reasons discussed in Section 6.4.1.1.

The pre-determined value of $L_{ap \cdot init}$ should produce a coarse model response that exhibits good coupling in the form of $|S_{11}|$'s magnitude below some acceptable threshold across any portion of the observed frequency range; a threshold of -10 dB is seen to work well. If a good starting value cannot be pre-determined, then the speed of the SM process using TLM coarse models allows the designer to run some test SM processes with a set of test values for $L_{ap \cdot init}$. A set of suggested of values for $L_{ap \cdot init}$ based on the desired FBW of the design are provided in Table 6.1.

Table 6.1 - Suggested values for $L_{ap\cdot init}$ based on desired FBW

FBW [%]	$L_{ap\cdot init}$ [mm]
1-2	$0.5 \cdot W_{0\cdot init}$
3-4	$0.75 \cdot W_{0\cdot init}$
5	$0.9 \cdot W_{0\cdot init}$
6-8	$1 \cdot W_{0\cdot init}$
9-10	$1.25 \cdot W_{0\cdot init}$

In order for the feed-side tuning stub to act as a transmission-line, it should be made long enough to prevent electromagnetic interaction between its open-end and the aperture. Fortunately, a stub length less than $\frac{\lambda_{g\cdot f}}{4}$ results in a large input reactance, which is not useful for counteracting the finite reactance of the aperture. The optimal tuning stub length is expected to be in the region of $\frac{\lambda_{g\cdot f}}{8} < L_{tune} < \frac{3\lambda_{g\cdot f}}{8}$ in order to provide the necessary tuning reactance [15]. Figure 6.3 shows the input reactance of an open-ended transmission-line vs. line length, and outlines the predicted region of the optimal stub length. The starting value for L_{tune} is therefore set to $\frac{\lambda_{g\cdot f}}{4}$, to occur in the middle of the optimal region.

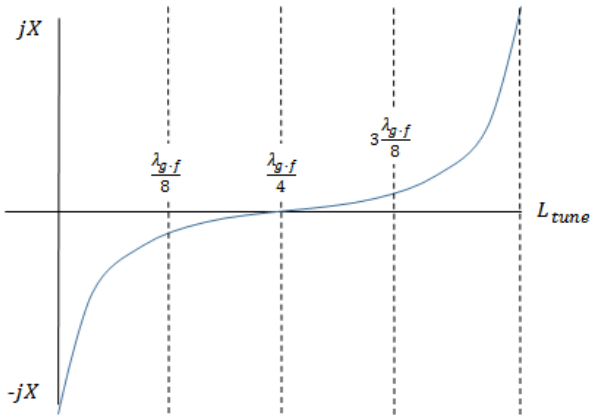

Figure 6.3 - Tuning stub input reactance vs. tuning stub length

The physical parametric settings of the aperture-fed patch design are now established, and the optimisation procedure must still be defined. Following the design example of Chapter 5, Input SM is chosen to be applied to the optimisation process. The SM process is configured in the same manner as the aperture-fed patch SM design example of Chapter 5: the response is sampled at $m = 31$ points over a pertinent frequency range, for both the fine and coarse models. All local optimisations are controlled by the Nelder-Mead Simplex algorithm, and global optimisations are controlled by the PBIL algorithm. The PBIL process is set to a 7-bit initial chromosome, a population size of 100 and a maximum number

of 1000 coarse model evaluations. Global optimisation is set to be used on the coarse/surrogate optimisation of the first SM iteration, and local optimisation thereafter. The parameter extraction step is set to use local optimisation throughout the SM process.

The finite dimensions of the substrate must then be determined. Until now, the patch elements and the array have been designed on infinite substrates; the finite substrates must therefore be made just large enough to produce a patch impedance response that matches that of an infinite substrate. This is done by beginning with a large set of substrate dimensions (for instance, 5-6 times the patch dimensions) and iteratively reducing them until the impedance responses begin to distort. The optimal substrate size is then the smallest size that gives an undistorted impedance response.

6.1.3 Step 3 – Design 1x8 Array

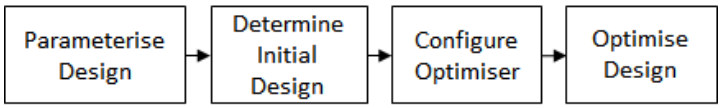

Figure 6.4 - Step 3 (Design 1x8 Array) flowchart

The third step of the design procedure is patterned from the array SM design example of Chapter 5. Each step of the procedure required to design the 1x8 array is stated here, as is illustrated in Figure 6.4. The procedure is applicable to a general 1x8 array of patch antenna elements, and can be used regardless of whether a basic patch or aperture-fed patch element was selected in Step 2.

The parameterisation of the antenna array is straightforward, as the patch elements' physical dimensions have already been optimised and are fixed in this step. The input parameters for the 1x8 array are the H-plane uniform element spacing y_{spc} and the symmetrical amplitude coefficients $[\![a_1\ a_2\ a_3]\!]$. The bounds of the aperture-fed patch's parameter space are set to:

$$\begin{bmatrix}\begin{bmatrix}0.4\cdot\lambda_0\\ a_{1\cdot min}\\ a_{2\cdot min}\\ a_{3\cdot min}\end{bmatrix}\end{bmatrix} \leq \begin{bmatrix}\begin{bmatrix}y_{spc}\\ a_1\\ a_2\\ a_3\end{bmatrix}\end{bmatrix} \leq \begin{bmatrix}\begin{bmatrix}0.6\cdot\lambda_0\\ a_{1\cdot init}+1\\ a_{2\cdot init}+1\\ a_{3\cdot init}+1\end{bmatrix}\end{bmatrix} \qquad (6.6)$$

where $a_{n\cdot min}$ is given by:

$$a_{n\cdot min} = \min[\![\,(a_{n\cdot init}-1)\,,\ \ 1\ ]\!] \qquad (6.7)$$

The amplitude coefficients are defined relative to the outermost amplitude coefficient $a_0 = 1$. Since amplitude windowing functions are usually minimum at the outermost elements and taper up in magnitude towards the central elements, as with the Dolph-Chebyshev distribution, the lower bounds of their dimensions of the parameter space must be greater than or equal to 1.

The initial design parameters must now be determined. The starting value for y_{spc} is typically set to a half-wavelength antenna array spacing:

$$y_{spc\cdot init} = 0.5 \cdot \lambda_0 \qquad (6.8)$$

Alternatively, a larger three-quarter-wavelength spacing is also suggested:

$$y_{spc\cdot init} = 0.75 \cdot \lambda_0 \qquad (6.9)$$

If the designer wishes to conserve board space and ensure that grating lobes will not appear in the radiation pattern, then $y_{spc} = 0.5 \cdot \lambda_0$ is recommended. If the designer wishes to minimise mutual coupling between the patch elements and/or remove the need for the adjustment process of Step 4, then $y_{spc} = 0.75 \cdot \lambda_0$ is recommended. A spacing of $0.75 \cdot \lambda_0$ is large enough to minimise mutual coupling on most patch array designs, but often it is also small enough to prevent grating lobes from distorting the radiation pattern.

The starting amplitude coefficients $[\![a_{1\cdot init}\ a_{2\cdot init}\ a_{3\cdot init}]\!]$ are set according to a Dolph-Chebyshev distribution, for the desired SLL.

The physical parametric settings of the basic patch design are now established, and the optimisation procedure must still be defined. Following the design example of Chapter 5, OSM is chosen to be applied to the optimisation process. The response is sampled at $m = 181$ points over the elevation angle range of $\theta = 0$-$180°$, for both the fine and coarse models at the desired resonant frequency. All local optimisations are controlled by the Nelder-Mead Simplex algorithm and global optimisations are controlled by the PBIL algorithm. The PBIL process is set to a 12-bit initial chromosome, a population size of 500 and a maximum number of 20000 coarse model evaluations. Global optimisation is set to be used on the coarse/surrogate optimisation throughout the SM process. The parameter extraction step is set to use local optimisation throughout the SM process.

Finally, the presence of a conductive back-plane must be simulated and observed. This step can be skipped if the antenna is not intended to be mounted on a larger, metallic structure, but in many design problems it will be the case (e.g. on an aircraft fuselage). For antennas that exhibit an undesired large back-lobe, such as an aperture-coupled patch, the problem can be mitigated by placing a reflector some distance behind the antenna. For an aperture-coupled patch, care must be taken not to mount the antenna too closely to the back-plane, as the presence of a conducting surface can affect the impedance properties of the feed-line and aperture [30]. A distance of $\frac{\lambda_0}{8}$ between the feed-line and back-plane has been observed to function adequately, and can be practically realised by mounting the antenna onto a dielectric material with $\varepsilon_r \cong 1$ (e.g. expanded polystyrene), which is then attached to the back-plane. If coplanar patch elements are used, then the ground-plane of the patch is the same as its back-plane.

6.1.4 Step 4 – Adjust Elements for Coupling

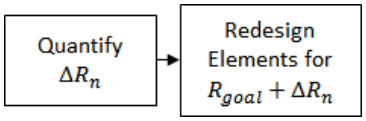

Figure 6.5 - Step 4 (Adjust Elements for Coupling) flowchart

Once the patch element and array layout is designed, the impedance responses of the individual patch elements within the array R_n $(n \in 1,2 \ldots N)$ must be inspected. If any of the impedance responses are distorted by some measure ΔR_n through mutual coupling, to the point where they no longer meet the element impedance specification, then their design parameters must be adjusted to mitigate the distortion. It should be noted that, since the antenna array is symmetrical, the distortion of the responses should be symmetrical; hence, $\Delta R_1 = \Delta R_8$, $\Delta R_2 = \Delta R_7$, and so on.

The distortion ΔR_n must be quantified for the element responses, in order to determine how the element must be adjusted. As is shown in [2], mutual coupling between patch elements often causes little more than a shift in resonant frequency shift Δf_n, and so the distortion can be quantified as $\Delta R_n = \Delta f_n$. If Δf_n is small and/or a wideband design is under consideration, it is sometimes sufficient to adjust L_0 by hand until the desired resonant frequency is restored for the patch element. Otherwise, the patch element must be run through an SM process again with a target resonant frequency of $f_0 - \Delta f_n$ [2].

6.2 Design I- 2.4 GHz Probe-fed Narrowband Patch Array

6.2.1 Design Specification

Table 6.2 tabulates the specifications of Design I. The impedance specification is the same as the design example of Section 5.3.4.

Table 6.2 - Design I Specification

IMPEDANCE SPECIFICATION	
f_0 [GHz]	2.4
FBW [%]	1
Passband $\lvert S_{11} \rvert$ [dB]	-10
RADIATION SPECIFICATION	
SLL [dB]	20
3dB-Beamwidth [°]	10

INITIAL SUBSTRATE SPECIFICATION	
No. of Layers	1
Patch layer h_0 [mm] / ε_{rp}	2 / 3.5

6.2.1 Patch Element Design

The SM process consists of 3 full SM iterations, with only the fine model being evaluated in Iteration 4. The starting value for the input parameters are $L_0 = 32.2$ mm, $W_0 = 30.3$ mm, $x_0 = 9.7$ mm.

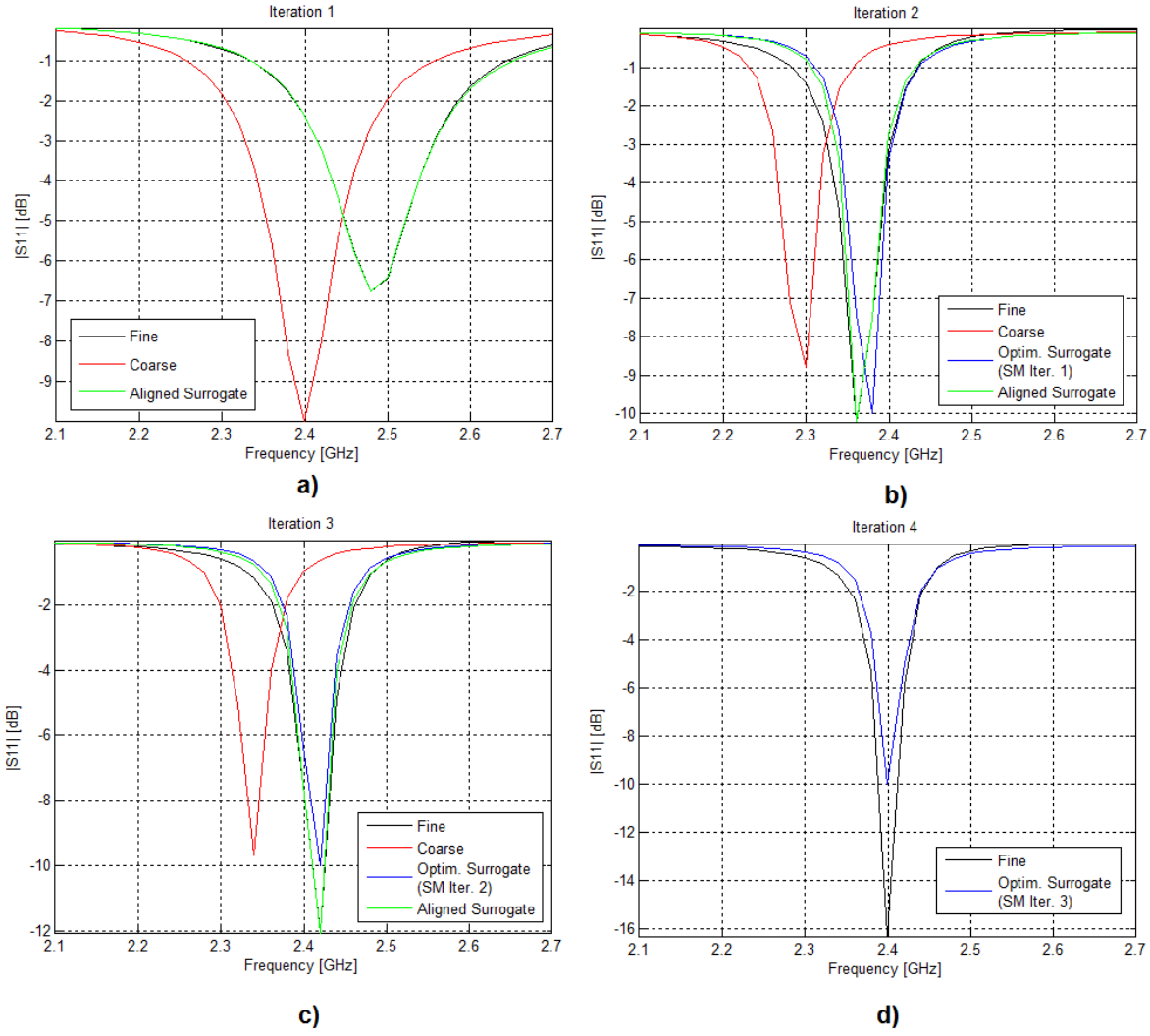

Figure 6.6 – Design I Patch Element SM Process

Figure 6.6 shows the results of Design I's patch Input SM process. The final fine response is correctly tuned to 2.4 GHz with $|S_{11}| = -16$ dB at resonance. The set of inputs for the final response are $L_0 = 34.3$ mm, $W_0 = 20.1$ mm, $x_0 = 15.3$ mm. The total solver time for the entire SM process is 927.4s.

6.2.2 Array Design

The SM process is chosen of consist of 2 full SM iterations, with only the fine model being evaluated in Iteration 3. The starting value for the input parameters are $y_{spc} = 62.5$ mm (half-wavelength spacing), $a_1 = 1.9783$, $a_2 = 3.0965$, $a_3 = 3.8136$.

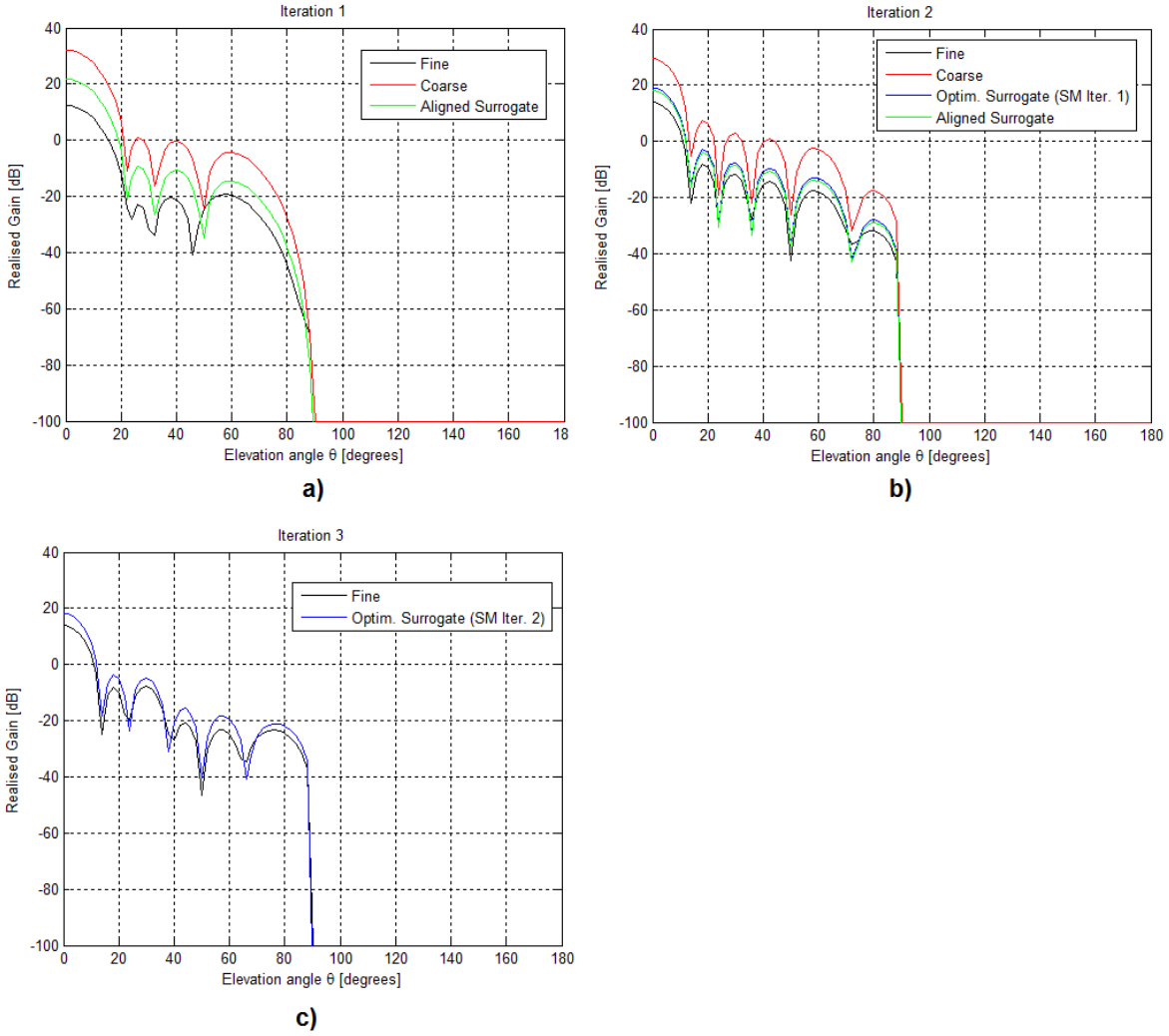

Figure 6.7 – Design I Array SM Process

Figure 6.7 shows the results of Design I's array OSM process. The final fine response exhibits $SLL = 22.14$ dB and $\theta_{beam} = 9.6°$, which is above the desired SLL and narrower than the target 3dB-beamwidth. The set of inputs for the final response are $y_{spc} = 84.5$ mm, $a_1 = 1.7105$, $a_2 = 2.0352$, $a_3 = 2.5222$. The total solver time for the entire SM process is 902.7s.

6.2.4 Full-wave Simulation

The full array is simulated on a finite substrate in CST MWS, using the Frequency Domain solver. It is found that a substrate 3.5 times larger than the patch dimensions is just large enough to sustain an

impedance response as if the antenna were mounted on an infinite substrate. After preliminary local meshing is applied, the adaptive meshing feature is activated and the solver is allowed to run for 8 iterations.

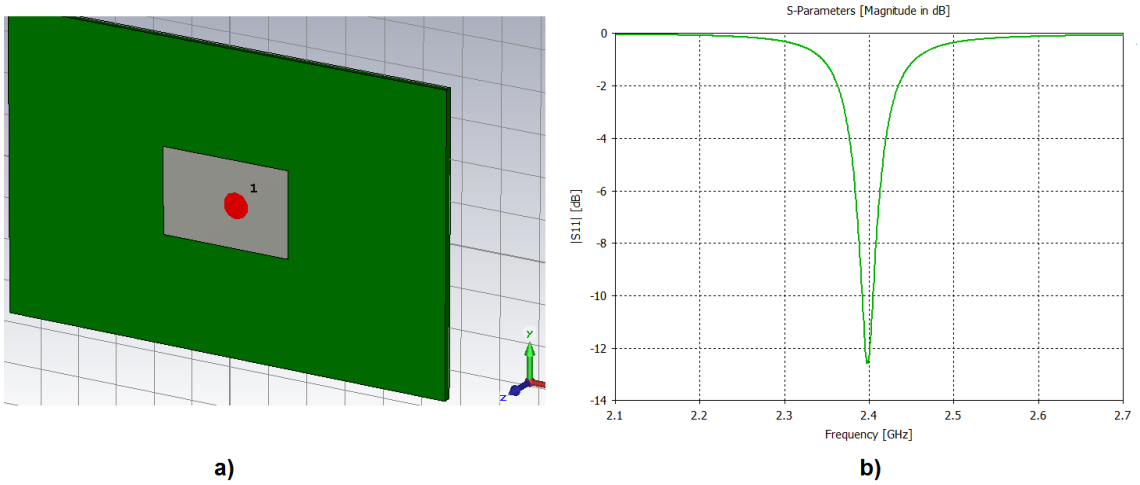

Figure 6.8 – Design I finite-substrate patch element in CST MWS: a) Isometric view, b) $|S_{11}|$

Figure 6.8a shows the modelled patch element on a finite substrate, modelled in CST MWS, while Figure 6.8b shows $|S_{11}|$ of the patch. It is clearly resonant at 2.4 GHz as designed, and functions the same as the patch mounted on an infinite substrate.

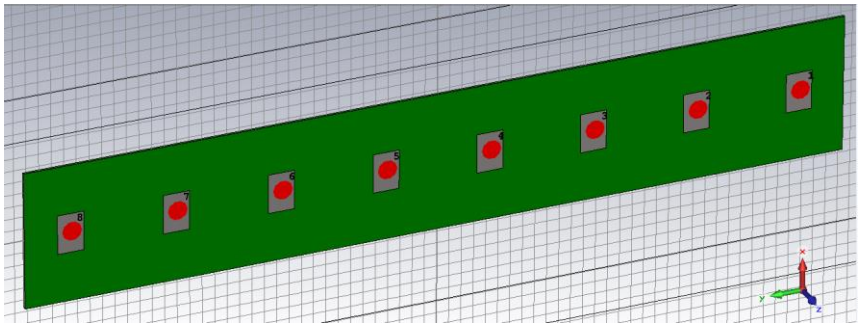

Figure 6.9 - Design I finite-substrate patch array in CST MWS

Figure 6.9 shows the modelled patch array on a finite substrate, modelled in CST MWS. The $x \times y$ dimensions of the substrate are 113.75 mm × 665.35 mm.

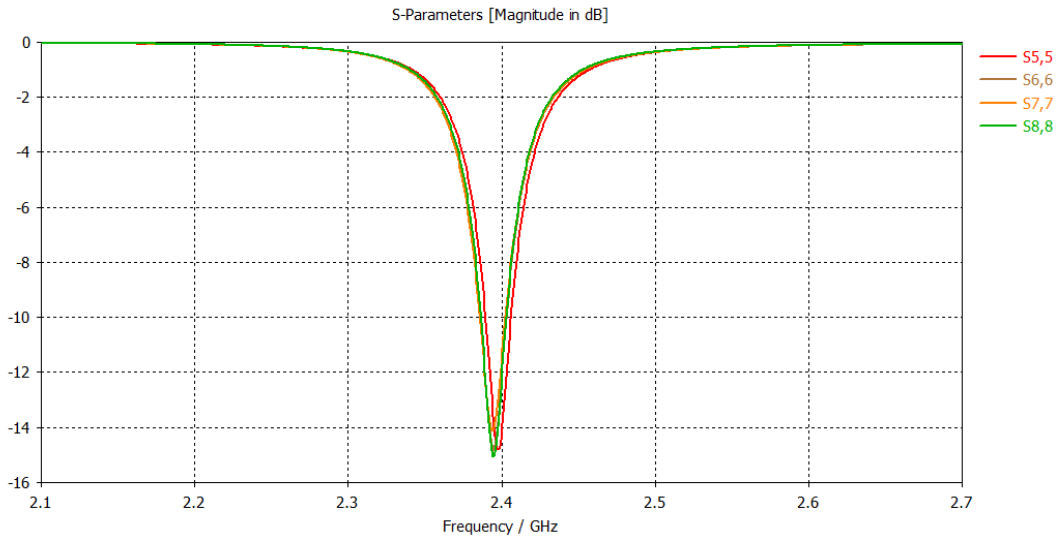

Figure 6.10 - $|S_{11}|$ of embedded array elements

Figure 6.10 shows the $|S_{11}|$ responses of the patch elements embedded in the array. Note that only 4 of the 8 elements are represented on one half of the array, because the symmetry of the array makes the mirrored elements' impedance responses duplicates of one another. In Figure 6.10, the response marked $S_{5,5}$ is the innermost element, and $S_{8,8}$ is the outermost element. It is clear from the figure that the responses are negligibly distorted by mutual coupling, and do not need to be adjusted through redesign.

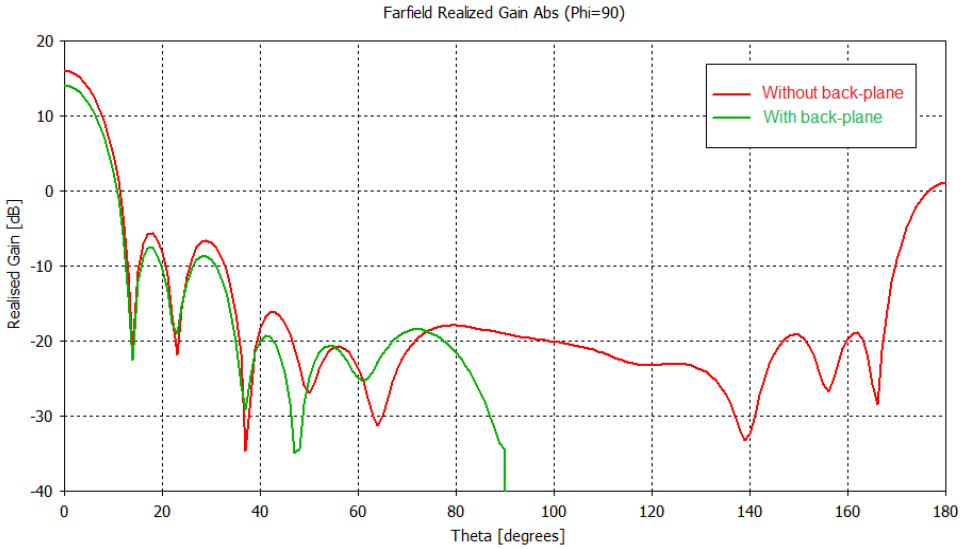

Figure 6.11 - Design I $|G_r(\theta, 90°)|$ at 2.4 GHz

Figure 6.11 shows the H-plane realised gain $|G_r(\theta, 90°)|$ of Design I, with and without the presence of a back-plane. It can be seen that the difference between the two plots are minimal in the main-lobe and two largest sidelobes. The realised gain pattern with the back-plane present drops slightly in its maximum broadside gain, but its SLL remains the same as the gain without the back-plane.

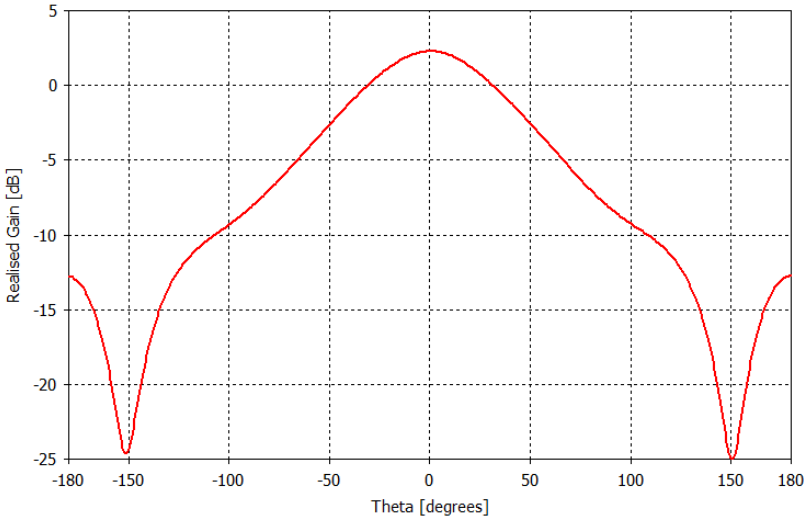

Figure 6.12 - Design I $|G_r(\theta, 0°)|$

Figure 6.12 shows the E-plane realised gain $|G_r(\theta, 0°)|$ of Design I. The E-plane pattern is inspected specifically to determine if the asymmetric placement of the feeding probe. The pattern barely exhibits asymmetry due to the probe, and is considered effectively symmetrical.

Table 6.3 – Design I Results Summary (measured at 2.4 GHz)

Resonant Frequency [GHz]	2.4
FBW [%]	1
SLL [dB]	21.7
3dB-Beamwidth [°]	10.25
Broadside Realised Gain [dB]	15.6
Axial Ratio (E-plane/H-plane) [dB]	40
Front-back Ratio (no back-plane) [dB]	15.1

Table 6.3 summarises the results of Design I. The design has fully met its impedance specification and has almost fully met its radiation specification; 3dB-beamwidth is 0.25° wider than specified, but this is an almost negligible error. Furthermore, the realised gain pattern's axial ratio is 40 dB, indicating very pure linear polarisation in the E-plane.

6.3 Design II- 2.4 GHz Aperture-fed Wideband Patch Array

6.3.1 Design Specification

Table 6.4 tabulates the specifications of Design II. The impedance specification is the same as the design example of Section 5.4.3, and the radiation specification is the same as the design example of Section 5.5.4.

Table 6.4 - Design II Specification

IMPEDANCE SPECIFICATION	
f_0 [GHz]	2.4
FBW [%]	10
Passband $\|S_{11}\|$ [dB]	-10
RADIATION SPECIFICATION	
SLL [dB]	20
3dB-Beamwidth [°]	15
INITIAL SUBSTRATE SPECIFICATION	
No. of Layers	2
Patch layer h_0 [mm] / ε_{rp}	9 / 3.5
Feed layer h_f [mm] / ε_{rf}	0.5 / 3.5

6.3.1 Patch Element Design

The patch SM process consists of 2 full SM iterations, with only the fine model being evaluated in Iteration 3. The starting value for the input parameters are $L_0 = 28.5$ mm, $L_{ap} = 20$ mm, $L_{tune} = 18.9$ mm, and the fixed physical parameters are set to $W_0 = 22.8$ mm, $W_{ap} = 1$ mm, $w_f = 1.1$ mm.

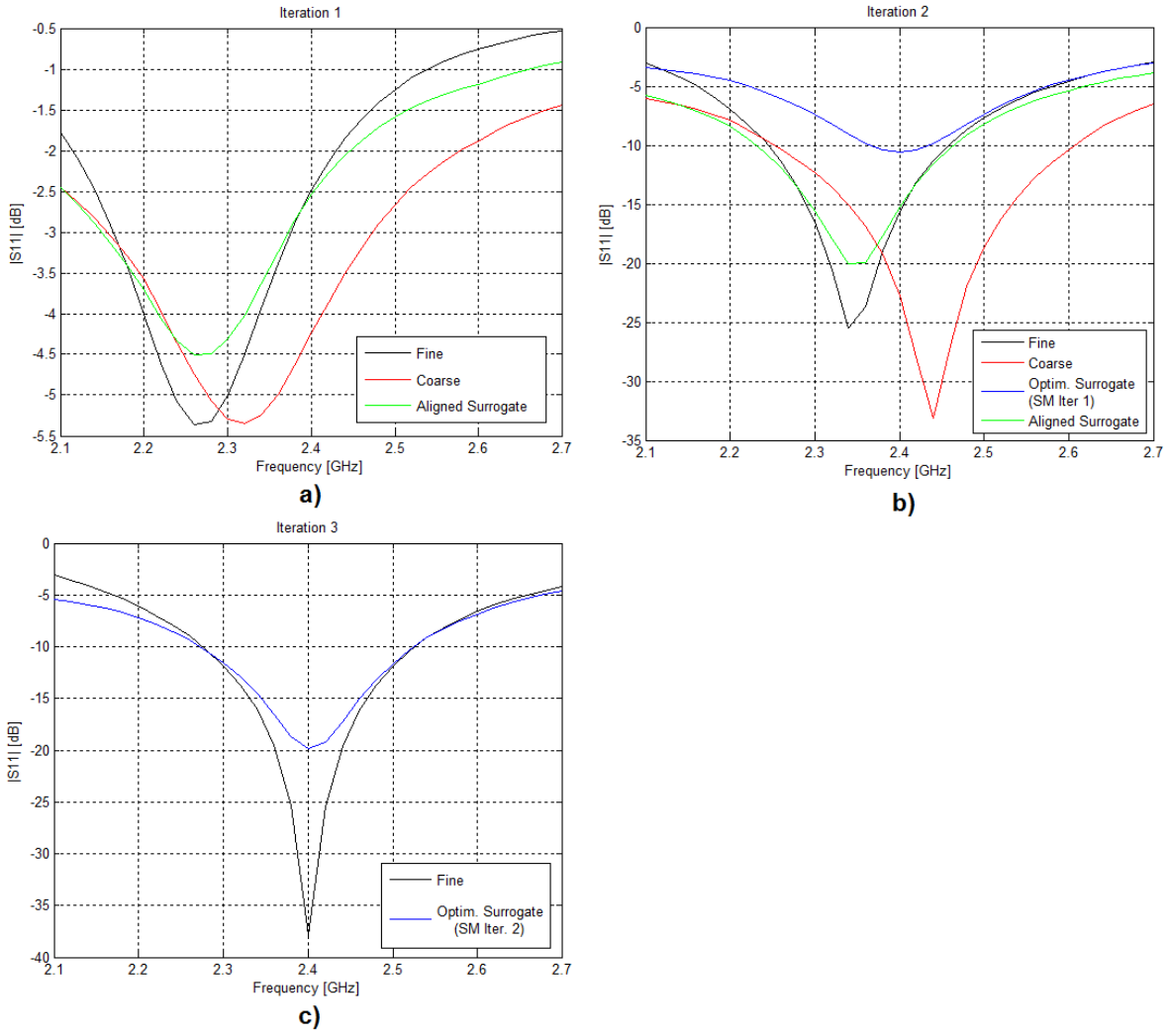

Figure 6.13– Design II Patch Element SM Process

Figure 6.13 shows the results of Design II's patch Input SM process. The final fine response is correctly tuned to 2.4 GHz with $|S_{11}| = -37$ dB at resonance, with a bandwidth of 0.24 GHz (10% FBW). The set of inputs for the final response are $L_0 = 26$ mm, $L_{ap} = 23.4$ mm, $L_{tune} = 9$ mm. The total solver time for the entire SM process is 829.8s.

6.3.2 Array Design

The array SM process consists of 3 full SM iterations, with only the fine model being evaluated in Iteration 4. The starting value for the input parameters are $y_{spc} = 62.5$ mm (half-wavelength spacing), $a_1 = 1.9783$, $a_2 = 3.0965$, $a_3 = 3.8136$.

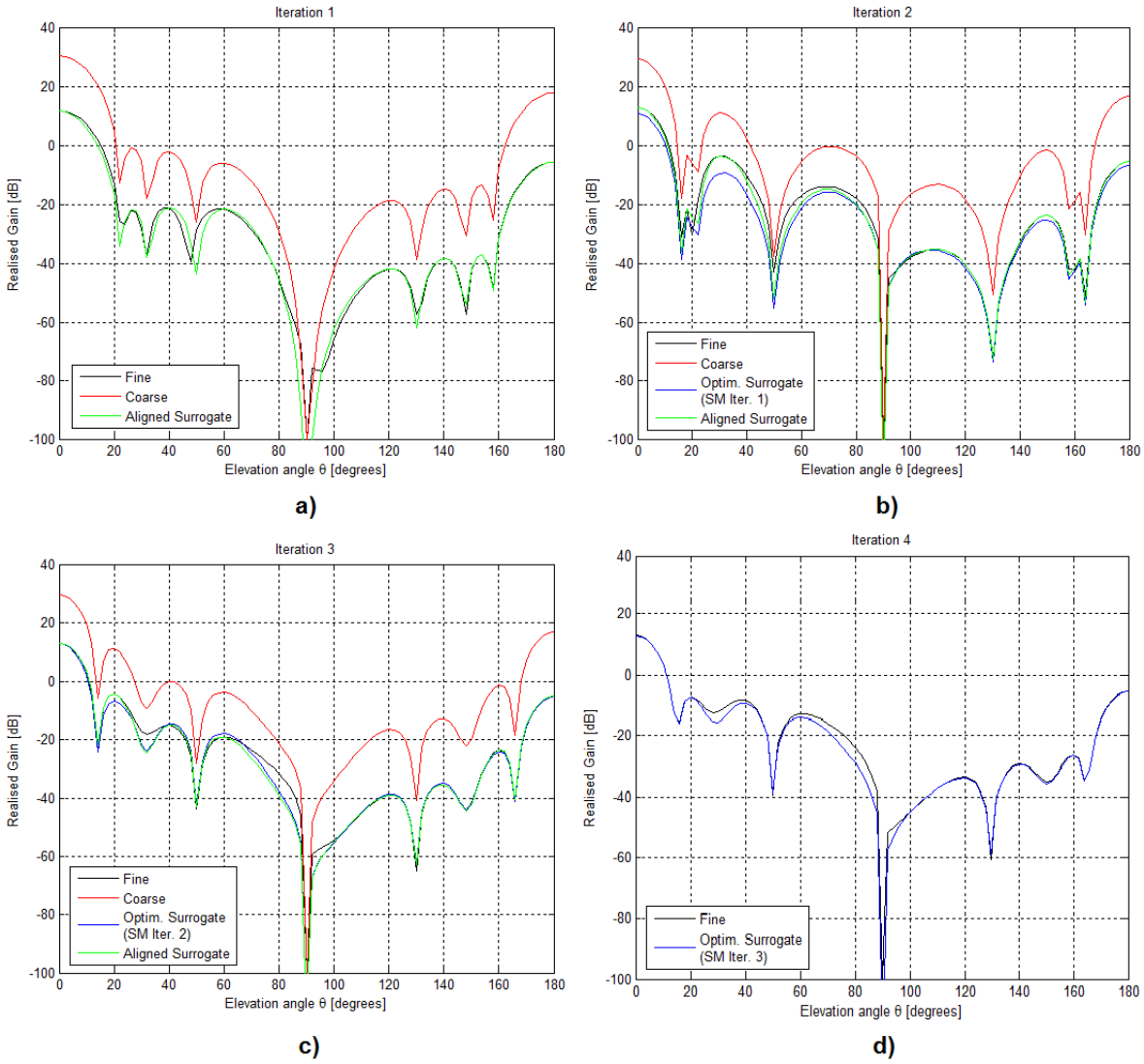

Figure 6.14 – Design II Array SM Process

Figure 6.14 shows the results of Design II's array OSM process. The final fine response exhibits $SLL = 20.23$ dB and $\theta_{beam} = 10.7°$, which is above the desired SLL and 0.3° wider than the target 3dB-beamwidth. The set of inputs for the final response are $y_{spc} = 85.9$ mm, $a_1 = 1.7216$, $a_2 = 3.1131$, $a_3 = 2.6168$. The total solver time for the entire SM process is 878.34s.

6.3.4 Full-wave Simulation

The full array is simulated on a finite substrate in CST MWS, using the Frequency Domain solver. It is found that a substrate 4 times larger than the patch dimensions is just large enough to sustain an impedance response as if the antenna were mounted on an infinite substrate. After preliminary local meshing is applied, the adaptive meshing feature is activated and the solver is allowed to run for 8 iterations.

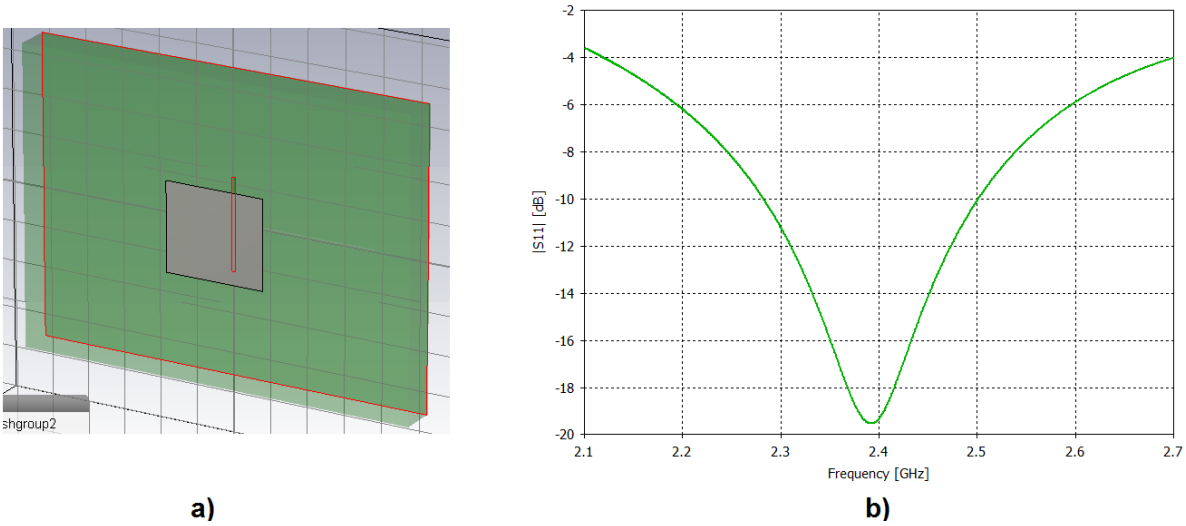

Figure 6.15 – Design II finite-substrate patch element in CST MWS: a) Isometric view, b) $|S_{11}|$

Figure 6.15a shows the modelled patch element on a finite substrate, modelled in CST MWS, while Figure 6.15b shows $|S_{11}|$ of the patch. It is clearly resonant at 2.4 GHz as designed, and functions the same as the patch mounted on an infinite substrate with a very similar bandwidth.

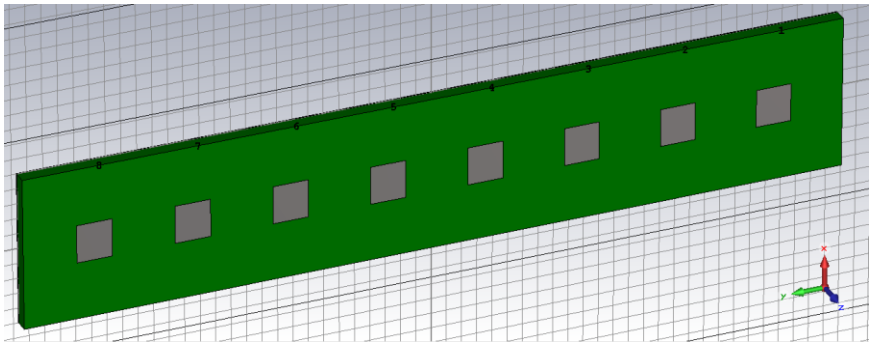

Figure 6.16 - Design II finite-substrate patch array in CST MWS

Figure 6.16 shows the modelled patch array on a finite substrate, modelled in CST MWS. The $x \times y$ dimensions of the substrate are 100 mm × 533.2 mm.

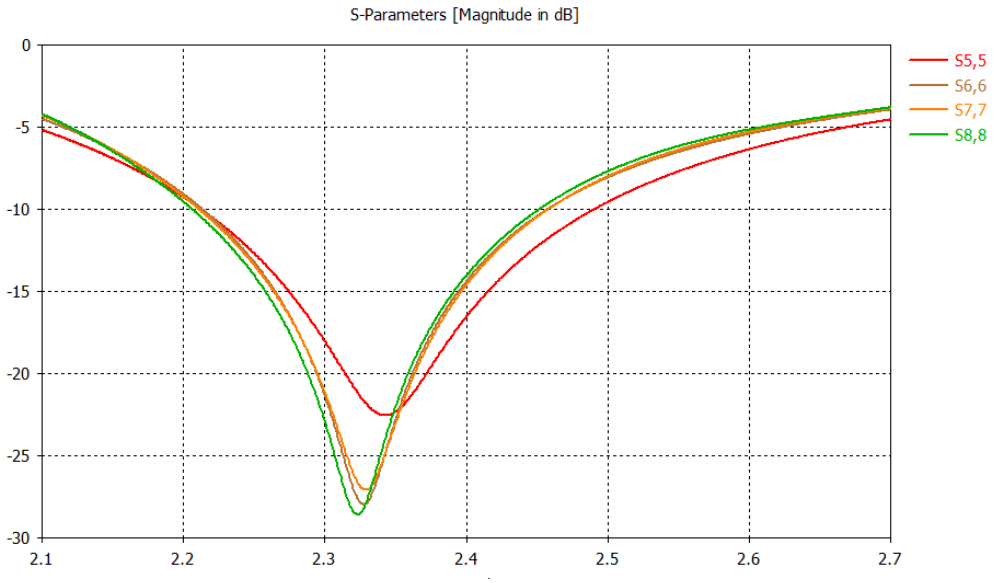

Figure 6.17 - $|S_{11}|$ of embedded array elements before adjustment for mutual coupling

Figure 6.17 shows the $|S_{11}|$ responses of the patch elements embedded in the array, before adjustments for coupling are made. The elements' responses are all shifted down in frequency, although their bandwidths are not altered. The innermost element's response S_{55} is shifted marginally less than the others.

The patch lengths are adjusted by hand to mitigate the frequency shift. As a first attempt, the lengths are all altered so that $L_0 = 25$ mm. The adjusted set of $|S_{11}|$ responses are illustrated in Figure 6.18.

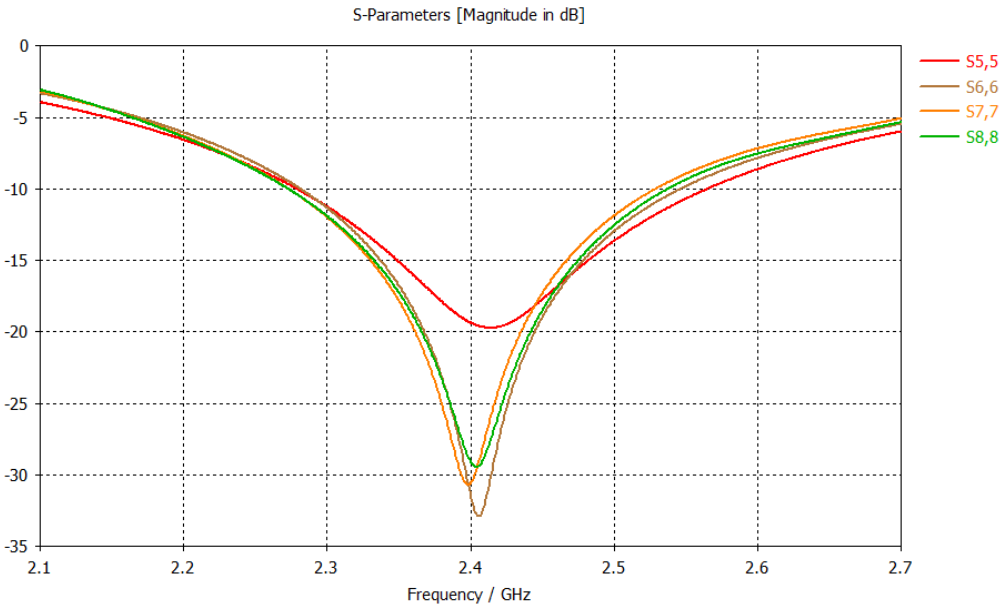

Figure 6.18- $|S_{11}|$ of embedded array elements after adjustment for mutual coupling

The responses are shown to be re-centred at 2.4 GHz, without loss of bandwidth. The adjustment by hand is thus sufficient for this particular design problem.

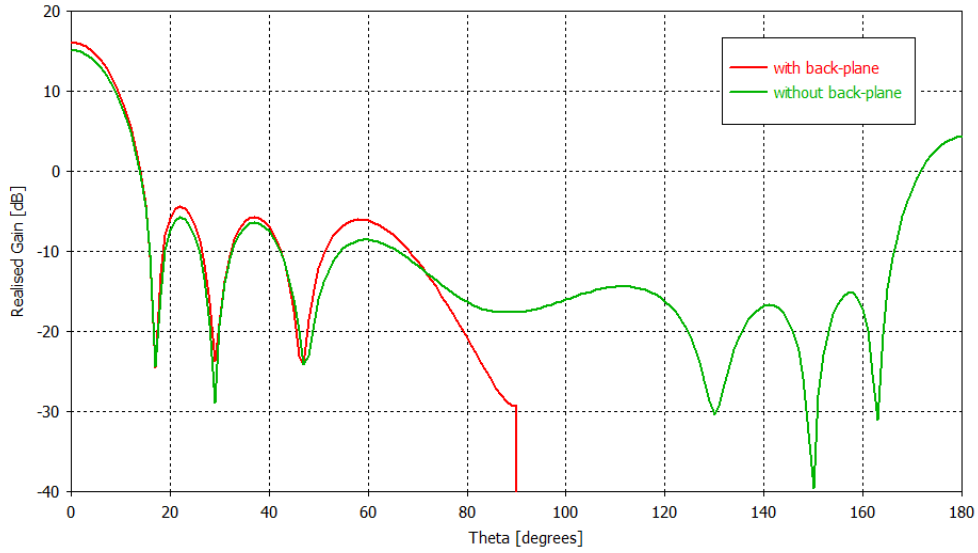

Figure 6.19 - Design II $|G_r(\theta, 90°)|$ at 2.4 GHz

Figure 6.19 shows the H-plane realised gain $|G_r(\theta, 90°)|$ of Design II, with and without the presence of a back-plane. It can be seen that the difference between the two plots are minimal in the main-lobe and two largest sidelobes. The realised gain pattern with the back-plane present raises slightly in its maximum broadside gain, but its SLL remains the same as the gain without the back-plane.

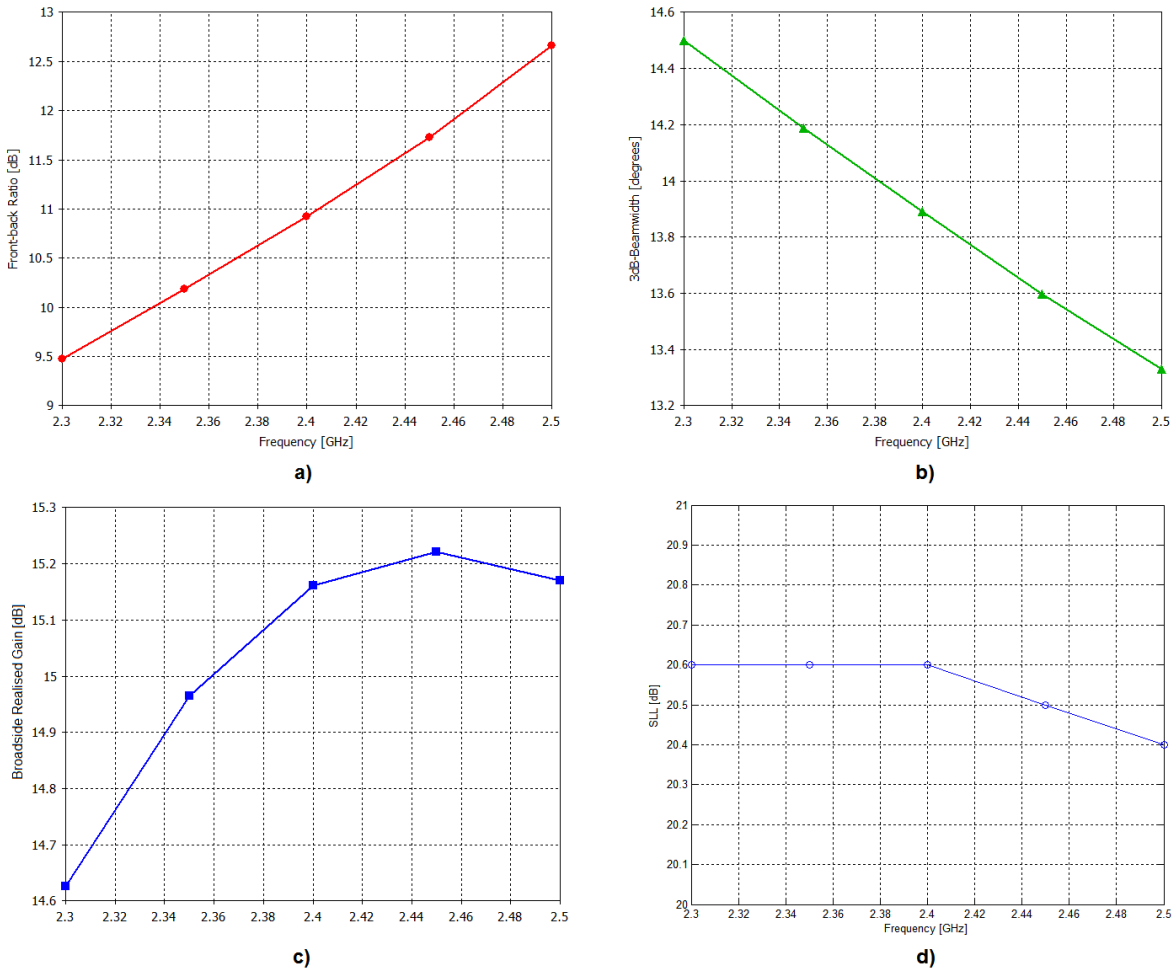

Figure 6.20 – Radiation properties over Design II passband: a) Front-back ratio (no ground-plane), b) 3dB-Beamwidth, c) Broadside realised gain, d) SLL

Figure 6.20 shows the various radiation measurements of Design II over its passband (2.3-2.5 GHz). Front-back ratio is seen to increase steadily as frequency increases, increasing by more than 3dB between the edges of the passband. 3dB-Beamwidth decreases with rising frequency, although the total change across the passband is not much more than 1°. Broadside realised gain is fairly steady across the passband, as is SLL. Although it is not plotted, axial ratio is measured as a flat 40dB across the passband. Overall, the radiation characteristics of Design II are reasonably consistent within the frequency band of interest.

Table 6.5 - Design II Results Summary (measured at 2.4 GHz)

Resonant Frequency [GHz]	2.4
FBW [%]	10
SLL [dB]	20.6
3dB-Beamwidth [°]	13.9
Broadside Realised Gain [dB]	15.18
Axial Ratio (E-plane/H-plane) [dB]	40
Front-back Ratio (no back-plane) [dB]	10.93

Table 6.5 summarises the results of Design II. The design has fully met its impedance specification and radiation specification. Furthermore, the realised gain pattern's axial ratio is 40 dB, indicating very pure linear polarisation in the E-plane.

6.5 Conclusion

This chapter has presented a design method for the elements and layout of a 1x8 uniformly-spaced patch antenna array. The design procedure has been thoroughly explained in its processes and subprocesses, and design suggestions are made at each point in the process to aid a first-time designer. The design specification step, patch design step, array design step, and adjustment step are developed and expanded upon for different design options.

The two S-band design examples have demonstrated the design procedure's operation from start to finish, and have shown its effectiveness for different patch elements. The examples show that the design procedure can produce narrowband and wideband (10% FBW) designs, and can produce consistent radiation characteristics across the antennas' passbands with linear polarisation along the antenna E-plane, as desired.

Chapter 7

Conclusion

This thesis has presented a method for the fast design and optimisation of one-dimensional, uniformly-spaced patch antenna arrays, using patch TLMs and array factor-based radiation patterns in a space mapping optimisation procedure. The method is applicable to an arbitrary number of patch elements, and is developed for use with basic coplanar- and probe-fed patches as well as aperture-coupled patches.

A theoretical overview of antenna properties, patch antennas and arrays was provided, as a conceptual foundation on which the remainder of the thesis is built. A detailed analysis of available full-wave solver systems was presented, whereby a number of convergence studies are performed on the basic and aperture-fed patch structures to determine their optimal meshing schemes. TLMs of basic and aperture-fed patch antennas were developed, with a set of validation experiments to determine the limits of the TLMs' accuracy. An optimisation framework driven by the space mapping paradigm was developed and applied to the optimisation of basic patch antennas, aperture-coupled patch antennas and 1xN uniformly-space antenna arrays.

A design procedure was developed and explained in detail which can be used to design a 1xN patch antenna array to a desired impedance and radiation specification. The procedure accepts probe-fed basic patch elements, microstrip-fed basic patch elements and aperture-coupled patch elements. The procedure was tested with 2 experimental S-band designs; a narrowband probe-fed 1x8 patch array and a wideband aperture-fed 1x8 patch array. The designs were shown to meet their specifications. In particular, the aperture-coupled patch array achieved 10% FBW over a -10 dB $|S_{11}|$ passband, and exhibited a realised gain pattern with around 13.9° 3dB-beamwidth and -20.6 dB SLL across the passband. The total solver runtime of the entire aperture-coupled patch antenna array optimisation process was 1708.14s (28.47 minutes).

The design method is fast, modular in its implementation and integration with an existing MATLAB SM framework and highly extendable to other microstrip antenna design problems. Much room for expansion exists in the sense that as long as the designer can determine a reasonably accurate TLM for the patch element they wish to use, then it can be implemented into the design method. For instance, a stacked patch geometry could be implemented and combined with the aperture-coupled feed for the design of ultra-wideband antenna arrays.

Aside from the potential for expansion that the design method offers, future projects related to the work of this thesis may involve:

- An integration of a feed network design into the array design method, possibly accelerated by Space mapping techniques. The inclusion of a feed design procedure would make the method more comprehensive, and allow the designer to design an entire antenna structure from start to finish. Existing literature on the full-wave coarse/surrogate modelling of patch antennas feeds [49] indicates that a TLM implementation may work well, especially considering that the microstrip feed-lines are easily implemented in a microwave circuit solver.
- An expansion of the design method to accommodate two-dimensional planar patch arrays.
- An extension of the feeding methods to include circularly-polarised patch antennas.
- An extension of the array optimisation procedure to accommodate nonuniform spacing, phase variation between elements and nonuniform element geometry.

Bibliography

[1] S. Koziel, Q. Cheng and J. Bandler, "Space Mapping," *IEEE Microwave Magazine,* vol. 9, no. 6, pp. 105-122, December 2008.

[2] S. Koziel and S. Ogurtsov, "Simulation-based design of microstrip linear antenna arrays using fast radiation response surrogates," *IEEE Wireless and Antenna Propagation Letters,* vol. 14, no. 1, pp. 759-762, 2015.

[3] C. A. Balanis, "Appendix VII: Vector Analysis," in *Antenna Theory Analysis and Design*, 3rd ed., NJ, USA: John Wiley and Sons, Inc., 2005, pp. 1079-1093.

[4] A. T. de Hoop, "A reciprocity relation between the transmitting and the receiving properties of an antenna," *Applied Scientific Research,* vol. 19, no. 1, pp. 90-96, 1968.

[5] C. A. Balanis, "Chapter 1: Antennas," in *Antenna Theory Analysis and Design*, 3rd ed., NJ, USA: John Wiley and Sons, Inc., 2005, pp. 1-24.

[6] C. A. Balanis, "Chapter 2: Fundamental Parameters of Antennas," in *Antenna Theory Analysis and Design*, 3rd ed., NJ, USA: John Wiley and Sons, Inc., 2005, pp. 27-132.

[7] C. A. Balanis, *Advanced Engineering Electromagnetics*, 2nd ed., New York, USA: John Wiley and Sons, 2012.

[8] Qualcomm Technologies International, Ltd. (2015). *An Introduction to Antennas and Propagation Part 1* [Online]. Available: http://www.csr.com/introduction-antennas-and-propagation-part-1. [Accessed 20 November 2015].

[9] P. J. Bevel. (2014). *Antenna-Theory: Bandwidth* [Online]. Available: http://www.antenna-theory.com/basics/bandwidth.php. [Accessed 19 November 2015].

[10] W. L. Stutzman and G. L. Thiele, *Antenna Theory and Design*, 2nd ed., New York, USA: Wiley, 1998.

[11] C. A. Balanis, "Chapter 14: Microstrip Antennas," in *Antenna Theory Analysis and Design*, 3rd ed., NJ, USA, John Wiley and Sons, Inc., 2005, pp. 811-876.

[12] P. J. Bevel. (2014). *Antenna-Theory: Microstrip Antenna Feeding Methods* [Online]. Available: http://www.antenna-theory.com/antennas/patches/patch3.php. [Accessed 13 November 2015].

[13] S. Koziel, S. Ogurtsov, W. Zieniutycs and L. Sorokosz, "Expedited design of microstrip antenna subarrays using surrogate based optimisation," *IEEE Antennas and Wireless Propagation Letters*, vol. 13, no. 1, pp. 635-638, 2014.

[14] S. Koziel, S. Ogurtsov, W. Zieniutycz and L. Sorokosz, "Simulation-driven design of microstrip antenna subarrays," *IEEE Transactions on Antennas and Propagation*, vol. 62, no. 7, pp. 3584-3591, 2014.

[15] D. M. Pozar, *Microwave Engineering*, 4th ed. NJ, USA: John Wiley and Sons, Inc., 2012.

[16] D. M. Pozar. (May 1996). *A review of aperture coupled microstrip antennas: history, operation, development, and applications* [Online]. Available: http://www.ecs.umass.edu/ece/pozar/aperture.pdf. [Accessed 7 September 2015].

[17] C. A. Balanis, "Chapter 7: Antenna Synthesis and Continuous Sources," in *Antenna Theory Analysis and Design*, 3rd ed., NJ, USA: John Wiley and Sons, Inc., 2005, pp. 385-424.

[18] S. J. Orfanidis. (2008). *Chapter 20: Antenna Arrays - Electromagnetic Waves and Antennas* [Online]. Available: http://www.ece.rutgers.edu/~orfanidi/ewa/ch20.pdf. [Accessed 10 November 2015].

[19] CST Computer Simulation Technology AG. (2015). *CST Microstrip Patch Array Design* [Online]. Available: https://www.cst.com/Applications/Article/Microstrip-Patch-Array-Design. [Accessed 10 October 2015].

[20] Altair Engineering, Inc. (2015). *FEKO Microstrip Antennas* [Online]. Available: https://www.feko.info/applications/antenna-analysis/microstrip-antennas. [Accessed 11 October 2015].

[21] CST Computer Simulation Technology AG. (2015). C*ST MICROWAVE STUDIO® - Frequency Domain Solver* [Online]. Available: https://www.cst.com/Products/CSTmws/FrequencyDomainSolver. [Accessed 10 October 2015].

[22] Altair Engineering, Inc. (2015). *FEKO Method of Moments (MoM)* [Online]. Available: https://www.feko.info/product-detail/numerical_methods/mom. [Accessed 11 October 2015].

[23] *FEKO 7.0 Help*, EM Software and Systems South Africa-S.A. (Pty) Ltd, 2014.

[24] S. Rao, D. Wilton and A. Glisson, "Electromagnetic scattering by surfaces of arbitrary shape," *IEEE Transactions on Antennas and Propagation*, vol. 30, no. 3, pp. 409 - 418, 1982.

[25] "The Simulation Method," in *CST Studio Suite Help*, CST Computer Simulation Technology AG, 2015.

[26] "Discrete Port," in *CST Studio Suite Help*, CST Computer Simulation Technology AG, 2015.

[27] "Waveguide Port," in *CST Studio Suite Help*, CST Computer Simulation Technology AG, 2015.

[28] A. Alsager, "Design and Analysis of Microstrip Patch Antenna Arrays," M.S. Thesis, School of Engineering, University College of Borås, Borås, Sweden, January 2011.

[29] "Time Domain Solver Overview," in *CST Studio Suite Help*, CST Computer Simulation Technology AG, 2015.

[30] D. Jaisson, "Transmission-line model for the input impedance of a slot coupled rectangular patch antenna," *IEE Proceedings - Microwave, Antennas and Propagation*, vol. 153, no. 5, pp. 461-468, 2005.

[31] D. Jaisson, "Simple model for computing the input impedance of a rectangular patch antenna with electromagnetic coupling," *IEE Proceedings*, vol. 51, no. 8, pp. 476-480, 2004.

[32] Wolfram Research, Inc. (2015). *Bessel Functions- Wolfram MathWorld* [Online]. Available: http://mathworld.wolfram.com/BesselFunction.html. [Accessed 24 November 2015].

[33] F. Venneri, S. Costanzo and G. D. Massa, "Transmission line analysis of aperture-coupled reflectarrays," *Progress to Electromagnetics Research*, vol. 4, pp. 1-12, 2008.

[34] M. Himdi, C. Terret and J. P. Daniel, "Transmission line analysis of aperture-coupled microstrip antenna," *Electronics Letters*, vol. 25, no. 18, p. 1229–1230, 1989.

[35] J. P. Kim, "Optimum design of an aperture-coupled microstrip patch," *Microwave and Optical Technology Letters*, vol. 39, no. 1, pp. 75-78, 2003.

[36] D. M. Pozar, "A reciprocity method of analysis for printed slot and slot-coupled microstrip antennas," *IEEE Transactions- Antennas and Propagation*, vol. 4, no. 12, pp. 1439-1446, 1986.

[37] G. Splitt and M. Davidovitz, "Guidelines for the design of electromagnetically coupled microstrip antennas on two-layer substrates," *IEEE Transactions- Antennas and Propagation,* vol. 38, no. 7, pp. 1136-1140, 1990.

[38] S. A. Schelkunoff and H. T. Friis, *Antennas: Theory and Practice,* New York, USA: John Wiley and Sons, Inc., 1952.

[39] Wolfram Research, Inc. (2015). *Cosine Integral - Wolfram MathWorld* [Online]. Available: http://mathworld.wolfram.com/CosineIntegral.html. [Accessed 24 November 2015].

[40] Wolfram Research, Inc. (2015). *Sine Integral - Wolfram MathWorld* [Online]. Available: http://mathworld.wolfram.com/SineIntegral.html. [Accessed 24 November 2015].

[41] Wolfram Research, Inc. (2015). *Euler-Mascheroni Constant - Wolfram MathWorld* [Online]. Available: http://mathworld.wolfram.com/Euler-MascheroniConstant.html. [Accessed 24 November 2015].

[42] S. Koziel, J.W. Bandler and K. Madsen, "A Space-mapping framework for engineering optimization—theory and implementation," *IEEE Transactions on Microwave Theory and Techniques,* vol. 54, no. 10, pp. 3721-3730, 2006.

[43] J. Lagarias, J. A. Reeds, M. H. Wright and P. E. Wright, "Convergence properties of the nelder-mead simplex method in low dimensions," *SIAM Journal of Optimization,* vol. 9, no. 1, p. 112–147, 1998.

[44] S. Baluja, "Population-based incremental learning: A method for integrating genetic search based function optimization and competitive learning," *Technical Report CMU-CS-94-163,* Carnegie Mellon University, 1994.

[45] S. Baluja, "An empirical comparison of seven iterative and evolutionary function optimization heuristics," *Technical Report CMU-CS-95-193,* Carnegie Mellon University, 1995.

[46] The MathWorks, Inc. (2015). *MATLAB Function Reference* [Online]. Available: http://www.mathworks.com/help/matlab/functionlist.html. [Accessed 10 November 2015].

[47] P. O'Connor. (2010). *Peakseek - MATLAB Central File Exchange* [Online]. Available: http://www.mathworks.com/matlabcentral/fileexchange/26581-peakseek. [Accessed May 2015].

[48] P. J. Bevel. (2014). *Antenna-Theory: Dolph-Chebyshev Weights* [Online]. Available: http://www.antenna-theory.com/arrays/weights/dolph.php. [Accessed 24 November 2015].

[49] S. Koziel, S. Ogurtsov, W. Zieniutycz and L. Sorokosz, "Simulation-driven design of microstrip antenna subarrays," *IEEE Transactions on Antennas and Propagations*, vol. 62, no. 7, pp. 3584-3591, 2014.

Appendix A – TLM Experiment 1

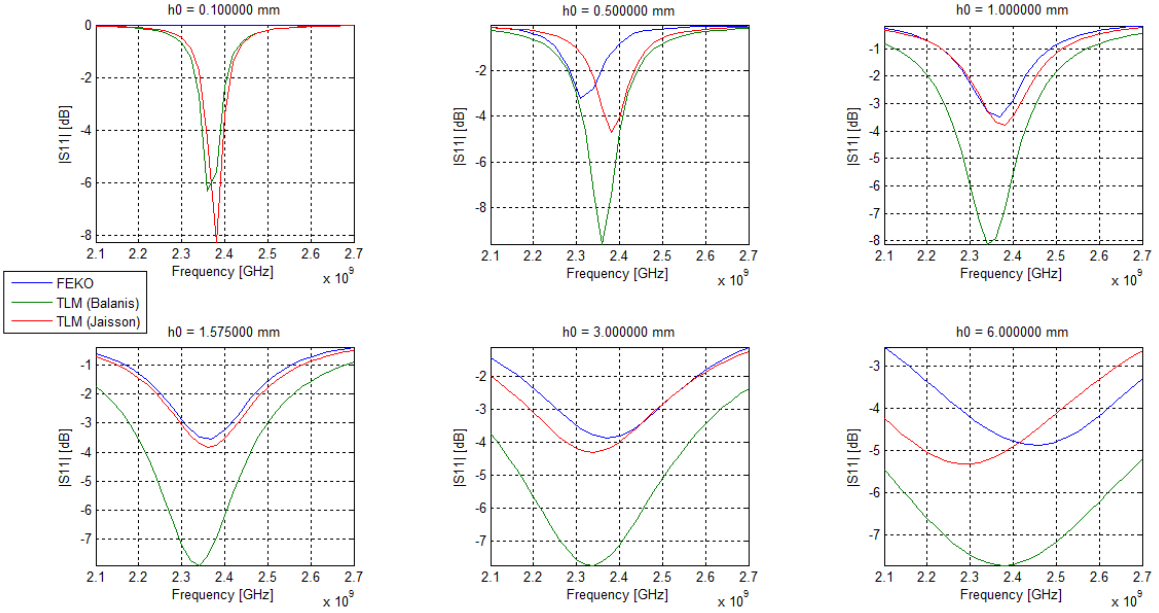

Figure A 1- S_{11} comparison of Basic patch TLMs (ε_{rp}= 1)

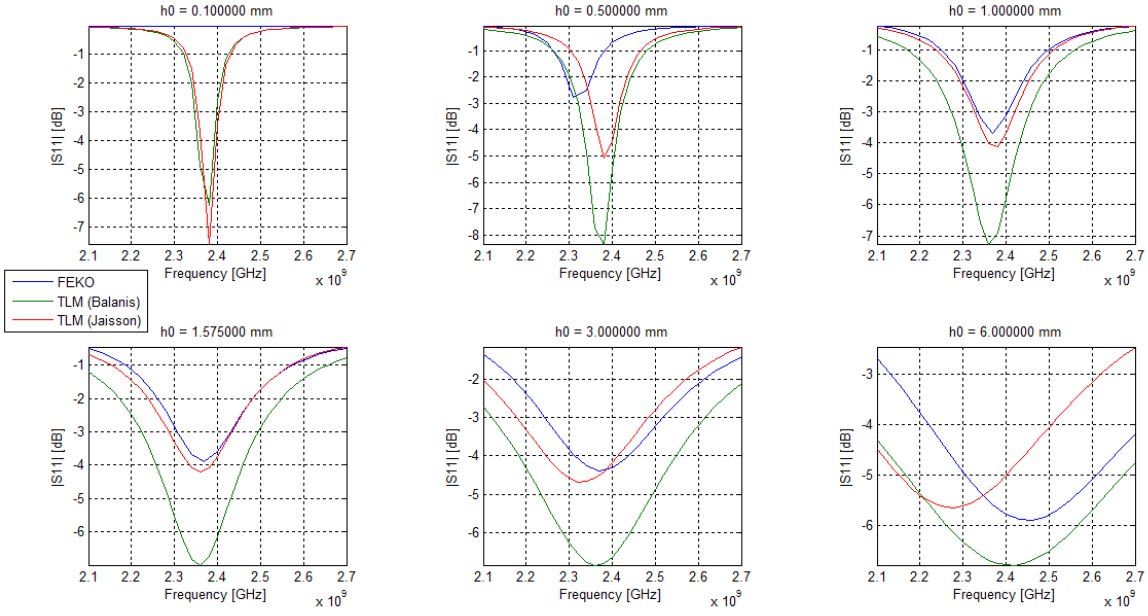

Figure A 2- S_{11} comparison of Basic patch TLMs (ε_{rp}= 1.5)

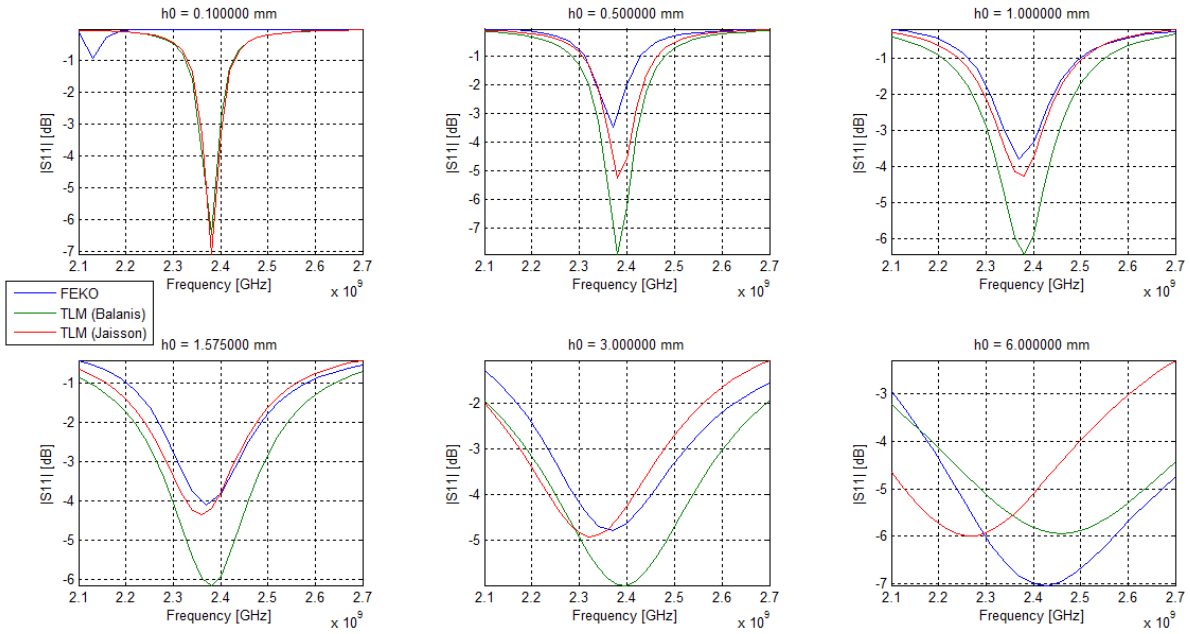

Figure A 3- S_{11} comparison of Basic patch TLMs ($\boldsymbol{\varepsilon_{rp}}$= 2.2)

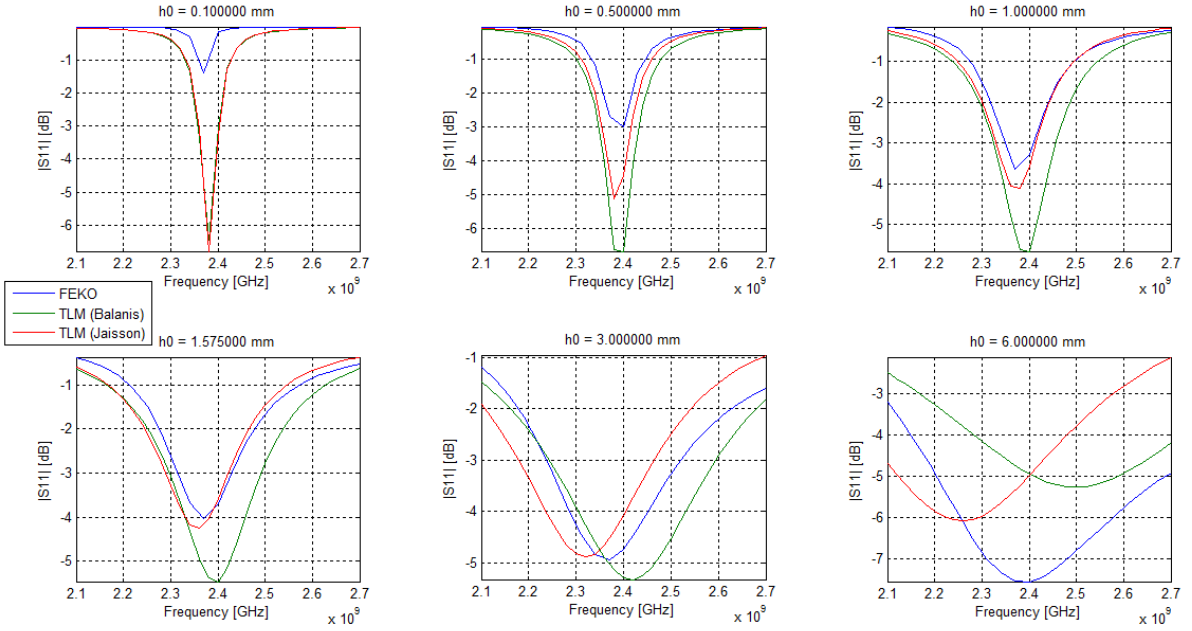

Figure A 4- S_{11} comparison of Basic patch TLMs ($\boldsymbol{\varepsilon_{rp}}$= 3)

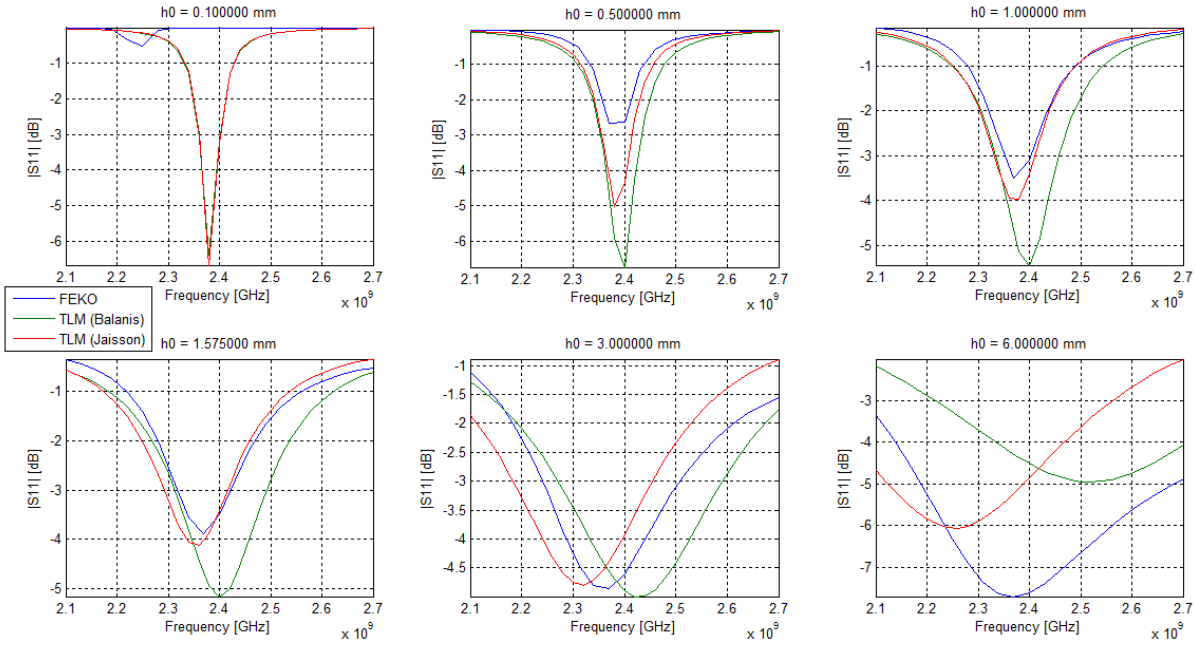

Figure A 5- S_{11} comparison of Basic patch TLMs ($\boldsymbol{\varepsilon_{rp}}$= 3.5)